

Towards Molecular-Scale Sensing and
Thermoelectric Energy Harvesting

Ali K. Ismael

PhD Thesis in Nanoelectronics

Submitted in part fulfilment of the requirements for the degree of

Doctor of Philosophy

September 2016



Declaration

This thesis is a result of the author's original work and has not been submitted in whole or in part for the award of a higher degree elsewhere. This thesis documents the work carried out between November 2012 and June 2016 at Lancaster University, UK, under the supervision of Prof. Colin J. Lambert and funded by Tikrit University - Iraq.

Ali

June 2016

Abstract

Nowadays, the world is advancing rapidly toward small scale electronic devices, eventually approaching the few nm length scale. The ultimate goal of this thesis is to contribute to the understanding of nanotechnology by exploring the electronic and thermoelectronic properties of systems containing two metallic electrodes that are linked by single molecules.

Density Functional Theory (DFT), with combined Green's functions quantum transport calculations and Tight Binding Models (TB), are used in this study together with in addition, experimental measurements which were carried out by myself and several experimental collaborators. This work is divided into three resulting chapters, covering electron transport through Crown-Ether-Bridged Anthraquinones. Finally, Fullerenes and Endohedral Metallofullerenes (theoretical and experimental results).

The list of author's publications:

1. Ali K. Ismael, Iain Grace and Colin J. Lambert, "Increasing the thermopower of crown-ether-bridged anthraquinones", *Nanoscale*. **7**, 17338-17342 (2015).
2. Rincn-Garca, Laura, Ali K. Ismael, Charalambos Evangeli, Iain Grace, Gabino Rubio-Bollinger, Kyriakos Porfyrakis, Nicols Agrat, and Colin J. Lambert. "Molecular design and control of fullerene-based bi-thermoelectric materials", *Nature materials*, Vol.15, Issue3, P254 (2015).

Acknowledgements

The work completed in this thesis could not have been done without the help and guidance from a number of people. I would like to first thank my supervisor Colin Lambert for his constant guidance and showing me that complex problems can always be reduced into simpler ones.

Special thanks goes to Iain Grace, you have given up a lot of time to answer my questions, and to Steve Bailey for his helping and support, to my group members too. I would also like to thank Nicolas and his group Laura and Charalambos UAM University Madrid. I am also grateful to Liverpool group, Richard, Simon, Andrea and David.

Special thanks goes to the International office in Lancaster University, especial one to Michele, Claire, Jamie and Heather. I have to send a great thank to Newcastle College staff, very especial thanks goes to Bruce Downie.

I thank my friends old and new, you have kept me sane throughout this exhausted process, I shall start from Newcastle upon Tyne where I spent great times, Bal and his wife (wey aye, man!), Arun (Pain killer!). Newcastle College friends, Spanish, Italian, Germans, the French, Chinese, Korean..... etc, great memories! Lancaster, first year housemates, Oliy, Will, Nafer and Jordan. Dallas's school kids shouting morning!. Second year, Amy, John, Jack and Joe..... our lovely landlady Marjorie. Balmoral housemates for 2 years, Jess, Dorcus and Arthur, I really enjoying my stay there with those guys.

Finally, a massive thank you to my family Mum and Dad for their constant support and love, and without them I couldn't have achieved what I have done.

Contents

1	Introduction	2
1.1	Motivation	2
1.2	Outline	5
2	Density Functional Theory	9
2.1	Many - body Hamiltonian	10
2.2	Born - Oppenheimer approximation	11
2.3	Hohenberg - Kohn theorems	14
2.4	Kohn - Sham equations and self consistency	16
2.5	Exchange and correlation	20
2.5.1	Local Density Approximation	23
2.6	SIESTA technique	25
2.6.1	Norm-conserving pseudopotentials	25
2.6.2	Localized basis	29
2.7	Some preparation for SIESTA	32
2.7.1	SIESTA calculations	32
2.8	Basis Set Superposition Error (BSSE)	33
3	Green's functions method	40
3.1	Green's function of an infinite 1D chain	40
3.2	Green's function of a semi-infinite 1D chain	44
3.3	Green's function of two 1D semi-infinite chains brought together	45
3.4	Green's function of a single impurity between 1D chains	48

3.5	Green's function of a general scatterer between semi-infinite 1D chains	49
3.6	Green's function of a general system	51
3.6.1	Green's function of an infinite periodic system	51
3.6.2	Green's function of a semi-infinite periodic system	56
3.6.3	Including a scattering region	58
3.7	Obtaining the transmission coefficients	59
4	Theory of Quantum Transport	63
4.1	Single electron transport	63
4.2	Transmission coefficient	65
4.3	Landauer formula and scattering formalism	69
4.4	Thermoelectric coefficients	71
4.4.1	Generalized formula for the thermoelectric coefficients	74
5	Crown Ethers	82
5.1	Introduction	82
5.2	Types of Crown Ethers	83
5.3	Nomenclature of Crown Ethers	83
5.4	Properties of Crown Ethers	84
5.5	Size Fitting of the Cation	84
5.6	Crown Ethers Applications	85
5.7	Selectivity of Crown Ethers	86
5.8	Binding energy	86
5.9	Structure of Molecular Wires	89
5.10	Controlled Shifting of Transmission Resonances	90
5.11	Sensing Mechanism	92
5.12	Doping of crown ethers with donor and acceptor molecules	101
5.13	Discriminating sensing of cations in crown-ether-bridged anthraquinones	104
5.14	Thermoelectric properties of crown-ether-bridged anthraquinones . .	108

6	Fullerenes and Endohedral Metallofullerenes	122
6.1	Introduction	122
6.1.1	Fullerenes	122
6.1.2	Endohedral Metallofullerenes	123
6.1.3	Trimetallic Nitride Endohedral Metallofullerenes	124
6.1.4	Production of $Sc_3N@C_{80}$	125
6.2	Geometry and Electronic Properties of Fullerenes	126
6.2.1	Electronic Properties of Hollow Cage Fullerenes	126
6.2.2	Electronic Properties of Trimetallic Nitride Endohedral Metallofullerenes	126
6.3	Applications of Fullerenes and Endohedral Fullerenes	128
6.4	Experimental measurements of single-molecule conductance and thermopower	129
6.5	Scanning Tunneling Microscopy (STM)	129
6.6	Basic Principle of Scanning Tunneling Microscopy	130
6.7	Experimental Method (STM)	132
6.7.1	Substrate preparation, experimental setup and technique	132
6.7.2	Thermal circuit	134
6.8	Experimental results	136
6.8.1	Pressure variation with tip displacement of the conductance, the thermopower, and the power factor of $Sc_3N@C_{80}$ junctions	139
6.9	Theoretical modeling of thermopower switching	140
6.10	Does Sc_3N rotate inside the cage?	140
6.11	Binding energy of $Sc_3N@C_{80}$ on gold	141
6.12	Comparison between Fullerenes and Endohedral Fullerenes	143
6.13	Frontier Orbitals of the $Sc_3N@C_{80}$ Molecule	144
6.14	Transmission coefficient as a function of orientation of the $Sc_3N@C_{80}$ molecule	145
6.14.1	Rotating	145

6.14.2 Pressing	147
7 Summary and Suggestions for Further Research	157
7.1 Summary	157
7.2 Suggestions for Further Research	158

List of Figures

2.1	Schematic of the self consistent DFT cycle starting from an initial density $n^i(r)$, which is used to calculate the Kohn-Sham potential V_{KS} , Hamiltonian \hat{H}_e and wavefunctions $\{\Psi_i^{KS}\}$ of the system. This allows a new density $n_{new}^i(r)$ to be calculated, and the cycle is repeated until convergence is achieved	19
3.1	Tight-binding approximation of a one-dimensional periodic lattice with on-site energies ε_o and hopping parameters γ	41
3.2	One dimensional semi-infinite tight-binding chain with ε_o on-site energies and γ hopping parameters, left: for the left lead, right: for the right lead.	44
3.3	Two semi-infinite 1D chains brought together	45
3.4	Tight-binding chain with a single scatterer	48
3.5	Tight-binding chains with a general scatterer	49
3.6	A general infinite periodic lead	51
4.1	A general scattering region (described by H_M) attached to leads, made up from infinite slices of H_0 connected by H_1 . The scattering region, also called the Extended Molecule (EM) already contains part of the leads.	65
4.2	A plane wave impinging on a potential barrier. The wave is partially reflected with a probability amplitude r , and partially transmitted with a probability $\mathcal{T} = t ^2$	68

4.3	Schematics of one dimensional lead-scatterer-lead arrangement and the electron reservoirs with μ_L (left) and μ_R (right) chemical potential.	69
5.1	12-Crown-4, red oxygen atoms, blue nitrogen, yellow sulfur, gray carbon and white hydrogen	82
5.2	Topology and classification of crown ethers, (D: donor atom, B: bridgehead atom and \frown : chain segment without donor atom). . . .	83
5.3	"Host-guest" complexes formed from crown ethers and ions of alkali metals.	85
5.4	Fully optimized minimum energy structure of complex 15C5 with Li^+ or Na^+ or K^+ (left to right)	87
5.5	Fully optimized minimum energy structure of complex (15C5+ Li^+) in vicinity of water	88
5.6	Molecular wires containing ether bridges. left AQOC, right AQNC .	89
5.7	Geometry of the molecular junction containing AQOC(12C4) and AQNC(12C4) molecular wire attached between two gold electrodes	90
5.8	Transmission coefficient AQNC (12C4, 15C5 and 18C6)	91
5.9	Transmission coefficient AQOC (12C4, 15C5 and 18C6)	92
5.10	Diagram of sensing mechanism	93
5.11	Sampling the cation (Li^+ ion) position in the vicinity of AQOC (12C4) cavity. (For clarity the alkyl arms and electrodes are not shown.)	93
5.12	Binding energy of AQOC (12C4) as a function of Li^+ position . . .	94

5.13	Transmission curves, the black dotted line is the transmission curve for the optimum binding of (Li^+ and PF_6^-) to AQ (12C4). The yellow curves show the transmission coefficient for a selection of the 245 possible configurations of the 245 possible configurations of (Li^+ and PF_6^-) bound to AQ (12C4), whose binding energies are shown in Fig 5.12. The green curve shows the ensemble-averaged transmission $\langle \mathcal{T}(E) \rangle$, obtained by averaging the 245 yellow curves weighted by a Boltzmann factor.	95
5.14	Counter ions left BF_4^- and PF_6^- right	96
5.15	Complexes left AQOC (15C5) and AQNC (15C5) right	97
5.16	Transmission coefficient curves. Top panel AQNC, Lower panel AQOC, both trapped (15C5) Li^+ , Na^+ and K^+	98
5.17	Sandwich (two ions, above and beneath the ligand) AQOC (15C5), BF_4^- counter ion	99
5.18	Transmission coefficient sandwich AQNC (15C5), blue one ion (K^+ and red two ions ($2K^+$)	99
5.19	Transmission coefficient sandwich AQOC (15C5), blue one ion (K^+ and red two ions ($2K^+$)	100
5.20	Transmission coefficient for AQOC (15C5) with PF_6^- (black) counter ion and BF_4^- (red) when complexed with Li^+ ion	101
5.21	Fully relaxed structure of TTF and TCNE	101
5.22	Optimum geometry of AQOC 15C5 with TTF (Top) and TCNE (Bottom)	102
5.23	Transmission coefficient AQOC (15C5) + TTF and TCNE (Top), and AQNC + TTF and TCNE (Bottom)	103
5.24	Zero bias transmission coefficient, $\mathcal{T}(E)$ of AQOC for different cavity sizes (12C4, 15C5 and 18C6) plus alkali Li^+ (a). Ligand (12C4) with different alkalis Li^+ , Na^+ and K^+ (b)	105

5.25	Zero bias transmission coefficient, $\mathcal{T}(E)$ of AQNC for different cavity sizes (12C4, 15C5 and 18C6) plus alkali Li^+ (a). Ligand (12C4) with different alkalis Li^+ , Na^+ and K^+ (b)	107
5.26	The change in conductance, $\mathcal{T}(E)$ calculated at $E_F = 0eV$ for six molecules and three ions (Note: AQOC and AQNC written in short OC and NC on X-axis)	108
5.27	The change in thermopower S for different cation compared with the bare (ligand). Top panel AQOC and lower panel AQNC (12C4)	109
5.28	Thermopower as function of temperature for complexes of AQOC (a) and AQNC (b)(12C4)	111
5.29	Thermopower as function of conductance for complexes of AQOC (a) and AQNC (b)(12C4)	113
5.30	Power factor as function of temperature for complexes of AQOC (a) and AQNC (b)	114
6.1	Buckminsterfullerene (C_{60})	123
6.2	I_h isomer (C_{80}), $Sc_3N@C_{80}$	124
6.3	Apparatus used to produce fullerenes by arc vaporization of graphite rods [6]	125
6.4	Six isomers of C_{80}	127
6.5	An example of stable isomer $Gd@C_{82}$	127
6.6	Diagram of a STM tip scanning an Au(111) surface. The Au(111) surface is revealed to have a <i>herringbone</i> reconstruction pattern as well as atomic step edges [43]	131
6.7	Example of topographic images, left image at low temperature . . .	132

- 6.8 Scanning tunnelling microscope images and tunnelling spectroscopy.
 a, Schematic of the endohedral fullerene $Sc_3N@C_{80}$ used in this work; notice the Sc_3N in the centre of the fullerene cage. b-d STM images of the molecules on atomically flat (111) Au surfaces showing preferential adsorption at step edges (b), islands (c) and isolated molecules (d). e,f IV characteristics (e) and differential conductance (f) in tunnelling regime on two different molecules, presenting opposite rectifying behaviour. 133
- 6.9 Technique for the simultaneous measurement of conductance and thermopower. *a, b*, Tip displacement z and applied bias voltage ΔV at the molecular junction, respectively, as a function of time. The bias voltage is maintained at a fixed value ΔV_0 during the tip motion (in blue in a) and every few picometers it is swept between $\pm\Delta V_0$ while the tip is stationary (in red in a). In the experiments, the bias voltage ΔV_0 was set to 6-10 mV and the tip was stopped every 15 – 25 pm. In each approaching-separating cycle, 50 – 100 $I - V$ traces are acquired. *c*, Experimental $I - V$ curves showing the voltage offset due to the temperature difference. 134
- 6.10 Equivalent thermal circuit of the setup for the determination of the thermopower. The substrate and body of the *STM* are at ambient temperature T_c while the tip is heated to a temperature $T_h = T_c + \Delta T$ above ambient temperature. S is the thermopower of the molecular junction and S_{lead} is the thermopower of the *tip - connecting* lead. V_{bias} is the bias voltage applied to the junction. 135

- 6.11 Thermopower and conductance simultaneous measurements. a,b, Conductance, G (blue), and thermopower, S (green), simultaneously acquired while approaching individual $Sc_3N@C_{80}$ molecules. For the molecule in a, the thermopower is always negative, while for that one in b, it is always positive. In these measurements the temperature difference was $\Delta T \simeq 40K$. $G_o = (2e^2)/h$, where e is the electron charge, and h is Plancks constant, is the conductance quantum. The portion of the thermopower trace highlighted in yellow corresponds to molecular contact with the tip. c, Schematic representation of the experimental setup. The tip is heated to a temperature T_h above ambient temperature T_c , while the substrate is maintained at T_c . d,e, Conductance G and thermopower S at first-contact histograms of $Sc_3N@C_{80}$ (in blue and green, respectively) compared to C_{60} (in grey). For the $Sc_3N@C_{80}$ histograms, the mean conductance value is $\bar{G} = 0.05G_o$ and the mean thermopower is $\bar{S} = -2\mu V/K$ 136
- 6.12 Effect of pressure on $Sc_3N@C_{80}$ molecular junctions. a-c, Periodical variations of the conductance G , thermopower S and power factor GS^2 , respectively, as the STM tip advances and retracts during three cycles. Each half cycle corresponds to less than 0.5 nm. Each colour corresponds to a different molecule. d-f, the same effect of pressure but on C_{60} 137

6.13	Effect of pressure on $Sc_3N@C_{80}$ junctions as a function of tip displacement. Periodical variations of the conductance G (a,d,g), the thermopower S (b,e,h), and power factor GS^2 (c,f,i) as a function of the tip displacement. This is the same data as in Fig.6.12a-c and the colours correspond to same three molecules detailed in the main text (1, 2 and 3). For molecule 1 (red), compressing the molecule results in S varying from $+20\mu V/K$ to almost $0\mu V/K$; for molecule 2 (blue), S varies from $+10\mu V/K$ to $-5\mu V/K$; and for molecule 3 (green), S varies from approximately $0\mu V/K$ to $-20\mu V/K$. Each half cycle corresponds to less than 0.5 nm. This representation is directly equivalent to the plot of the theoretical calculations j-l.	139
6.14	(a) Charge transfer model for $Sc_3N@C_{80}$ (b) Rapid circular motion of the Sc_3N cluster inside the $I_h C_{80}$ cage.	140
6.15	Binding energy as a function of rotation of Sc_3N within the fixed $I_h - C_{80}$ cage.	141
6.16	$Sc_3N@C_{80}$ on a gold surface. Top panels: Orientation of the $Sc_3N@C_{80}$ molecule with respect to the gold leads corresponds to the defined angle (left) $\theta = 0^\circ$ and (right) $\theta = 90^\circ$. Lower panel: Binding energy of $Sc_3N@C_{80}$ to gold as a function of molecule-contact distance. The equilibrium distance is found to be approximately 2.3 \AA from the minimization of the binding energy.	142
6.17	Transmission curves, for C_{60} and $Sc_3N@C_{80}$ junctions, respectively. Letters H and L indicate the HOMO and LUMO peaks of the fullerene cages.	144
6.18	Wavefunctions of the HOMO – LUMO orbitals of the $Sc_3N@C_{80}$ molecule.	145
6.19	Rotation angles θ between 0° and 90° of the $Sc_3N@C_{80}$ molecule with respect to the gold leads.	146

6.20	Transmission coefficient as a function of orientation. Zero bias transmission coefficient $\mathcal{T}(E)$ versus electron energy E for rotation angles θ between 0° and 180° of the $Sc_3N@C_{80}$ molecule with respect to the gold leads.	146
6.21	Optimized geometries of $Sc_3N@C_{80}$ and C_{60} junctions.	147
6.22	Transmission curves, $\mathcal{T}(E)$, for different z (C_{60}). The Fermi level is shifted from the position given by <i>DFT</i> and the black dotted line indicates the true Fermi level as explained in the text. In this case, $E_F = E_F^0 - 0.165eV$, chosen such as to present similar amplitude variations as the experimental curves.	147
6.23	Transmission coefficient as a function of orientation and tip separation. Transmission curves, $\mathcal{T}(E)$, for three different orientations ($\theta = 150^\circ$, $\theta = 57^\circ$, and $\theta = 63^\circ$, respectively) and for different z	148
6.24	Thermopower as a function of orientation and tip separation. Thermopower S versus orientation angle at a value of $E_F = 0.23$ eV, for different tip-substrate distances z	148
6.25	Optimized geometries of $Sc_3N@C_{80}$ junctions. Four optimized geometries corresponding to tip-carbon distances of 2.7, 2.5, 2.3 and 2.1 Angstroms. They show that the C_{80} barely distorts over such a range. In these simulations, the gold is not allowed to relax.	149
7.1	Schematic of a Tandem device	160

List of Abbreviations and Symbols

DFT	Density Functional Theory
\mathcal{H}	Hamiltonian
LDA	Local Density Approximation
GGA	Generalised Gradient Approximation
LCAO	Linear Combination of Atomic Orbital
ζ	Basis function
SZ	Single Zeta
SZP	single Zeta Polarised
DZ	Double Zeta
DZP	Double Zeta Polarised
1D	One dimension
EM	Extended Molecule
PL	Principal Layer
PBC	Periodic Boundary Conditions
STM	Scanning Tunneling Microscopy
NC	Nitrogen Crown
OC	Oxygen Crown
AQOC	Anthraquinone with oxygen atoms
AQNC	Anthraquinone with nitrogen atoms
BE	Binding Energy
$\mathcal{T}(E)$	Transmission curve
Complexes	<i>Ligand + Ion</i>
BF_4^-	Counter Ion
PF_6^-	Counter Ion
Sandwich	Two Ions and one ligand
TCNE	Tetracyanoethylene
TTF	Tetrathiafulvalene
S	Thermopower or Seebeck coefficient

Π	Peltier coefficient
ZT	Figure of merit
P	Power factor
C_{60}	Buckminsterfulleren
I_h	icosahedral (isomer)
$Sc_3N@C_{60}$	Endohedralmetallofulleren
TNT	Trimetallic Nitride template method
$HOMO$	Highest Occupied Molecular Orbital
$LUMO$	Lowest Unoccupied Molecular Orbital
NMR	Nuclear Magnetic Resonance
$BSSE$	Basis Set Superposition Error
V_{oc}	Voltage open circuit

Chapter 1

Introduction

1.1 Motivation

1947 was the breakthrough in an electronic world when Shockley and his co-workers built the first transistor at Bell laboratories. Since then the door has been opened for communications and modern technology to kick off. Throughout the past 70 years the transistor has been the fundamental building block in most electronic devices and is recognised as one of the most important inventions of the previous century. In this time the size of the transistor has been dramatically reduced from a few centimetres to tens of nanometres. The reduction in the size of transistor has followed the path of Moore's law [1], which predicts the doubling in the number of transistors on an integrated circuit every eighteen months. This process enables industrial factories to produce smaller, faster and more energy efficient devices. As this trend approaches the nano-scale, conventional manufacturing of transistors will become problematic as a result of this large reduction in size. The electronics industry will therefore be forced to change from conventional semiconducting materials and methods, to newer approaches and exotic materials [2]. From a spectrum of possibilities, molecular electronics could be a solution to this problem, providing the required reduction in size and flexibility of design.

The idea of using a molecule as an electrical device started in 1970s. The

theoretical prediction by Aviram and Ratner [3] showed that a single molecule could be used as a rectifier. However, it was not until 1997 when Reed et al [4] first measured the current through a single phenyl-dithiol molecule using a mechanically control label break-junction, that molecular electronics took off.

One of the major problems in electronic devices is the amount of waste heat produced by their transistors. This is not just a problem for small personal devices, the combined electricity consumption of IT systems (communication networks, personal computers, data centres, etc.) was 900 TWh in 2012, or 4.6% of global electricity use, and this figure is set to double by 2025 [5].

To meet this challenge, research labs around the world are aiming to create high-performance thermoelectric materials and devices, which can convert this waste heat back into electricity. The thermopower (or Seebeck coefficient) S of a material is defined as $S = - \Delta V / \Delta T$, where V is the voltage difference generated between the two ends of the junction when a temperature difference T is established between them. In addition to the goal of maximising S , there is a world-wide race to develop materials with a high power factor $P = S^2 G$, and high thermoelectric efficiency, which is expressed in terms of a dimensionless figure of merit $ZT = PT/\kappa$, where T is the average temperature, G is the electrical conductance and κ is the sum of the electronic and phononic contribution to the thermal conductance. In addition there is a need for thermopowers of both positive and negative signs, so that materials with thermopowers of opposite signs can be organised in tandem to boost the thermovoltage. The difficulty in thermoelectrics research is that S and G usually work against each other in a given bulk material, with high S usually accompanied by low G [6].

A key strategy for improving the thermoelectric properties of inorganic materials has been to take advantage of nanostructuring which leads to quantum confinement of electrons, suppression of parasitic phonons and enhanced thermoelectric performance. For example, nanostructured materials such as PbSeTe/PbTe-based quantum dot superlattices with ZT of ~ 2 were realised over a decade ago [7].

However lack of further improvement since that time suggests that new strategies are needed. Since nanostructuring underpins the current state of the art for inorganic thermoelectrics, it is natural to examine the thermoelectric performance of single- or few-molecule junctions as a stepping stone towards the design of new high-performance organic materials, because the single-molecule building blocks of organic materials offer the ultimate limit of electronic confinement, with energy-level spacings which are orders of magnitude greater than $k_B T$ at room temperature. The ability to measure thermopower in single-molecule junctions is relatively new and the thermoelectric properties of only a few molecules have been measured. More than one of these were a recent measurement by ourselves of the thermopower of C_{60} . [8–10]

The key to enhancing the thermoelectric performance lies in taking advantage of resonances in the electronic density of states, (associated with the discrete spectrum of molecular levels), because (loosely) the thermopower is proportional to the slope of the density of states at the Fermi energy of the electrodes. In C_{60} and all single molecules measured to date, the Fermi energy is far away from any molecular energy levels and there currently exists no experimental evidence of the effect of resonant transport on thermoelectric properties.

To reveal this evidence, I have investigated the thermopower and power factor of the endohedral fullerene $Sc_3N@C_{80}$. This was chosen because our density functional theory predicted that the Sc_3N within the fullerene cage would create a sharp resonance near the Fermi energy. Remarkably, through a joint experimental and theoretical study, we have demonstrated that the energetic location of this resonance and hence the sign of the thermopower can be tuned by applying pressure. This means that we have identified the worlds first example of a pressure-dependent bi-thermoelectric material, which can exhibit both positive and negative thermopower.

1.2 Outline

My thesis will report a study of the electrical and thermoelectrical properties of different types of molecules and compare theory results with experimental results. To start with, Chapter 2 gives an introduction to Density Function Theory, the Hohenberg-Kohn theorems and the Kohn-Sham ansatz. It also describes the functional forms of the exchange and correlation energy in the local density approximation, and the generalized gradient approximation. The SIESTA code (which is the main DFT code used in this work) is introduced, whereby the finer details of the calculations are described, such as the use of pseudopotentials and the type of basis sets. Finally, the Basis Set Superposition Error (BSSE) is used to find the optimum distances between molecules and electrodes and to calculate the magnitude of binding energies.

Chapter 3 describes how to construct the Green's function of a molecular device, consisting of a scattering region connected to semi-infinite electrodes (leads) from the Hamiltonian and scattering matrices obtained from DFT simulations. The central result shows how the electron transmission coefficient is related to the retarded Green's function of the system. This method is adopted in the Gollum code; a first principles quantum transport code, developed at Lancaster and Oviedo Universities. Gollum is applied (chap.5, chap.6 and chap.7) to obtain the electron transport through single molecule systems.

Chapter 4 gives a brief introduction to the theory of quantum transport, including the transmission coefficient $\mathcal{T}(E)$, the Landauer formula and scattering formalism, thermoelectric coefficients such as thermopower, conductance and power factor.

Chapter 5 starts by giving a brief details about crown ethers, their names, types, properties, size and applications. Sensing and thermoelectic properties are covered for two types of crown ethers AQ-bridged crown ether (AQOC) and AQ-daza-bridged crown ethers (AQNC). Three sizes of crown are investigated (12C4, 15C5 and 18C6) for the two types of crown ethers, and the bindings of three cations (Li^+ , Na^+ and K^+) within the crown is explored. In addition, a

donor (TTF), and acceptor (TCNE) molecules are used to see their effect on the electrical and thermoelectrical properties.

Chapter 6 deals with fullerenes and endohedral metallofullerenes. It describes a joint theoretical and experimental study. It begins with a brief description of fullerenes and endohedrals, the production of $Sc_3N@C_{80}$, the main molecule studied- and possible applications of fullerenes and endohedrals. A detailed study of the conductance and thermopower $Sc_3N@C_{80}$ is carried out, investigating the role of pressure to create a bi-thermoelectric material. The theoretical model explains the experimental results through the localization of an orbital on the central Sc_3N inside the cage.

Bibliography

- [1] G. Moore, "Cramming more components onto integrated circuits", *Electronics*, vol. 38, Apr 19 : 114-117, 1965.
- [2] C. A. Pignedoli, A. Curioni and W. Andreoni, "Anomalous behavior of the dielectric constant of hafnium silicates: a first principles study", *Physical review letters* 98.3 : 037602., 2007.
- [3] A. Aviram and M. A. Ratner, "Molecular rectifiers", *Chemical Physics Letters* 29.2 : 277-283., 1974.
- [4] M. A. Reed, C. Zhou, C. J. Muller, T. P. Burgin and J. M. Tour, "Conductance of a molecular junction", *Science* 278.5336 : 252-254, 1997.
- [5] V. Heddeghem, Ward, S. Lambert, B. Lannoo, D. Colle, M. Pickavet, and P. Demeester, "Trends in worldwide ICT electricity consumption from 2007 to 2012", *Computer Communications* 50: 64-76., 2014.
- [6] J. P. Heremans, S. M. Dresselhaus, L. E. Bell, and D. T. Morelli, "When thermoelectrics reached the nanoscale", *Nature nanotechnology* 8, no. 7: 471-473, 2013.
- [7] G. S. Nolas, "Bulk dimensional nanocomposites for thermoelectric applications", U.S. Patent No. 8,759,662. 24 Jun. 2014.
- [8] C. Evangeli, K. Gillemot, E. Leary, M. T. Gonzalez, G. Rubio-Bollinger, C. J. Lambert and N. Agrat, "Engineering the Thermopower of C_{60} Molecular Junctions", *Nano Letters* 13, 2141-2145, 2013.

- [9] K. Gillemot, C. Evangelini, E. Leary, A. La Rosa, M. T. Gonzalez, S. Filippone, I. Grace, G. Rubio-Bollinger, J. Ferrer, N. Martn, C. J. Lambert and N. Agrat, "A Detailed Experimental and Theoretical Study into the Properties of C_{60} Dumbbell Junctions" , *Small*, vol. 9 (22), pp 3812-3822, doi: 10.1002/sml.201300310, 2013.
- [10] A. La Rosa, K. Gillemot, E. Leary, C. Evangelini, M. T. Gonzalez, S. Filippone, N. Agrat, C. J. Lambert, N. Martn, "Does the Cyclopropane Ring Enhance the Electronic Communication in Dumbbell-type C_{60} dimers?" , *The Journal of organic chemistry*, 79, 4871-4877, 2013.

Chapter 2

Density Functional Theory

In order to understand the transport of electrons through organic molecular wires, we need to understand the electronic properties of the isolated molecule. More specifically, solving the many body Schrodinger equation to find the eigenvalues, eigenfunctions, Hamiltonian and overlap matrices that can be used to calculate the electron scattering matrix. Solving such an equation for any system with more than a few electrons proves impossible. However, a number of other techniques can be employed to reduce the complexity of the problem. One type involves first-principles *ab – initio* methods that are based on a purely theoretical formalism, while another employs semi-empirical methods that fit various parameters to experimental data. This thesis uses *ab – initio* methods to provide a consistent systematic method of calculating the electronic structure [1–4].

Density functional theory (DFT) is a well-known *ab – initio* technique, which can efficiently deal with systems containing large numbers of atoms. As the focus of this study is on the electronic properties of large molecules, DFT is a sensible choice to obtain eigenvalues and a Hamiltonian efficiently, taking advantage of modern computational power and numerical techniques. In practice DFT is an approximate method, however, there are lots of examples where the theoretical calculations agree with experimental results [5], however, caution needs to be applied when interpreting results produced using this method. Here I will summarise the main details of DFT and introduce the DFT code SIESTA [6].

2.1 Many - body Hamiltonian

In solid state physics the final target is to find a solution to the time-independent, non-relativistic Schrodinger equation

$$\hat{H}\Psi(r_1, \dots, r_N, R_1, \dots, R_M) = E\Psi(r_1, \dots, r_N, R_1, \dots, R_M) \quad (2.1)$$

where \hat{H} is the Hamiltonian operator of a system consisting of M nuclei and N electrons, r_i is the position of the i - th electron, and R_I the position of the I - th nucleus. Molecules are an excellent example of the complexity of a many body system. Systems consisting of one or two particles can be solved analytically and numerical methods can solve systems an order of magnitude higher. However, larger systems are almost impossible to solve due to the computational time and memory requirements of the calculations. This can be appreciated by looking at the general many body Hamiltonian of a molecule containing N interacting electrons (lower case) and M nuclei (upper case) as shown in the following equation (2.2)

$$\begin{aligned} \hat{H} = & \sum_{i=1}^N -\frac{\nabla_i^2}{2m_i} + \sum_{I=1}^M -\frac{\nabla_I^2}{2M_I} + \frac{1}{2} \sum_{i \neq j}^N \frac{e^2}{4\pi\epsilon_o |r_i - r_j|} + \frac{1}{2} \sum_{I \neq J}^M \frac{e^2 Z_I Z_J}{4\pi\epsilon_o |R_I - R_J|} \\ & - \sum_{iI=1}^{NM} \frac{Z_I e^2}{4\pi\epsilon_o |r_i - R_I|} \end{aligned} \quad (2.2)$$

where:

m_i the mass of the i - th electron

M_I the mass of the I - th nuclei

ϵ_o the dielectric constant of vacuum

e the charge of the electron

Z_I the atomic number of the I - th nucleus. In the equation, the first and second terms are the kinetic energies of the electrons and nuclei respectively, the third is the electron-electron interaction (half for double counting), the fourth the nuclei-

nuclei interactions, and finally the electron-nuclei interactions. Unlike the simple hydrogen atom, solving the Schrodinger equation with this Hamiltonian is impossible as the interaction terms cannot be directly uncoupled and independently solved. An approximation has to be applied to enable a separation of the nucleon and electron degrees of freedom to reduce the size of the problem. That can be achieved through the Born-Oppenheimer approximation.

2.2 Born - Oppenheimer approximation

The electron structure adiabatically follows the changes of nuclear configuration as electrons are lighter than nuclei. The solution of the Schrodinger equation (2.1) with the many-body Hamiltonian (2.2) is a wave function that depends on the coordinates of all the electrons and nucleons i.e $3N + 3M$ variables. To find such a wavefunction is impossible at first, but Born and Oppenheimer [7] demonstrated that it is possible to divide the Hamiltonian into independent nucleon and effective electron pairs, so as to solve the equation independently. As the mass of the electron is significantly smaller than that of the nucleons their velocities are much higher, the electronic structure adiabatically follows the changes of the nuclear configuration. Therefore, the nuclei wavefunction can be assumed to be independent of the electron's position. With this idea in mind, the solution of (2.1) can be written as the product of an independent nuclei χ and electron wavefunction Φ

$$\Psi(r_i, R_I) = \chi(R_I)\Phi(r_i, R_I)$$

inserting this formula into equation (2.2) gives:

$$\begin{aligned}
 & \chi(R_I) \sum_i \left(-\frac{\hbar^2}{2m_i} \nabla_i^2 \right) \Phi(r_i, R_I) + \sum_I \left(-\frac{\hbar^2}{2M_I} \nabla_I^2 \right) \chi(R_I) \Phi(r_i, R_I) \\
 & + \chi(R_I) \frac{1}{2} \frac{1}{4\pi\epsilon_o} \sum_{i,j,i \neq j} \frac{e^2}{|r_i - r_j|} \Phi(r_i, R_I) + \frac{1}{2} \frac{1}{4\pi\epsilon_o} \sum_{I,J,I \neq J} \frac{e^2 Z_I Z_J}{|R_I - R_J|} \chi(R_I) \Phi(r_i, R_I) \\
 & - \frac{1}{4\pi\epsilon_o} \sum_{i,I} \frac{Z_I e^2}{|r_i - R_I|} \chi(R_I) \Phi(r_i, R_I) = E \chi(R_I) \Phi(r_i, R_I)
 \end{aligned} \tag{2.3}$$

In equation (2.3) the second term can be expanded by using the product rule of a differential operator

$$\begin{aligned}
 \nabla_I^2 [\chi(R_I) \Phi(r_i, R_I)] &= \chi(R_I) \nabla_I^2 \Phi(r_i, R_I) + 2 \nabla_I \chi(R_I) \nabla_I \Phi(r_i, R_I) \\
 &+ \Phi(r_i, R_I) \nabla_I^2 \chi(R_I)
 \end{aligned} \tag{2.4}$$

The first term in equation (2.4) depends on the variation of the electronic wavefunction as a function of the nuclei positions, which is taken to be zero, as the nuclei are seen as stationary within the relaxation time of the electrons. The second term represents the electron-phonon interaction which can be canceled by assuming low temperatures. Then we are left with a single term, and substituting that into the full Schrodinger equation yields

$$\begin{aligned}
 & \left\{ \hat{H}_e \Phi(r_i, R_I) + \sum_I \Phi(r_i, R_I) \left(-\frac{\hbar^2}{2M_I} \nabla_I^2 \right) + \frac{1}{2} \frac{1}{4\pi\epsilon_o} \sum_{I,J,I \neq J} \frac{e^2 Z_I Z_J}{|R_I - R_J|} \right. \\
 & \left. \Phi(r_i, R_I) \right\} \chi(R_I) = E \Phi(r_i, R_I) \chi(R_I)
 \end{aligned} \tag{2.5}$$

where

$$\begin{aligned}
 \hat{H}_e &= \sum_i \left(-\frac{\hbar^2}{2m_i} \nabla_i^2 \right) + \frac{1}{2} \frac{1}{4\pi\epsilon_o} \sum_{i \neq j} \frac{e^2}{|r_i - r_j|} - \frac{1}{4\pi\epsilon_o} \sum_{i,I} \frac{e^2 Z_I}{|r_i - R_I|} \\
 &= \hat{T} + \hat{V}_{ee} + \hat{V}_{Ne}
 \end{aligned} \tag{2.6}$$

(2.6) is an effective Hamiltonian, that describes the electron's motion in a constant positive background potential caused by the stationary nuclei, and is defined through the following Schrodinger equation

$$\hat{H}_e\phi = E_e\phi$$

Multiplying (2.5) by Φ^* summing over all i and integrating over the electron position, the nuclei Schrodinger equation

$$\hat{H}_N\chi = E_N\chi$$

can be obtained, with the nuclei Hamiltonian \hat{H}_N containing only the kinetic and interaction terms of the nuclei

$$\hat{H}_N = \sum_I \left(-\frac{\hbar^2}{2M_I} \nabla_I^2 \right) + \frac{1}{2} \frac{1}{4\pi\epsilon_0} \sum_{I \neq J} \frac{e^2 Z_I Z_J}{|R_I - R_J|} + E_e(R_I)$$

The total energy of the system is simply the sum of the two energies

$$E = E_e + E_N$$

Thus, the Born-Oppenheimer approximation allows the electron and nuclei degrees of freedom to be separated. The general method in solving the system of electrons and nuclei is to first solve the electron Hamiltonian using either the Density Functional Theory, Hartree, Hartree-Fock or other quantum mechanical methods, and then treating the nucleon equation as classical equations of motion. A DFT based method for solving only effective electron Hamiltonian will be described later in this chapter.

2.3 Hohenberg - Kohn theorems

Density functional theory describes the method of solving the effective electron Schrodinger equation defined by H_e in (2.6). It is based on two theories constructed originally by Hohenberg and Kohn [8], that show there is unique ground state density of the system n_o which refers to a minimum of the total energy functional. The Hohenberg-Kohn theorems state that for system of interacting particles in an external potential:

- 1- The external potential is uniquely defined (except for a constant) by the ground state particle density n_o and is considered a functional of the density.
- 2- The density can be used to minimize variationally a total energy functional with the global minimum corresponding to the ground state density.

The two theorems can be simply derived by applying a restriction that the system is non-degenerate, however a more general analysis has been performed by Levy [9] and Leib [10] which lead to the same conclusions.

The first theorem can be realised by considering two hypothetical Hamiltonians \hat{H}_1 and \hat{H}_2 which contain two different external potentials (V_1 and V_2) that produce the same ground state density $n_o(r)$. These Hamiltonians form the Schrodinger equations in

$$\begin{aligned}\hat{H}_1\psi_1 &= E_1\psi_1, \\ \hat{H}_2\psi_2 &= E_2\psi_2\end{aligned}$$

As ψ_2 is not the ground state wavefunction of \hat{H}_1 the equality in (2.7) holds for non-degenerate systems (Levi Lieb's derivation does not use this assumption).

$$\langle\psi_1 | \hat{H}_1 | \psi_1\rangle < \langle\psi_2 | \hat{H}_1 | \psi_2\rangle \tag{2.7}$$

The second term can be rewritten in terms of the eigenvalues E_2 of \hat{H}_2 and external potentials.

$$\begin{aligned} \langle \psi_2 | \hat{H}_1 | \psi_2 \rangle &= \langle \psi_2 | \hat{H}_2 | \psi_2 \rangle + \langle \psi_2 | \hat{H}_1 - \hat{H}_2 | \psi_2 \rangle \\ &= E_2 + \int [V_1(r) - V_2(r)] n_o(r) d^3r \end{aligned} \quad (2.8)$$

When (2.8) is substituted back into (2.7) and the whole procedure is repeated for the term $\langle \psi_2 | \hat{H}_2 | \psi_2 \rangle$ (i.e. $\langle \psi_2 | \hat{H}_2 | \psi_2 \rangle < \langle \psi_1 | \hat{H}_2 | \psi_1 \rangle$), two inequalities in (2.9) are produced.

$$\begin{aligned} E_1 &< E_2 + \int [V_1(r) - V_2(r)] n_o(r) d^3r \\ E_2 &< E_1 + \int [V_2(r) - V_1(r)] n_o(r) d^3r \end{aligned} \quad (2.9)$$

Finally, adding together the two expressions in (2.9) produces the contradicting inequality $E_1 + E_2 < E_1 + E_2$, showing that there can not be two external potentials differing by more than a constant which lead to the same non-degenerate ground state particle density. Therefore each different external potential is defined uniquely by a unique ground state density.

In the same way, the second term can be understood in a similar way [11], which links to the minimisation of a total energy functional. The first Hohenberg-Kohn theorem states, that the density can uniquely determine the external potential, which determines the Hamiltonian, which is used to find the wavefunctions of the system. This, therefore means that the wavefunction is a functional of the density. Thus, the expectation value E of the system Hamiltonian \hat{H}_e is also a functional of the density.

$$\langle \Phi[n] | \hat{H}_e | \Phi[n] \rangle = \langle \Phi[n] | \hat{T} | \Phi[n] \rangle + \langle \Phi[n] | V_{ee} | \Phi[n] \rangle + \langle \Phi[n] | V_{Ne} | \Phi[n] \rangle$$

The ground state energy can be found by applying the variational principle to minimise this expectation value with respect to the wavefunction ϕ of the effective

electron Hamiltonian.

$$E = \min_{\Phi} (\langle \Phi | \hat{H} | \Phi \rangle) = \min_{n|\Phi} \left(\underbrace{F[n] + \int V_{ext}(r)n(r)d^3r}_{\text{}} \right)$$

where

$$E[n] = F[n] + \int V_{ext}(r)n(r)d^3r$$

$$F[n] = \langle \Phi | \hat{T} | \Phi \rangle + \langle \Phi | \hat{V}_{ee} | \Phi \rangle \equiv T[n] + E_{int}[n]$$

describes the kinetic energy and electron-electron interaction energy functionals respectively. Here, the minimisation is carried out with respect to the density, corresponding to the system wavefunction Φ which is equivalent to minimising with respect to the wavefunction alone. If the density does not correspond to the ground state, the corresponding wavefunction is not the ground state wavefunction and therefore the expectation value will not correspond to the ground state energy of the system.

2.4 Kohn - Sham equations and self consistency

Kohn and Sham solved the interacting system problem by mapping the interacting system in an external potential onto a set of fictitious single particle, non-interacting systems containing a new effective potential $V_{eff}(r)$ [12]. This can then be solved directly. The new effective electron potential can be identified by comparing results from a non-interacting system to that of an interacting system. The full energy functional of a non-interacting system can be written in terms of the external potential and the energy functional consisting of the non-interacting kinetic energy functional only $F_{ni}[n] = T_{ni}[n]$

where $T_{ni}[n] = \langle \Phi_{ni}[n] | \hat{T} | \Phi_{ni}[n] \rangle$ is the kinetic energy functional evaluated for

a non-interacting wavefunction

$$E_{ni}[n(r)] = F_{ni}[n(r)] + \int V_{ext}(r)n(r)d^3r \quad (2.10)$$

following from the Hohenberg-Kohn theories, the ground state density will correspond to the minimum of the energy functional or equivalently where the functional derivative $\frac{\delta}{\delta n(r)}$ of $E_{ni}[n(r)]$ is zero. The density is under the additional constraint that it has to be normalized to the number of electrons N in the system

$$\int n(r)d^3r = N \quad (2.11)$$

It is now possible to minimize (2.10) with respect to the density under the constraint (2.11), which produces the Euler equation

$$\frac{\delta}{\delta n(r)} \left\{ T_{ni}[n] + \int V_{ext}(r')n(r')d^3r' - \epsilon \left[\int n(r')d^3r' - N \right] \right\} = 0$$

that is

$$\frac{\delta T_{ni}[n]}{\delta n(r)} + V_{ext}(r) - \epsilon = 0, \quad (2.12)$$

with the Lagrange multiplier ϵ corresponding to the Schrodinger equation

$$\left(-\frac{\hbar^2}{2m_i} \nabla_i^2 + V_{ext}(r) \right) \phi_i = \epsilon_i \phi_i \quad (2.13)$$

For the fully interacting system, instead of the energy functional $F_{ni}[n]$ in (2.10) an extended term $F[n]$ comes up, that contains two extra energy functionals

$$F[n] = T_{ni}[n] + E_H[n] + E_{xc}[n],$$

corresponding to the interacting $T[n]$, and the interaction between the electrons. The electron-electron interaction has been split into two terms, the Hartree func-

tional E_H

$$E_H[n] = \frac{1}{2} \frac{1}{4\pi\epsilon_o} \int \frac{n(r)n(r')}{|r-r'|} d^3r d^3r',$$

and the exchange-correlation functional E_{xc} . The former stems from the classical Hartree potential which includes an electron self-interaction term. The latter includes all other many body effects, and is defined explicitly as

$$E_{xc}[n] = T[n] - T_{ni}[n] + E_H[n] + E_{ee}[n]. \quad (2.14)$$

following the minimization procedure as before for the non-interaction system, the functional derivative of the different functionals is taken

$$\frac{\delta}{\delta n(r)} \left\{ T_{ni}[n] + \int V_{ext}(r')n(r')d^3(r') + \frac{1}{2} \frac{1}{4\pi\epsilon_o} \int \frac{n(r')n(r'')}{|r-r'|} d^3r' d^3r'' + E_{xc}[n] - \alpha \left[\int n(r')d^3r' - N \right] \right\}$$

This leads to the modified Euler equation for the interacting system

$$\frac{\delta T_{ni}[n]}{\delta n(r)} + V_{KS}(r) - \epsilon^{KS} = 0, \quad (2.15)$$

which looks like that of the non-interacting system (2.12), with a different external potential, namely the Kohn-Sham potential $V_{KS}(r)$ defined by the equation

$$V_{KS}(r) = \frac{1}{4\pi\epsilon_o} \int \frac{n(r')}{|r-r'|} d^3r' + V_{xc}(r) + V_{ext}(r).$$

Which means (2.15) corresponds to a set of single particle, non-interacting Schrodinger equations in the presence of an effective single electron potential V_{KS} , which includes the many-body effects. The total energy functional can be found in terms of the eigenvalues of the Kohn-Sham equations. This is achieved by comparing (2.13) with the eigenvalues of

$$\left(-\frac{\hbar^2}{2m_i} \nabla_i^2 + V_{KS}(r) \right) \psi_i^{KS} = \epsilon_i^{KS} \psi_i^{KS}$$

This means that three terms have to be subtracted to get the total energy

$$E[n] = \sum_i \epsilon_i - \frac{1}{2} \frac{1}{4\pi\epsilon_0} \int \frac{n(r)n(r')}{|r-r'|} d^3r' d^3r - \int V_{ext}(r)n(r)d^3(r) - E_{xc}[n]. \quad (2.16)$$

In the Kohn-Sham formalism no approximation have been assumed, so (2.16) is exact if the exchange-correlation functional is known exactly. As a result of the Hohenberg-Kohn theorems the ground state density can be found by carrying out a self-consistent cycle shown in figure 2.1.

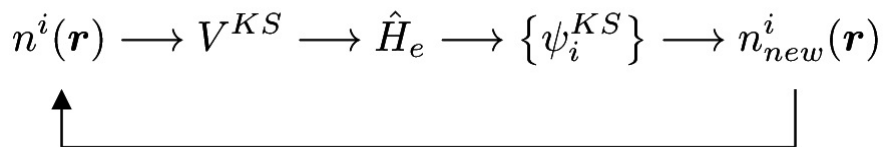


Figure 2.1: Schematic of the self consistent DFT cycle starting from an initial density $n^i(r)$, which is used to calculate the Kohn-Sham potential V_{KS} , Hamiltonian \hat{H}_e and wavefunctions $\{\Psi_i^{KS}\}$ of the system. This allows a new density $n_{new}^i(r)$ to be calculated, and the cycle is repeated until convergence is achieved

where the electron density is expressed as

$$n(r) = \sum_i f_i |\Psi_i^{KS}(r)|^2$$

with f_i being the occupancy of the orbital, which can be 1 for half filled orbitals, 0 for empty orbitals and 2 for an orbital with two electrons on it.

This shows that if the density is known, the energy functional is fully determined. An arbitrary starting density can be diagonalized to find the eigenfunctions, which in turn can be used to find the density. The procedure is repeated until the output density and the input densities are equivalent within a predetermined tolerance.

The Kohn-Sham approach clearly shows that a complicated many body system can be mapped onto a set of simple non-interacting equations exactly if the exchange correlation functional is known. Due to the formulation of the theory, only groundstate quantities are correctly calculated such as: groundstate energy,

groundstate density, the fictitious Kohn-Sham eigenvalues and the groundstate electron geometry. Therefore, DFT cannot be used to calculate higher energetic states correctly such as the lowest unoccupied orbital of a molecule, and thus underestimates band gaps in semiconductors. It is important to note that DFT remains an approximate technique of finding these ground state properties, as the exchange-correlation functional is not known exactly, so approximations have to be made.

2.5 Exchange and correlation

The exchange-correlation functional $E_{xc}[n]$ contains all of the complicated, many body parts of the electron-electron interaction and is therefore quite complex in itself. An exact form is unknown, but numerous approximations have been made to various degrees of accuracy in an attempt to obtain comparable results with experimental data.

These approximations range from the local density approximation (LDA) [12], where the exchange-correlation functional depends only on the density, to the more complicated generalised gradient approximations (GGA) of various degrees of accuracy, where the exchange-correlation functional depends on both the density and its gradients, to the even more complex, and specific, but for certain systems far more accurate hybrid functionals, e.g. B3LYP [13–16] and HSE [17], or to even functionals with van der Waals interactions included [18]. In this section, I will derive some relations which this exchange-correlation functional must obey and explain how these functionals are constructed.

The exchange-correlation functional is defined as the difference between the interacting and non-interacting minimised values of the kinetic plus electron interaction functionals (2.14). If a parameter λ is introduced such that $\lambda = 1$ corresponds to the full interacting system, and $\lambda = 0$ to the non-interacting system, then the exchange-correlation functional $E_{xc}[n]$ can be written in terms of the difference between the interacting and non-interacting systems (where E_H is the Hartree

functional) as shown in (2.17).

$$E_{xc}[n] = \langle \psi_\lambda | \hat{T} + \lambda \hat{V}_{ee} | \psi_\lambda \rangle_{\lambda=1} - \langle \psi_\lambda | \hat{T} + \lambda \hat{V}_{ee} | \psi_\lambda \rangle_{\lambda=0} - E_H[n] \quad (2.17)$$

If λ is taken to be continuous then the first two terms in (2.17) can be simplified into an integral fictitiously representing the adiabatic turning-on of the electron-electron interaction.

$$E_{xc}[n] = \int_0^1 \frac{d}{d\lambda} \langle \psi_\lambda | \hat{T} + \lambda \hat{V}_{ee} | \psi_\lambda \rangle d\lambda - E_H[n] \quad (2.18)$$

The equation can be further simplified by applying the Hellmann-Feynman theorem [19]. This shows that if a Hamiltonian depends on a parameter λ , then any normalised eigenstate ϕ_λ which also depends on that parameter, the following equation holds.

$$\frac{d}{d\lambda} \langle \phi_\lambda | \hat{H}_\lambda | \phi_\lambda \rangle = \langle \phi_\lambda | \frac{\hat{H}_\lambda}{d\lambda} | \phi_\lambda \rangle$$

This can be applied to equation (2.18) to produce

$$E_{xc}[n] = \int_0^1 \langle \phi_\lambda | \hat{V}_{ee} | \phi_\lambda \rangle d\lambda - E_H[n]$$

Before proceeding we need to define a joint probability of finding an electron in a volume d^3r and another in volume d^3r'

$$P(r, r') = \rho_\lambda(r, r') d^3r d^3r'$$

where the reduced density matrix is defined by

$$\rho_\lambda(r, r') = N(N-1) \int d^3r_2 \dots \int d^3r_N \phi_\lambda(r, r', r_2, \dots, r_N)^2$$

Using this the new form of the exchange-correlation functional is

$$E_{xc}[n] = \int_0^1 \int d^3r \int d^3r' \frac{1}{2} \frac{1}{4\pi\epsilon_0} \frac{\rho_\lambda(r, r')}{|r - r'|} d\lambda - E_H[n] \quad (2.19)$$

Thus, the groundstate value of the two-body operator \hat{V}_{ee} is represented in a much more convenient way. Using basic statistical theory, the density matrix can be expressed as the product of two terms

$$\rho_\lambda(r, r') = n(r)n_2^\lambda(r|r')$$

with $n(r)$ being the probability of finding an electron at r , and $n_2^\lambda(r|r')$ being the conditional probability of finding an electron at r' given that there is one at r . This conditional probability can be viewed as the averaged electron density at r' given that there is an electron at r . These two densities have the normalisation conditions

$$\int d^3r n(r) = N \tag{2.20}$$

$$\int d^3r' n_2^\lambda(r'|r) = N - 1 \tag{2.21}$$

Finally, n_2 can be separated into two terms $n_2^\lambda(r'|r) = n(r') + n_{xc}^\lambda(r, r')$ a single particle probability and a new conditional probability called the "exchange-correlation hole", n_{xc}^λ which must have the normalisation condition in order to satisfy equations (2.20) and (2.21).

$$\int d^3r' n_{xc}^\lambda(r, r') = -1 \tag{2.22}$$

Therefore the initial reduced density matrix is simplified to

$$\rho_\lambda(r, r') = n(r)n(r') + n(r)n_{xc}^\lambda(r, r')$$

Substituting the above equation into (2.19), the classical Hartree terms are canceled to reduce the exchange-correlation functional to

$$\begin{aligned} E_{xc}[n] &= \int_0^1 d\lambda \int d^3r \int d^3r' \frac{1}{2} \frac{1}{\pi\epsilon_0} \frac{n(r)n_{xc}^\lambda(r, r')}{|r - r'|} \\ &= \int d^3r \int d^3r' \frac{1}{2} \frac{1}{\pi\epsilon_0} \frac{n(r)\bar{n}_{xc}(r, r')}{|r - r'|} \end{aligned} \tag{2.23}$$

Where we have defined the coupling-constant averaged hole density as

$$\bar{n}_{xc}(r, r') = \int_0^1 n_{xc}^\lambda(r, r') d\lambda$$

This equation shows that the exchange-correlation energy equals the electrostatic interaction between each electron and the coupling-constant averaged exchange-correlation hole that surrounds it. This "hole" is created due to three effects:

- 1- The Pauli exclusion principle.
- 2-The unphysical self-interaction correction (i.e. such that one electron cannot interact with itself.)
- 3- The Coulomb repulsion, the first two effects contribute to the exchange, and the third to the correlation. It is worthwhile to note that if DFT was exact, then self interaction effects would not be present.

In order to have an accurate exchange-correlation functional, a suitable form of the exchange-correlation hole must be known. There is a considerable area of research into finding different forms of the exchange-correlation hole, however I will summarise the approach used by the local density approximation (LDA).

2.5.1 Local Density Approximation

The simplest approximation of the exchange-correlation functional is the local density approximation (LDA) which was first introduced by Kohn and Sham [12]. They showed that for a system with a relatively slowly varying density, the exchange-correlation hole in (2.23) can be approximated to be dependent only on the local density $n(r)$. The exchange-correlation functional in this case can be expressed in terms of the exchange-correlation energy per electron in a uniform electron gas $\varepsilon_{xc}^{uni}[n(r)]$ with a density $n(r)$.

$$E_{xc}[n(r)] \approx E_{xc}^{LDA}[n(r)] = \int n(r) \varepsilon_{xc}^{uni}[n(r)] d^3r$$

The idea is to assume that the inhomogeneous electron density is smooth enough, that in the vicinity of a point the electron density can be seen as constant. ε_{xc}^{uni} can then split into a sum of the exchange ε_x^{uni} and correlation ε_c^{uni} energies

$$\varepsilon_{xc}^{uni}[n(r)] = \varepsilon_x^{uni}[n(r)] + \varepsilon_c^{uni}[n(r)]$$

which can be found separately. Analytical expressions for the exchange term are well known [20]

$$\varepsilon_x^{uni}[n(r)] = -\frac{3}{4} \left(\frac{3n(r)}{\pi} \right)^{\frac{1}{3}}$$

The form of the correlation term cannot be found by analytical means. Rather, the correlation term needs to be parameterised and then fitted to Monte-Carlo simulations at different densities. There have been a number of calculations on this matter, however, the most accurate results lie with the parametrisation by Ceperley and Alder [21] or Perdew and Zunger [22]. The resulting exchange-correlation potential produces relatively accurate results for systems with well behaved densities.

The main problem with the LDA is the spurious "self-interaction" error. In Hartree-Fock theory the self-term in the Hartree term (i.e one electron interacting with its own potential) is cancelled out by the non-local exchange term, however in LDA this term is only partially cancelled. This partial cancellation can therefore produce large errors in systems where electrons are localised close together, however this effect is reduced in systems where there is delocalised electrons. Despite this, LDA produces relatively accurate results even for non-homogeneous systems because

- 1- The exchange-correlation hole always obeys the normalisation rule (2.22).
- 2- The exact shape of the exchange-correlation hole does not have to be correct as the exchange-correlation functional can be shown to depend only on it's spherical

average, i.e. (2.23) can be transformed with $R = r - r'$

$$E_{xc} = \int d^3r n(r) \int d^3r' \frac{1}{2} \frac{1}{4\pi\epsilon_0} \frac{\bar{n}_{xc}(r, r')}{|r - r'|} = \frac{1}{\epsilon_0} \int d^3r n(r) \int_0^\infty \frac{1}{2} R^2 \frac{1}{R} dR \int_\Omega \bar{n}_{xc} d\Omega$$

This concludes the brief derivation of the core components of DFT. In essence it is possible to now solve the Schrodinger equation for a fully interacting system as long as a suitable exchange-correlation functional is defined.

2.6 SIESTA technique

From a large number of DFT codes and methods, the SIESTA [23] (Spanish Initiative for Electronic Simulations with Thousands of Atoms) numerical code was chosen to perform all electronic structure calculations in this thesis. SIESTA is designed to perform efficient calculations on large systems consisting of thousands of atoms by utilising methods such as a linear combination of atomic orbital (LCAO) basis, norm-conserving pseudopotentials and use of a periodic supercell. This section will briefly describe the importance of these methods and how they are implemented within the code.

2.6.1 Norm-conserving pseudopotentials

By defining an exchange-correlation functional within the Kohn-Sham formalism, it is possible to split a large interacting problem into a large effective non-interacting problem. From a physical viewpoint, this vastly simplifies the problem. However, in typical systems of molecules which contain many atoms, the calculation is still very large and has the potential to be computationally intensive. In order to reduce the number of electrons, one can introduce pseudopotentials which effectively remove the core electrons from an atom. Pseudopotentials were first introduced by Hans Hellmann in 1935 [24] and since then methods have evolved from creating not so realistic empirical pseudopotentials [25, 26] to more realistic ab-initio pseudopotentials [27].

The electrons in an atom can be split into one of two types: core and valence, where core electrons lie within filled atomic shells and the valence electrons lie in partially filled shells. Core electrons are spatially localized close to the nucleus, so when atoms are brought together mostly only their valence electron states will overlap. This allows the core electrons to be removed and replaced by a pseudopotential, such that the valence electrons still feel the same screened nucleon charge as if the core electrons were still present. This reduces the number of electrons in a system dramatically and in turn reduces the time and memory required to calculate properties of molecules, that contain a large number of electrons. In the SIESTA code a special type of ab-initio pseudopotential, called the norm-conserving pseudopotential [28] is implemented.

To generate pseudopotentials, the Kohn-Sham formalism can be used to solve the many electron problem for a single atom. From the single atom solutions one can calculate the pseudopotential that can replace the effect of the core electrons. It has to be noted, that for general use an assumption has to be made, that if the atom is not alone in vacuum, but in a complex environment surrounded by other atoms, then the pseudopotential is still applicable.

Let's take the wavefunction of a single valence electron state in an arbitrary, spherically symmetric potential (like an atom). This can always be split into a radial and an angular part, $\psi_{nlm}^{AE}(r) = R_{nl}^{AE}(r)Y_{lm}(\theta, \varphi)$, where $Y_{lm}(\theta, \varphi)$ is the spherical part and is a spherical harmonic function. The subscript *AE* refers to 'all-electron' wavefunction. The radial part R_{nl}^{AE} is the solution to the radial Schrodinger equation (2.24)

$$\left[-\frac{1}{2r} \frac{d^2}{dr^2} + \frac{l(l+1)}{2r^2} + V_{nl}^{AE}(r) \right] R_{nl}^{AE}(r) = \epsilon_{nl}^{AE} R_{nl}^{AE}(r) \quad (2.24)$$

where V_{nl}^{AE} is the usual Coulomb potential, which includes all interactions with the remaining core and valence electrons in the atom. To reduce the size of the system, it is possible to remove the core electrons and replace the all-electron potential in (2.24) by a pseudopotential V^{PS} , such that the valence electrons feel

the same interactions as if they were still present. By doing this, the solutions to (2.24) will be changed to the radial pseudo-wavefunction R_{nl}^{PS} . The method of finding this pseudopotential is to first construct the pseudo-wavefunctions R_{nl}^{PS} from the all-electron R_{nl}^{AE} wavefunctions, and then calculate the pseudopotential by inverting the radial Schrodinger equation (2.24)

$$V_{nl}^{PS} = \epsilon_{nl}^{PS} - \frac{l(l+1)}{2r^2} + \frac{1}{2r} \frac{1}{R_{nl}^{PS}(r)} \frac{d^2}{dr^2} (r R_{nl}^{PS}(r)) \quad (2.25)$$

So, how is the radial part of the pseudowavefunction determined? There is no set answer to this, however there are a number of different ways of parameterising the pseudo-wavefunction. In SIESTA, the Troullier-Martins method [29,30] is applied, where the pseudo-wavefunction is defined below the cut-off radius r_c as a function of a polynomial in r^2

$$p(r) = a_0 + a_2 r^2 + a_4 r^4 + a_6 r^6 + a_8 r^8 + a_{10} r^{10} + a_{12} r^{12}$$

as shown in equation (2.26).

$$R_{nl}^{PS} = \begin{cases} R_{nl}^{AE} & r > r_c \\ r^l e^{p(r)} & r < r_c \end{cases} \quad (2.26)$$

For the resulting pseudopotential to be classified as norm-conserving, the following rules must be obeyed by radial part of the pseudo-wavefunction:

1. Above some cut-off radius r_c the pseudo-wavefunction and all-electron wavefunction should be equal.

$$R_{nl}^{PS} = R_{nl}^{AE} \quad r > r_c$$

2. The pseudo-wavefunction should be smooth and nodeless to produce a smooth pseudopotential. This is done by making R_{nl}^{PS} and its first four derivatives continuous at the cut-off radius.

3. The eigenvalues of the pseudo and all electron wavefunctions should be equal.

$$\epsilon_{nl}^{PS} = \epsilon_{nl}^{AE}$$

4. The charge enclosed inside r_c should be equal for both all-electron and pseudo wavefunctions.

$$\int_0^{r_c} |rR_{nl}^{PS}(r)|^2 dr = \int_0^{r_c} |rR_{nl}^{AE}(r)|^2 dr$$

The resulting pseudopotential can be found by substituting equation (2.26) into the inverted Schrodinger equation (2.25)

$$V_{nl}^{PS} = \begin{cases} V_{nl}^{AE} & r > r_c \\ \epsilon_{nl}^{PS} + \frac{(l+1)p'(r)}{r} + \frac{1}{2}(p'(r) + p''(r)) & r < r_c \end{cases}$$

Therefore, the pseudopotential can be determined if the coefficients in (2.26) are known. These are found from seven conditions found in points 1, 2 and 4, with the additional constraint that the second derivative of the pseudopotential is zero. If these conditions are satisfied, the resulting pseudopotential will be smooth and nodeless, producing a rapid convergence of calculations [30].

The pseudopotential obtained in this way is called "screened pseudopotential", because it includes effects from both core and valence electrons. In order to make it transferable to other environments (i.e. used in molecules), one has to partition off any screening from the valence electrons. This can be done by making the assumption, that the exchange-correlation potential is additive and separable into core and valence terms. Then by subtracting the Hartree and exchange-correlation potentials due to the presence of the valence electrons the following ion potential is obtained

$$V_{nl}^{ion}(r) = V_{nl}^{PS}(r) - V_H[n^{PS}] - V_{xc}[n^{PS}] \quad (2.27)$$

where n^{PS} is the valence part of the full self-consistent charge density. Note that this potential depends on the exchange-correlation functional, so in general

pseudopotentials for the different approximations for the exchange-correlation are not the same (like e.g. for LDA and GGA).

2.6.2 Localized basis

One of the most important features of the SIESTA code is the type of basis functions used in the calculations. Looking back at the self-consistent cycle in Figure 2.1, it can be seen that in order to find the wavefunctions, the Hamiltonian has to be diagonalized. This process involves the inversion of a large matrix whose computation time scales with the number of non-zero elements. Therefore, for efficient calculations the Hamiltonian is required to be sparse with many zeros. As mentioned before SIESTA utilizes a Linear Combination of Atomic Orbital (*LCAO*) basis set, whose elements are constrained to be zero after some defined cut-off radius, and are constructed from the orbitals of the atoms. The former produces the required sparse form of the Hamiltonian, as the overlap between basis functions is reduced, and the latter allows even a minimal size basis set to produce properties close to that of the studied system (unlike for plane wave basis sets). The simplest basis set for an atom is called a *single* – ζ basis, which corresponds to a single basis function $\psi_{n|m}(r)$ per electron orbital (i.e. 1 for s, 3 for p,... etc.)

$$\psi_{n|m}(r) = \phi_{nl}^1(r)Y_{lm}(\theta, \varphi)$$

In this case each basis function consists of a product of one radial wavefunction ϕ_{nl}^1 and one spherical harmonic Y_{lm} . The radial part of the wavefunction is found by using the method proposed by Sankey [31], where the following Schrodinger equation is solved for the atom placed inside a spherical box

$$\left[\frac{1}{2r} \frac{d^2}{dr^2} + \frac{l(l+1)}{2r^2} + V_{nl}^{ion}(r) \right] r\phi_{nl}^1(r) = (\epsilon_{nl} + \delta E)r\phi_{nl}^1(r) \quad (2.28)$$

Here, the radial wavefunction is under the constraint to vanish at a cut-off radius r_{cut} . This constraint produces an energy shift δE within the Schrodinger equation

such that the eigenfunction's first node occurs at r_{cut} .

For higher accuracy basis sets (*multiple* – ζ) additional radial wavefunctions can be included for each electron orbital. The additional radial wavefunctions $\{\phi_{nl}^i\}$ for $i > 1$ are calculated using a split-valence method. This involves defining a split valence cut-off r_s^i for each additional wavefunction, so it is split into two piecewise functions: a polynomial below the cut-off, and the previous basis wavefunction above it as shown in the equation

$$\phi_{nl}^i(r) = \begin{cases} r^l(a_1 - b_l r^2) & r < r_s^i \\ \phi_{nl}^{i-1} & r_s^i < r < r_s^{i-1} \end{cases}$$

The additional parameters are found at the point r_s^i , where the wavefunction and its derivative are assumed continuous.

Further accuracy (*multiple* – ζ *polarized*) can be obtained by including wavefunctions with different angular momenta corresponding to orbitals which are unoccupied in the atom. This is done by solving (2.28) in an electric field such that the orbital is polarized or deformed due to the field (see [23] for details), so a different radial function is obtained. This is now combined with the appropriate angular dependent spherical harmonic, which increases the size of the basis. Table 2.1 shows the number of basis orbitals for a selected number of atoms of *single* – ζ (SZ), *single* – ζ polarised (SZP), *double* – ζ (DZ) and *double* – ζ *polarized* (DZP) basis sets.

Basis set	H	C	Au
SZ	1(1 x 1s)	4(1 x 2s + 3 x 2 p)	6(1 x 6s + 5 x 2 d)
SZP	4(1 x 1s + 3 x 2 p ⁻)	9(1 x 2s + 3 x 2p + 5 x 3d ⁻)	9(1 x 6s + 5 x 5d + 3 x 6p ⁻)
DZ	2(2 x 1s)	8(2 x 2s + 6 x 2p)	12(2 x 6s + 10 x 5d)
DZP	5(2 x 1s + 3 x 2p ⁻)	13(2 x 2s + 6 x 2p + 5 x 3d ⁻)	15(2 x 6s + 10 x 5d + 3 x 6p ⁻)

Table 2.1: Table showing the number of radial basis functions per atom for three elements as used within the SIESTA for different degrees of precision. For clarity the specific orbitals are listed next to each number, with – representing the polarization of that orbital.

Electron Hamiltonian

The electron Hamiltonian generated by SIESTA is the same as in Kohn-Sham formalism and includes the local and non-local parts of the pseudopotential

$$\hat{H} = \hat{T} + \sum_I \hat{V}_I^{KB} + \sum_I \hat{V}_{loc}^I(r) + \hat{V}_H(r) + \hat{V}_{xc}(r) \quad (2.29)$$

Here \hat{T} is the kinetic energy operator, \hat{V}_{loc}^I and \hat{V}_I^{KB} are the local and non-local parts of the pseudopotential for atom I, V_H and V_{xc} the Hartree and exchange-correlation potentials. The first two terms in (2.29) are calculated using two centre integrals in k-space. These are defined by

$$\langle \psi_1 | \hat{O} | \psi_2 \rangle = \int \psi_1^*(k) \hat{O} \psi_2(k) e^{-ik \cdot R} dk$$

which is a Fourier transforms in k-space with ψ_α corresponding to either the basis orbitals (for $\hat{Q} = \hat{T}$) or the Kleinmann-Bylander pseudo-potential projectors (for $\hat{Q} = V_I^{KB}$). The final three terms in (2.29) are calculated on a three-dimensional real space grid with a fineness Δx controlled the a grid-cut off energy ϵ_c which is equivalent to a plane-wave cut off $\epsilon_c = \frac{1}{2} \frac{\pi^2}{\Delta x}$. Within all of our calculations we chose a cut-off energy of 200 Ry which proves to provide sufficient accuracy.

This Hamiltonian is used within the self consistent procedure explained in Section 2.4 to find the ground state density of the system. In order to facilitate conver-

gence, SIESTA has additional options of mixing the density matrix in each cycle. In particular the method of Pulay mixing [32], where the new density is mixed not just with the old density, but a linear combination of the previous n densities.

2.7 Some preparation for SIESTA

In this section, I will briefly summarise the procedure and necessary steps that will be required to obtain acceptable results of the DFT code. Firstly, I will start with building the geometry configuration of the system in order to obtain the optimum configuration. An appropriate pseudopotential must be generated, for each atom in that system, in case the system is periodic, then the lattice vectors should be defined. To make a balance between the accuracy, computational time, as well as memory, we should choose the right basis set for each atom in the system, the smaller basis the less memory and time calculations it will take.

Regarding setting the computational parameters, such as the density convergence tolerance, grid fineness, and Brillouin zone sampling for the k -space integral in the case of periodic systems, these parameters control the accuracy of the numerical procedures and so there is a trade off between the speed of the computation and numerical accuracy. The other type of computational parameters are the convergence parameters, like the so called Pulay parameters, which are responsible for accelerating or maintaining the stability of the convergence.

2.7.1 SIESTA calculations

During the calculation, SIESTA generates the initial charge density based on non-interacting atoms. Since the pseudopotentials are known, it is easy to generate this and the total charge density will be the sum of the atomic densities. In addition to that, the iteration is started by calculating the Hartree potential and the exchange correlation potential. Since the density is represented in real space, the Hartree potential is obtained by solving the Poisson equation with a multi-grid [33, 34],

or fast-Fourier transform method [35], and the exchange-correlation potential is obtained by performing the integrals given in the section 2.5.1. The full iteration cycle is described on Figure 2.1. The iteration process ends when the necessary convergence criteria are reached. As a result the ground state Kohn-Sham orbitals are obtained and the ground state energy for a given atomic configuration. For structural optimization, the procedure described above is in a loop, which is controlled by, e.g., the conjugate gradient method for finding the minimal ground state energy and the corresponding atomic configuration, with the help of DFT, one can obtain an approximation of the electronic structure of the typical molecular systems described in my results.

2.8 Basis Set Superposition Error (BSSE)

The Basis Set Superposition Error (BSSE) was shown for the first time by Kestner [36] for the calculation of a Helium dimer and by Jansen and Ros [37] in 1969, for the protonation of carbon monoxide. The term BSSE was introduced by Liu and McLean in 1973 [38], and it is still being studied and reviewed.

BSSE is present in all molecular electronic structure calculations in which orbitals are approximated by expansion in terms of analytic basis functions centered on different points (usually the nuclei) that are dependent on the geometry of the system being studied. The error arises when two chemical fragments, A and B, approach to form the AB super-molecule. The description of fragment A within the complex can be improved by the functions of fragment B and vice versa, while such an extension is not possible in the calculation of the isolated fragments.

Consequently, in the process $A + B \rightarrow AB$, the total energy decreases due to two factors, first the stabilization of the system due to the fragments interaction and the improvement in the individual atomic description. This second effect (BSSE) is an artifact, which causes an unphysical overestimation of the interaction energy. These errors have been mainly discussed in studies of weak

interactions, such as Van der Waals interactions, and more recently in studies of intramolecular interactions [40,41]. However, let us recall that A and B fragments can be atoms as well as polyatomic species, that is, the BSSE is also present in every chemical bond, as well as it is in weakly bounded dimers. The conventional way to correct for BSSE is based on the Boys - Bernardi [41] counterpoise (CP) scheme. Using the CP correction scheme one has to recalculate the monomers in the basis of the whole supermolecule for every geometrical arrangement. For example, in the case of two interacting monomers A and B, the uncorrected binding or interaction energy ΔE can be calculated as

$$\Delta E = E_{AB}^{AB} - E_A^A - E_B^B \quad (2.30)$$

where E_{AB}^{AB} is the total energy of the complex and E_A^A and E_B^B are the total energies of the monomers.

This chapter has shown the formalism behind DFT along with details of the DFT code SIESTA which is used in all electronic structure calculations in this thesis. This is the first step in all my transport calculations, however the Hamiltonian extracted is still only of the isolated molecule. In order to understand the transport properties of the molecule it has to be connected to semi-infinite leads which in theory produces an infinite problem. The next chapter will introduce the second step in my transport calculations which enables the reduction of a infinite problem to that of a finite system through the retarded Green's function.

Bibliography

- [1] M. J. S. Dewar, E. G. Zoebisch, E. F. Healy, and J. J. P. Stewart, "Development and use of quantum mechanical molecular models. 76. AM1: a new general purpose quantum mechanical molecular model", *Journal of the American Chemical Society*, vol. 107, pp. 3902-3909, June 1985.
- [2] R. Pariser and R. Parr, "A SemiEmpirical Theory of the Electronic Spectra and Electronic Structure of Complex Unsaturated Molecules.I", *The Journal of Chemical Physics* 21, no.3: 466-471, 1953.
- [3] J. J. P. Stewart, "Optimization of parameters for semiempirical methods I. Method", *Journal of Computational Chemistry*, vol. 10, no. 2, pp. 209-220, 1989.
- [4] R. C. Bingham, M. J. S. Dewar and D. H. Loe, "Ground states of molecules. XXVIII. MINDO/3 calculations for compounds containing carbon, hydrogen, fluorine, and chlorine", *Journal of the American Chemical Society* 97, no.6: 1307-1311, 1975.
- [5] N. Troullier and J. L. Martins, "Structural and electronic properties of C_{60} ", *Phys. Rev. B*, vol. 46, pp. 1754-1765, July 1992.
- [6] E. Artacho, E. Anglada, O. Diguez, J. D. Gale, a. Garca, J. Junquera, R. M. Martin, P. Ordejn, J. M. Pruneda, D. Snchez-Portal, and J. M. Soler, "The SIESTA method; developments and applicability", *Journal of physics. Condensed matter : an Institute of Physics journal*, vol. 20, p. 064208, Feb. 2008.

- [7] M. Born, "Born-Oppenheimer Approximation", *Ann. Phys*, vol. 84, pp. 457-484, 1927.
- [8] Gill, MW Peter, B. G. Johnson, J. A. Pople and M. J. Frisch, "The performance of the BeckeLeeYangParr (BLYP) density functional theory with various basis sets." *Chemical Physics Letters* 197.4 : 499-505. 1994.
- [9] M. Levy, "Electron densities in search of Hamiltonians", *Phys. Rev. A*, vol. 26, pp. 1200-1208, Sept. 1982.
- [10] E. H. Lieb, "Density functionals for coulomb systems", *International Journal of Quantum Chemistry*, vol. 24, no. 3, pp. 243-277, 1983.
- [11] J. Slyom, "Fundamentals of the Physics of Solids: Volume 3 - Normal, Broken-Symmetry, and Correlated Systems", *Theoretical Solid State Physics: Interaction Among Electrons*, Springer, 2010.
- [12] W. Kohn and L. J. Sham, "Self-Consistent Equations Including Exchange and Correlation Effects", *Phys. Rev.*, vol. 140, pp. A1133-A1138, Nov. 1965.
- [13] J. P. Perdew, K. Burke, and M. Ernzerhof, "Generalized Gradient Approximation Made Simple", *Phys. Rev. Lett.*, vol. 77, pp. 3865-3868, Oct. 1996.
- [14] A. D. Becke, "Density-functional exchange-energy approximation with correct asymptotic behavior", *Phys. Rev. A*, vol. 38, pp. 3098-3100, Sept. 1988.
- [15] J. P. Perdew and Y. Wang, "Accurate and simple analytic representation of the electron-gas correlation energy", *Phys. Rev. B*, vol. 45, pp. 13244-13249, June 1992.
- [16] B. Hammer, L. B. Hansen, and J. K. Norskov, "Improved adsorption energetics within density-functional theory using revised Perdew-Burke-Ernzerhof functionals", *Phys. Rev. B*, vol. 59, pp. 7413-7421, Mar. 1999.

- [17] C. Lee, W. Yang, and R. G. Parr, "Development of the Colle-Salvetti correlationenergy formula into a functional of the electron density", *Phys. Rev. B*, vol. 37, pp. 785-789, Jan. 1988.
- [18] M. Dion, H. Rydberg, E. Schrder, D. C. Langreth, and B. I. Lundqvist, "Van der Waals Density Functional for General Geometries", *Physical Review Letters*, vol. 92, pp. 22-25, June 2004.
- [19] R. P. Feynman, "Forces in Molecules", *Phys. Rev.*, vol. 56, pp. 340-343, Aug. 1939.
- [20] J. Thijssen, "Computational Physics", Cambridge University Press, 2007.
- [21] D. M. Ceperley and B. J. Alder, "Exchange-correlation potential and energy for density-functional calculation", *Phys. Rev. Lett*, vol. 45, pp. 567-581, 1980.
- [22] J. P. Perdew and A. Zunger, "Self-interaction correction to density-functional approximations for many-electron systems", *Phys. Rev. B*, vol. 23, pp. 5048-5079, May 1981.
- [23] J. M. Soler, E. Artacho, J. D. Gale, A. Garca, J. Junquera, P. Ordejn, and D. Snchez-Portal, "The SIESTA method for ab initio order- N materials simulation", *Journal of Physics: Condensed Matter*, vol. 14, no. 11, p. 2745, 2002.
- [24] H. Hellmann, "A new approximation method in the problem of many electrons", *The Journal of Chemical Physics* 3.1: 61-61. 1935.
- [25] N. W. Ashcroft, "Electron-ion pseudopotentials in metals", *Physics Letters*, vol. 23, pp. 48-50, Oct. 1966.
- [26] I. V. Abarenkov and V. Heine, "No Title", *Phil. Mag.*, vol. XII, p. 529, 1965.
- [27] A. Zunger and M. L. Cohen, "First-principles nonlocal-pseudopotential approach in the density-functional formalism: Development and application to atoms", *Phys. Rev. B*, vol. 18, pp. 5449-5472, Nov. 1978.

- [28] D. R. Hamann, M. Schlter, and C. Chiang, "Norm-Conserving Pseudopotentials", *Phys. Rev. Lett.*, vol. 43, pp. 1494-1497, Nov. 1979.
- [29] N. Troullier and J. Martins, "A straightforward method for generating soft transferable pseudopotentials", *Solid State Communications*, vol. 74, pp. 613-616, May 1990.
- [30] N. Troullier and J. L. Martins, "Effient pseudopotentials for plane-wave calculations", *Phys. Rev. B*, vol. 43, pp. 1993-2006, Jan. 1991.
- [31] O. F. Sankey and D. J. Niklewski, "ntextitAb initio multicenter tight-binding model for molecular-dynamics simulations and other applications in covalent systems", *Phys. Rev. B*, vol. 40, pp. 3979-3995, Aug. 1989.
- [32] J. Slyom, "Fundamentals of the Physics of Solids: Volume 3 - Normal, Broken-Symmetry, and Correlated Systems. Theoretical Solid State Physics: Interaction Among Electrons", Springer, 2010.
- [33] W. H. Press, "Numerical Recipes 3rd Edition: The Art of Scientific Computing", Cambridge University Press, 2007.
- [34] G. P. Astrakhantsev, "An iterative method of solving elliptic net problems", *USSR Computational Mathematics and Mathematical Physics*, vol. 11, no. 2, pp. 171-182, 1971.
- [35] J. W. Cooley and J. W. Tukey, "An algorithm for the machine calculation of complex Fourier series", *Mathematics of computation*, vol. 19, no. 90, pp. 297-301, 1965.
- [36] N. R. Kestner. "He-He Interaction in the SCF-MO Approximation", *J. Chem. Phys.*, Vol. 48, N. 1, pp. 252-257, 1968.
- [37] H. B. Jansen, P. Ros, "Non-empirical molecular orbital calculations on the protonation of carbon monoxide", *Chem. Phys. Lett.* Vol. 3, N. 3, pp. 140-143, 1969.

- [38] B. Liu, A. D. Malean, "Accurate calculation of the attractive interaction of two ground state helium atoms", *J. Chem. Phys.*, Vol. 59, N. 8, pp. 4557-4558, 1973.
- [39] F. Jensen, "The Magnitude of Intramolecular Basis Set Superposition Error", *Chem. Phys. Lett.* Vol. 261, N. 6, pp. 633 - 636, 1996.
- [40] M. L. Senent, S. Wilson, "Intramolecular basis set superposition errors" *International Journal of Quantum Chemistry*, Vol. 82, N. 6, pp. 282-292, 2001.
- [41] S. F. Boys, F. Bernardi, "The calculations of small molecular interaction by the difference of separate total energies - some procedures with reduced error - *Molecular Physics*", Vol. 19, pp. 553-566, 1970.
- [42] P. Valiron, I. Mayer, "Hierarchy of counterpoise corrections for N-body clusters: generalization of the Boys-Bernardi scheme", *Chem. Phys. Lett.*, Vol. 275, N. 1, pp. 46-55, 1997.

Chapter 3

Green's functions method

The previous chapter introduced the DFT method for the calculation of the electronic structure of an isolated molecule. The next step is to connect this isolated molecule to semi-infinite leads and compute the probability of transmission through the system. This is carried out by using the Green's function scattering formalism.

In this chapter I will first introduce the simplest form of a retarded Green's function for a one dimensional tight binding chain, and show how it is similar to the wavefunction of a system. I will then show how the Green's function is directly related to the transmission coefficient across a scattering region by presenting a simple example of a one dimensional lattice where the periodicity is broken at a single connection. The methods used in solving this simple example will then be used in deriving the transmission coefficient of a general scattering region connected to two general, semi-infinite periodic electrodes.

3.1 Green's function of an infinite 1D chain

The first step in solving this problem is to calculate Green's function of an infinite one dimensional tight binding chain as shown in Figure 3.1. The Schrodinger equation for that system is

$$\hat{H}|\Psi\rangle = E|\Psi\rangle \quad (3.1)$$

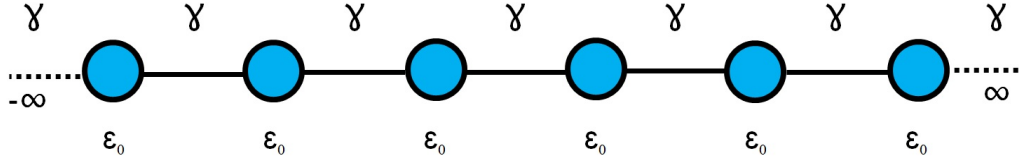


Figure 3.1: Tight-binding approximation of a one-dimensional periodic lattice with on-site energies ε_o and hopping parameters γ

where \hat{H} is the Hamiltonian and $|\Psi\rangle$ the wavefunction which is expanded in an appropriate one dimensional orthogonal localized basis set

$$|\Psi\rangle = \sum_{z' \in \mathbb{Z}} \psi_{z'} |z'\rangle \quad (3.2)$$

where $|z'\rangle$ denotes the basis of the site z' . Substituting this back into (3.1) and multiplying the equation with $|z\rangle$ gives

$$\sum_{z'} \mathcal{H}_{z,z'} \psi_{z'} = E \psi_z \quad (3.3)$$

Here

$$\mathcal{H}_{z,z'} = \langle z | \hat{H} | z' \rangle \quad (3.4)$$

the form of the Hamiltonian matrix is

$$\mathcal{H} = \begin{pmatrix} \ddots & \gamma & & & & & \\ \gamma & \varepsilon_o & \gamma & & & & \\ & \gamma & \varepsilon_o & \gamma & & & \\ & & \gamma & \varepsilon_o & \gamma & & \\ & & & \gamma & \varepsilon_o & \gamma & \\ & & & & \gamma & \varepsilon_o & \gamma \\ & & & & & \gamma & \ddots \end{pmatrix} \quad (3.5)$$

where γ and ε_o are real numbers, and represent the hopping parameters and the on-site energies respectively. Considering the periodic structure of the matrix, the following equation for every $z \in \mathbb{Z}$ can be written as

$$\gamma\psi_{z+1} + \varepsilon_o\psi_z + \gamma\psi_{z-1} = E\psi_z \quad (3.6)$$

Using the Bloch-theorem $\psi_{z+n} = e^{ikn}\psi_z$ where $-\pi \leq k < \pi$ and $n \in \mathbb{Z}$, the Schrodinger equation (3.6) can be solved to obtain the following dispersion relation

$$E(k) = \varepsilon_o + 2\gamma\cos(k) \quad (3.7)$$

and the wavefunction for the $z - th$ site

$$\psi_z = \frac{e^{ikz}}{\sqrt{v}} \quad (3.8)$$

which has been normalized by the group velocity

$$\hbar v = \frac{\partial E}{\partial k} = -2\gamma\sin(k) \quad (3.9)$$

It is important to note, that for a given energy there are two wavefunctions that satisfy (3.1) and their k and v have opposite signs. The wavefunction with positive group velocity is called a right moving wave and with negative group velocity it is called a left moving wave. With the choice of $\gamma < 0$ the right moving waves have $k = +|k|$ and the left moving waves have $k = -|k|$. Since only their signs are different, for convenience I restricted k and v to be positive and explicitly add the sign there if I wanted to distinguish between the left and right moving waves. The Green's function of this system is defined by the equation

$$(E - \hat{H})\hat{g} = \hat{I} \quad (3.10)$$

which can be transformed into a matrix equation by using the basis set defined above

$$(E\mathcal{I} - \mathcal{H})g^\infty = \mathcal{I} \quad (3.11)$$

where g^∞ is the matrix form of the Green's function and \mathcal{I} is the identity matrix.

Formally the solution could be written as the inverse of the $E\mathcal{I} - \mathcal{H}$ matrix, however this matrix is infinite. Furthermore, this equation itself is not enough to determine the Green's function, since the system is only described completely by including the boundary conditions as well. The retarded Green's function, the one we need, as it will be clear later, belongs to the boundary condition for outgoing waves. Therefore one has to set the boundary of this open system so that the waves are propagating outwards to infinity, namely at positive infinity we have a propagating wave that goes in the positive direction and at negative infinity a propagating wave that goes in the negative direction.

Substituting the explicit form of the Hamiltonian (3.5) into (3.11) for a given z'

$$-\gamma g_{z-1,z'}^\infty + (E - \varepsilon_o)g_{z,z'}^\infty - \gamma g_{z+1,z'}^\infty = \delta_{z,z'} \quad (3.12)$$

equation (3.12) is a Schrodinger equation, except for $z = z'$. To obey the retarded boundary conditions the following solutions are assumed

$$g_{z,z'}^\infty = \begin{cases} A^- e^{-ik(z-z')} & z < z' \\ A^+ e^{ik(z-z')} & z > z' \end{cases} \quad (3.13)$$

By substituting this ansatz into (3.12) and using the definition of the group velocity the amplitudes are expressed as

$$g_{z,z'}^\infty = A^+ = A^- = \frac{1}{i\hbar v} \quad (3.14)$$

This way the retarded Green's function for the one dimensional chain has the following form

$$g_{z,z'}^\infty = \frac{e^{ik|z-z'|}}{i\hbar v} \quad (3.15)$$

3.2 Green's function of a semi-infinite 1D chain

Figure 3.2 shows the Green's function of a semi-infinite lead. Our aim is to attach the leads to the scatterer, so we are going to show the Green's function of a semi-infinite lead.



Figure 3.2: One dimensional semi-infinite tight-binding chain with ϵ_o on-site energies and γ hopping parameters, left: for the left lead, right: for the right lead.

The equations for the Green's function of the left semi-infinite lead are the same as for the infinite lead, but with $z, z' \leq 0$, with the terminating point $z = 0$

$$\gamma g_{-1,z'}^L + (E - \epsilon_o) g_{0,z'}^L = \delta_{z',0} \quad (3.16)$$

This is the same as (3.12) with the condition that $g_{1,z'}^L = 0$, hence the problem is the same as in the infinite case, but with an additional boundary condition. With adding a left going wave to (3.15) this condition can be satisfied

$$g_{z,z'}^L = g_{z,z'}^\infty + B e^{-ikz} \quad (3.17)$$

furthermore $g_{z,z'}^L$ is only sensible if $z, z' \leq 0$ and B can be determined from the $g_{1,z'}^L = 0$ condition. Since a left going wave was added, this Green's function is still a retarded Green's function. Finally it takes the form

$$g_{z,z'}^L = \frac{e^{ik|z-z'|} - e^{ik(2-z'-z)}}{i\hbar v} \quad (3.18)$$

Similarly one can derive the Green's function of the right semi-infinite lead, which is

the calculations to 2×2 matrices using

$$V_a = \begin{pmatrix} 0 & \alpha \\ \alpha & 0 \end{pmatrix} \tag{3.28}$$

which is the (2×2) nonzero submatrix of the coupling matrix, and defining

$$\begin{aligned} g_a &= \begin{pmatrix} g_{00}^{L\infty} & 0 \\ 0 & g_{11}^{R\infty} \end{pmatrix} \\ &= \begin{pmatrix} g_l & 0 \\ 0 & g_r \end{pmatrix} \end{aligned} \tag{3.29}$$

This way the (2×2) submatrix of the full Green's function is

$$G_a = g_a + G_a V_a g_a \tag{3.30}$$

Rearranging this obtains

$$G_a = [(g_a)^{-1} - V_a]^{-1} \tag{3.31}$$

which is

$$\begin{aligned} &= \begin{pmatrix} G_{a,00} & G_{a,01} \\ G_{a,10} & G_{a,11} \end{pmatrix} \\ &= \begin{pmatrix} g_l^{-1} & -\alpha \\ -\alpha & g_r^{-1} \end{pmatrix}^{-1} \\ &= \frac{1}{g_l^{-1} g_r^{-1} - \alpha^2} \begin{pmatrix} g_r^{-1} & \alpha \\ \alpha & g_l^{-1} \end{pmatrix} \end{aligned} \tag{3.32}$$

One could also express the other elements of \mathcal{G}_a , but as we will see later, knowing this block is sufficient for the transport calculations.

(3.34)

$$V_b = \begin{pmatrix} 0 & \alpha & 0 \\ \alpha & 0 & \beta \\ 0 & \beta & 0 \end{pmatrix}$$

(3.35)

and finally the important subpart of the Green's function takes the form

$$G_b = \begin{pmatrix} g_l^{-1} & -\alpha & 0 \\ -\alpha & E - \varepsilon_1 & -\beta \\ 0 & -\beta & g_r^{-1} \end{pmatrix}^{-1}$$

(3.36)

3.5 Green's function of a general scatterer between semi-infinite 1D chains

Following the same logic one can express the Green's function for a general scatterer between semi-infinite 1D chains. The corresponding tight-binding model is depicted on Figure 3.5 The Hamiltonian matrix now has the following block

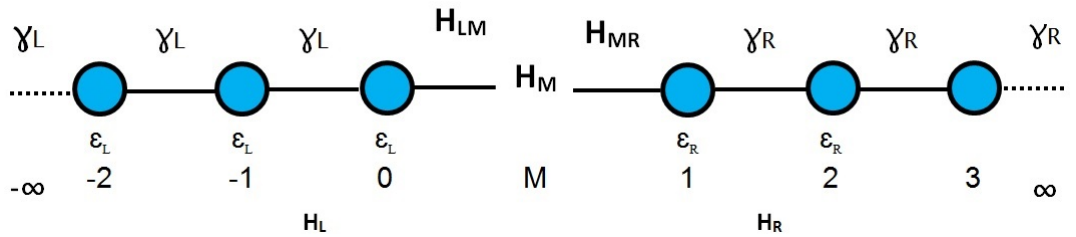


Figure 3.5: Tight-binding chains with a general scatterer

matrix form

$$H = \begin{pmatrix} \mathcal{H}_l & \mathcal{H}_{LM} & 0 \\ \mathcal{H}_{LM}^\dagger & \mathcal{H}_M & \mathcal{H}_{MR} \\ 0 & \mathcal{H}_{MR}^\dagger & \mathcal{H}_R \end{pmatrix}$$

(3.37)

where \mathcal{H}_M is an N by N matrix, \mathcal{H}_{LM} is an $\infty \times N$ and \mathcal{H}_{MR} is an $N \times \infty$ matrix, and N denotes the number of sites in the scatterer. In principle H_{LM} and H_{MR} are infinite, but they only have a $1 \times N$ and $N \times 1$ block that is defined to be nonzero, which will be denoted by H_{LM} and H_{MR} . The Green's function of the decoupled system the system (with $H_{LM} = H_{MR} = 0$) can be written as $g^\infty = g^{L\infty} \oplus g_M \oplus g^{R\infty}$, where $g_M = (EI - H_M)^{-1}$. As previously, it is possible to construct the truncated matrices.

$$g = \begin{pmatrix} g_l & 0 & 0 \\ 0 & g_M & 0 \\ 0 & 0 & g_r \end{pmatrix} \quad (3.38)$$

$$V = \begin{pmatrix} 0 & H_{LM} & 0 \\ H_{LM}^\dagger & 0 & H_{MR} \\ 0 & H_{MR}^\dagger & 0 \end{pmatrix} \quad (3.39)$$

Now the (3×3) superscript denotes the 3 blocks inside. Substituting the blocks (3.38) and (3.39) into Dyson's equation yields the truncated Green's function

$$G = \begin{pmatrix} G_{LL} & G_{LM} & G_{LR} \\ G_{ML} & G_{MM} & G_{MR} \\ G_{RL} & G_{MR} & G_{RR} \end{pmatrix} = \begin{pmatrix} g_l^{-1} & -H_{LM} & 0 \\ -H_{LM}^\dagger & EI - H_M & -H_{MR} \\ 0 & -H_{MR}^\dagger & g_r^\dagger \end{pmatrix}^{-1} \quad (3.40)$$

where the matrix elements are themselves matrices with the corresponding dimension.

3.6 Green's function of a general system

3.6.1 Green's function of an infinite periodic system

Previously, the Green's function of a one-dimension chain was calculated. At this point, I extended this to examine a general procedure to produce the Green's function of an arbitrary periodic system. So, assuming we have a periodic infinite lead in the z direction, and consisting of both slices of intra-Hamiltonians, H_0 and inter-Hamiltonian elements, H_1 , as shown on Figure 3.6.

The Hamiltonian describing this lead is

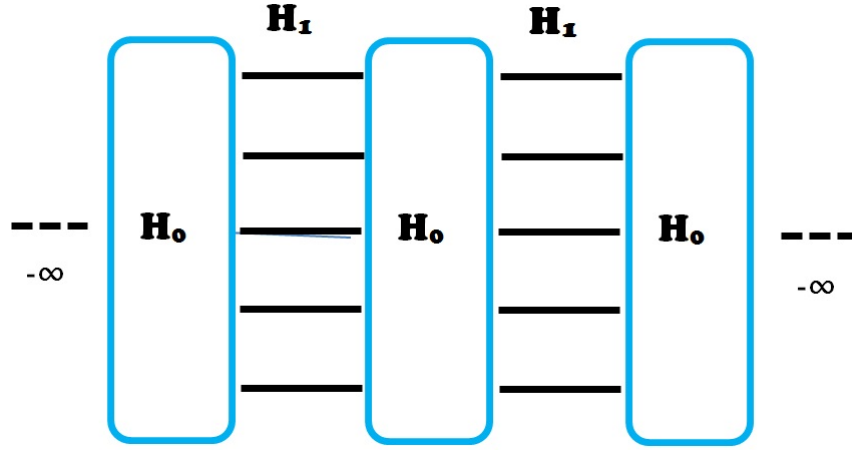


Figure 3.6: A general infinite periodic lead

$$\mathcal{H} = \begin{pmatrix} \ddots & H_1 & & & & \\ H_1^\dagger & H_0 & H_1 & & & \\ & H_1^\dagger & H_0 & H_1 & & \\ & & H_1^\dagger & H_0 & H_1 & \\ & & & H_1^\dagger & H_0 & H_1 \\ & & & & H_1^\dagger & \ddots \end{pmatrix}$$

(3.41)

Therefore, at a point z along the periodic direction, the Schrodinger equation can be written in terms of the energy E and the wavefunction $|\psi_z\rangle$, the same as in the

case of the 1D chain.

$$H_o|\psi_z\rangle + H_1|\psi_{z+1}\rangle + H_1^\dagger|\psi_{z-1}\rangle = E|\psi_z\rangle \quad (3.42)$$

The system considered is infinitely periodic in the z direction only and is finite in both x and y directions. This means, that any unit cell z , the wavefunction $|\psi_z\rangle$ can be represented in Bloch form

$$|\psi_z\rangle = \frac{1}{\sqrt{V_k}} e^{ikz} |\phi_k\rangle \quad (3.43)$$

consisting of a product of a propagating plane wave, and a wavefunction $|\phi_k\rangle$ in the perpendicular direction to transport. The latter has M degrees of freedom and is therefore a $1 \times M$ dimensional vector. This can be substituted back into (3.42), where the dependence on the position z drops out, leaving a set of modified Schrodinger equations

$$(H_o + H_1\chi + H_1^\dagger\chi^{-1})|\phi_k\rangle = E|\phi_k\rangle \quad (3.44)$$

where $\chi = e^{ik}$.

In normal band structure calculations, the Hamiltonian on the left hand side of (3.44) is diagonalized for a given k value to find the M energy eigenvalues $E_i(k)$ ($i = 1 \dots M$) and the corresponding set of eigenvectors $|\phi_k\rangle$. The method employed here was the opposite, for a given energy value E , all complex values of k will be obtained by finding the allowed values of χ . This can be done by rearranging (3.44) into the form

$$[-H_1^{-1}(H_o - E) - H_1^{-1} - H_1^\dagger\chi^{-1}]|\phi_k\rangle = \chi|\phi_k\rangle \quad (3.45)$$

where χ now represents the eigenvalues of the new matrix. Defining $|\omega_k\rangle = \chi^{-1}|\phi_k\rangle$ and substituting this into equation (3.45), an equivalent eigenvalue equation is

formed

$$\begin{pmatrix} -H_1^{-1}(H_o - E) & -H_1^{-1}H_1^\dagger \\ \mathcal{I} & 0 \end{pmatrix} \begin{pmatrix} |\phi_k\rangle \\ |\omega_k\rangle \end{pmatrix} = \chi \begin{pmatrix} |\phi_k\rangle \\ |\omega_k\rangle \end{pmatrix} \quad (3.46)$$

which can be solved numerically. Once this is solved, it gives a set of $2M$ eigenvalues, and the wavefunctions $|\phi_k\rangle$ can be identified as the top M components of each eigenvector.

If H_o is Hermitian, then these eigenvalues can be divided into two sets: those which are propagating or decaying right as $z \rightarrow \infty$, and those which are propagating or decaying left as $z \rightarrow -\infty$. Left/right propagating states correspond to real values of k , whereas states decaying as $z \rightarrow \pm\infty$ correspond to complex values of k . If k is real, there exist pairs of solutions corresponding to right k and left \bar{k} propagating states, which either have positive v^+ or negative v^- group velocities, respectively. These real k -vectors identify open scattering channels, and in this case, $k = -\bar{k}$. The channel velocities are given by

$$\nu^+ = \frac{1}{\hbar} \frac{\partial E(k)}{\partial k} > 0 \quad (3.47)$$

$$\nu^- = \frac{1}{\hbar} \frac{\partial E(\bar{k})}{\partial \bar{k}} < 0 \quad (3.48)$$

Imaginary solutions of k can again be paired and if k is a solution, then k^* is also a solution. A summary on the sorting of the states can be found in Table 3.1.

	Left	Right
Decaying	$\text{Im } k_1 > 0$	$\text{Im } k_1 < 0$
Propagating	$\text{Im } k_1 = 0, \nu_{kl} < 0$	$\text{Im } k_1 = 0, \nu_{kl} > 0$

Table 3-1: Sorting the eigenstates into left and right propagating or decaying states.

It is now possible to construct the Green's function for this general infinitely

periodic system. As we demonstrated before, the Green's function is related to the wavefunction of the system, and in this case will take the form

$$\mathcal{G}_{z,z'} = \begin{cases} \sum_{l=1}^M |\phi_{k_l}\rangle e^{ikl(z-z')} \langle W_{kl}| & z \geq z' \\ \sum_{l=1}^M |\phi_{\bar{k}_l}\rangle e^{i\bar{k}l(z-z')} \langle W_{\bar{k}l}| & z \leq z' \end{cases} \quad (3.49)$$

where the vectors $\langle W_{kl}|$ and $\langle W_{\bar{k}l}|$ and have to be determined. For an infinitely periodic system the Green's function should be continuous at the point $z = z'$, which produces the continuity condition

$$\sum_{l=1}^M |\phi_{k_l}\rangle \langle W_{kl}| = \sum_{m=1}^M |\phi_{\bar{k}_m}\rangle \langle W_{\bar{k}m}| \quad (3.50)$$

Equation (3.49) can be substituted back into the defining equation for the Green's function

$$(E\mathcal{I} - \mathcal{H})\mathcal{G} = \mathcal{I} \quad (3.51)$$

Obtaining

$$(E - H_o)\mathcal{G}_{z,z} + H_1\mathcal{G}_{z,z+1} + H_1^\dagger\mathcal{G}_{z,z-1} = 1 \quad (3.52)$$

which can be expanded at a point z and simplified considerably if only the nearest slice interactions are included

$$\sum_{l=1}^M [(E - H_o)|\phi_{k_l}\rangle \langle W_{k_l}| + H_1|\phi_{k_l}\rangle e^{ikl} \langle W_{k_l}| + H_1^\dagger|\phi_{\bar{k}_l}\rangle e^{i\bar{k}l} \langle W_{\bar{k}_l}|] = 1 \quad (3.53)$$

After some manipulation and the use of the Schrodinger equation from (3.44), it was possible to reduce (3.53) further to

$$\sum_{l=1}^M H_1^\dagger [|\phi_{k_l}\rangle e^{-ikl}\langle W_{k_l}| - |\phi_{\bar{k}_l}\rangle e^{-i\bar{k}l}\langle W_{\bar{k}_l}|] = -1 \quad (3.54)$$

Before proceeding, it is important to note that in normal band structure calculations the wavefunctions corresponding to a given choice of k are all orthogonal. However, wavefunctions corresponding to different choices of k are not necessarily orthogonal, because the operator on the left side of (3.44) does not necessarily commute with itself for different choices of χ . Hence the solutions of (3.46) for a fixed energy and different k need not be orthogonal. In this case a dual basis can be defined $|\bar{\phi}_{k_l}\rangle$ which is orthonormal to the basis $|\phi_{k_l}\rangle$ and these two together form a complete basis in the Hilbert space

$$\langle \phi_{\bar{k}l} | \bar{\phi}_{\bar{k}m} \rangle = \delta_{\bar{k}l\bar{k}m} \quad (3.55)$$

$$\langle \phi_{kl} | \bar{\phi}_{km} \rangle = \delta_{klkm} \quad (3.56)$$

$$\sum_{l=1}^M |\phi_{\bar{k}l}\rangle \langle \bar{\phi}_{\bar{k}l}| = I \quad (3.57)$$

$$\sum_{l=1}^M |\phi_{kl}\rangle \langle \bar{\phi}_{kl}| = I \quad (3.58)$$

By defining this dual basis it is now possible to express $\langle W_{k_l}|$ as a superposition of $\langle W_{\bar{k}_l}|$, and vice versa by manipulating equation (3.50)

$$\langle W_{k_l}| = \sum_{l=1}^M \langle \bar{\phi}_{kl} | \phi_{\bar{k}m} \rangle \langle W_{\bar{k}_m}| \quad (3.59)$$

$$\langle W_{\bar{k}_l}| = \sum_{l=1}^M \langle \bar{\phi}_{\bar{k}l} | \phi_{km} \rangle \langle W_{k_m}| \quad (3.60)$$

(3.60) can be substituted into equation (3.54) and simplified to produce the two equations

$$\langle W_{k_l} | = \sum_{m=1}^M \langle \bar{\phi}_{km} | \mathcal{V}^{-1} \quad (3.61)$$

$$\langle W_{\bar{k}_l} | = \sum_{m=1}^M \langle \bar{\phi}_{\bar{k}m} | \mathcal{V}^{-1} \quad (3.62)$$

which show the vectors $\langle W_{k_l} |$ and $\langle W_{\bar{k}_l} |$ in terms of the basis and dual basis functions with

$$\mathcal{V}^{-1} = \sum_{l=1}^M H_1^{-1} (|\phi_{kl}\rangle e^{-ik_l} \langle \bar{\phi}_{kl} | - |\phi_{\bar{k}l}\rangle e^{-i\bar{k}_l} \langle \bar{\phi}_{\bar{k}l} |) \quad (3.63)$$

The Green's function for the infinite periodic system can now be written by substituting the $|W\rangle$ vectors back into equation (3.49)

$$\mathcal{G}_{z,z'} = \begin{cases} \sum_{l=1}^M |\phi_{kl}\rangle e^{ik_l(z-z')} \langle \bar{\phi}_{kl} | \mathcal{V}^{-1} & z \geq z' \\ \sum_{l=1}^M |\phi_{\bar{k}_l}\rangle e^{i\bar{k}_l(z-z')} \langle \bar{\phi}_{\bar{k}l} | \mathcal{V}^{-1} & z \leq z' \end{cases} \quad (3.64)$$

3.6.2 Green's function of a semi-infinite periodic system

In this section I am going to construct the Green's functions for the left and right semi-infinite periodic systems. This is carried out in a similar fashion to that of the one-dimensional example, where the semi-infinite Green's function was derived directly from the infinite system's Green's function.

The left lead is defined by the periodic system extending from $z = -\infty$ to the last Hamiltonian slice at $z = z_o - 1$, and the right lead is defined by the periodic system extending from $z = \infty$ to its last Hamiltonian slice at $z = z_o + 1$. From these boundary conditions, the left and right lead Green's functions (\mathcal{G}^L , \mathcal{G}^R) are constrained to be zero at the point $z = z_o$

$$\mathcal{G}_{z_o,z'}^L = \mathcal{G}_{z_o,z'}^R = 0 \quad (3.65)$$

To obey these constraints as in the one dimensional example a wavefunction can be added to the infinite system's Green's function (3.64). First we will add a left moving wavefunction with amplitude $\Lambda_l(z', z_o)$ to the left lead side

$$\mathcal{G}_{z,z'}^L = \mathcal{G}_{z,z'} + \sum_{l=1}^M |\phi_{\bar{k}_l}\rangle e^{i\bar{k}_l z} \Lambda_l(z', z_o) \quad (3.66)$$

The amplitude $\Lambda_l(z', z_o)$ is found by applying the constraint (3.65) at the point $z = z_o$

$$\sum_{l=1}^M |\phi_{k_l}\rangle e^{ik_l(z_o - z')} \langle \bar{\phi}_{k_l} | \nu^{-1} + \sum_{l=1}^M |\phi_{\bar{k}_l}\rangle e^{i\bar{k}_l z_o} \Lambda_l = 0 \quad (3.67)$$

Therefore

$$\Lambda_l = - \sum_{m=1}^M e^{-i\bar{k}_l z_o} \langle \bar{\phi}_{\bar{k}_m} | \phi_{k_l}\rangle e^{ik_l(z_o - z')} \langle \phi_{\bar{k}_l} | \mathcal{V}^{-1} \quad (3.68)$$

Substituting this into equation (3.66) produces the Green's function of the left semi infinite lead

$$\mathcal{G}_{z,z'}^L = \left[\sum_{l=1}^M |\phi_{k_l}\rangle e^{ik_l(z - z')} \langle \bar{\phi}_{k_l} | - \sum_{l,m=1}^M |\phi_{\bar{k}_l}\rangle e^{i\bar{k}_l(z - z_o)} \langle \bar{\phi}_{\bar{k}_m} | \phi_{k_l}\rangle e^{ik_l(z_o - z')} \langle \bar{\phi}_{k_l} | \right] \mathcal{V}^{-1} \quad (3.69)$$

This can be repeated in exactly the same manner for the right lead, by adding a right moving wavefunction. This leads to the Green's function of the right semi infinite lead

$$\mathcal{G}_{z,z'}^R = \left[\sum_{l=1}^M |\phi_{\bar{k}_l}\rangle e^{i\bar{k}_l(z - z')} \langle \bar{\phi}_{\bar{k}_l} | - \sum_{l,m=1}^M |\phi_{k_l}\rangle e^{ik_l(z - z_o)} \langle \bar{\phi}_{\bar{k}_m} | \phi_{\bar{k}_l}\rangle e^{i\bar{k}_l(z_o - z')} \langle \bar{\phi}_{\bar{k}_l} | \right] \mathcal{V}^{-1} \quad (3.70)$$

The final step in this analysis is to extract the surface Green's function evaluated at each end point $z = z' = z_o$ for the left and right leads. This can be simplified using the completeness relations (3.55) (3.56) (3.57) (3.58) and yields

$$G^L = \mathcal{G}_{z_o, z_o}^L = [I - \sum_{l,m=1}^M |\phi_{\bar{k}_m}\rangle e^{-i\bar{k}_m} \langle \bar{\phi}_{\bar{k}_m} | \phi_{k_l}\rangle e^{ik_l} \langle \bar{\phi}_{k_l} |] \mathcal{V}^{-1} \quad (3.71)$$

$$G^R = \mathcal{G}_{z_o, z_o}^R = [I - \sum_{l,m=1}^M |\phi_{k_m}\rangle e^{ik_m} \langle \bar{\phi}_{k_m} | \phi_{\bar{k}_l}\rangle e^{-i\bar{k}_l} \langle \bar{\phi}_{\bar{k}_l} |] \mathcal{V}^{-1} \quad (3.72)$$

3.6.3 Including a scattering region

As before, the first step was to set the couplings H_{LM} and H_{MR} to zero, thus the truncated Green's function g^{tr} across the uncoupled device is

$$g^{tr} = \begin{pmatrix} G^L & 0 & 0 \\ 0 & (EI - H_M)^{-1} & 0 \\ 0 & 0 & G^R \end{pmatrix} \quad (3.73)$$

Here, the Green's function of the isolated scatterer is calculated directly from the equation $(EI - H_M)G_M = I$. Turning on the couplings to the scattering region is again done by introducing the truncated perturbation Γ^{tr}

$$\Gamma^{tr} = \begin{pmatrix} 0 & H_{LM} & 0 \\ H_{LM}^\dagger & 0 & H_{MR} \\ 0 & H_{MR}^\dagger & 0 \end{pmatrix} \quad (3.74)$$

Using equations (3.73) and (3.74) in Dyson's equation yields the truncated block G^{tr} of the full retarded Green's function of the system

$$G^{tr} = (g^{-1} - \Gamma^{tr})^{-1} = \begin{pmatrix} G^L & G_{LM} & G_{LR} \\ G_{ML} & G_M & G_{MR} \\ G_{RL} & G_{RM} & G^R \end{pmatrix} \quad (3.75)$$

3.7 Obtaining the transmission coefficients

From equation (3.75) one can see, that if we want to calculate any part of G^{tr} we need to invert a matrix the size of the lead's surfaces plus the size of the scatterer (due to Dyson's equation). This is computationally very intense, and as the Fisher-Lee formula [1] expresses the transmission and reflection coefficients as a function of the surface Green's functions only, the Green's functions between two internal points in the scatterer are not needed.

To overcome this, it is possible to substitute the full Hamiltonian of the system by an effective Hamiltonian, that couples the surface sites directly. Let us consider the Schrodinger equation

$$\sum_j H_{ij}\Psi_j = E\Psi_i \quad (3.76)$$

Separating the l - th degree of freedom from (3.76) obtains

$$H_{il}\Psi_l + \sum_{j \neq l} H_{ij}\Psi_j = E\Psi_i \quad (i \neq l) \quad (3.77)$$

$$H_{ll}\Psi_l + \sum_{j \neq l} H_{lj}\Psi_j = E\Psi_l \quad (i = l) \quad (3.78)$$

(3.78) and Ψ_l is

$$\Psi_l = \sum_{j \neq l} \frac{H_{lj}\Psi_j}{E - H_{ll}} \quad (3.79)$$

Inserting (3.79) into (3.76) results in the following effective Schrodinger equation

$$\sum_{j \neq l} [H_{ij}\Psi_j + \frac{H_{il}H_{lj}\Psi_j}{E - H_{ll}}] = E\Psi_i \quad (i \neq l) \quad (3.80)$$

where the number of degrees of freedom is decreased by one compared to (3.76).

We can hence introduce a new effective Hamiltonian H^{eff} as

$$H_{ij}^{eff} = H_{ij} + \frac{H_{il}H_{lj}}{E - H_{ll}} \quad (3.81)$$

In this way we are able to use Gauss elimination to remove any unwanted degrees of freedom from the Hamiltonian (it is also called decimation). Now the original scattering problem with the Hamiltonian \mathcal{H} can be reduced into this effective Hamiltonian

$$\mathcal{H}^{eff} = \begin{pmatrix} \mathcal{H}_L & \mathcal{V}_c \\ \mathcal{V}_c^\dagger & \mathcal{H}_R \end{pmatrix} \quad (3.82)$$

where \mathcal{V}_c is the new effective coupling Hamiltonian. Using Dyson's equation again, for the truncated Green's function we get

$$\begin{aligned} G_{eff}^{tr} &= \begin{pmatrix} (G^L)^{-1} & V_c \\ V_c^\dagger & (G^R)^{-1} \end{pmatrix} \\ &= \begin{pmatrix} G_{00} & G_{01} \\ G_{10} & G_{11} \end{pmatrix} \end{aligned} \quad (3.83)$$

And finally the generalization of the Fisher-Lee relation [1, 2] assuming that the states are normalized to carry unit flux- gives the matrix elements for the transmission amplitude \hat{t} from the left lead to the right lead as

$$t_{hl} = \bar{\phi}_{k_h}^\dagger G_{01} \mathcal{V}_L \phi_{k_l} \sqrt{\left| \frac{\nu_h}{\nu_l} \right|} \quad (3.84)$$

ϕ_{k_h} is a right moving state vector in the right lead, ϕ_{k_l} is a right moving state vector in the left lead, ν_h and ν_l are the corresponding group velocities and \mathcal{V}_L is \mathcal{V} defined by (3.63) for the left lead. The matrix elements of the reflection amplitude in the left lead \hat{r} read

$$r_{hl} = \bar{\phi}_{k_h}^\dagger (G_{00} \mathcal{V}_L - I) \phi_{k_l} \sqrt{\left| \frac{\nu_h}{\nu_l} \right|} \quad (3.85)$$

Similarly for particles coming from the right

$$t'_{hl} = \bar{\phi}_{k_h}^\dagger G_{10} \mathcal{V}_R \phi_{\bar{k}_l} \sqrt{\left| \frac{\nu_h}{\nu_l} \right|} \quad (3.86)$$

$$r'_{hl} = \bar{\phi}_{k_h}^\dagger (G_{11} \nu_R - I) \phi_{\bar{k}_l} \sqrt{\left| \frac{\nu_h}{\nu_l} \right|} \quad (3.87)$$

The scattering matrix, S_C built up from transmission and reflection coefficients in such a manner is unitary. Finally, the total observable transmission coefficient for the system can be found by adding all channels

$$\mathcal{T}(E) = \sum_{lm=1}^M |t_{lm}|^2 = \sum_{lm=1}^M t_{lm}^* t_{lm} = \mathcal{T}r(\hat{t}^\dagger \hat{t}) \quad (3.88)$$

This chapter has demonstrated that by using the Green's function scattering approach a potentially infinitely sized problem can be reduced to a finite problem, that can then be solved numerically. In later chapters this procedure will be demonstrated by implementing the DFT code SIESTA [3] and the transmission coefficient will be calculated using the Gollum code [4].

Bibliography

- [1] D. S. Fisher and P. A. Lee, "Relation between conductivity and transmission matrix", *Physical Review B*, vol. 23, no. 12, pp. 6851-6854, 1981.
- [2] S. Sanvito, C. J. Lambert, J. H. Jefferson, and A. M. Bratkovsky, "General Green's function formalism for transport calculations with spd-Hamiltonians and giant magnetoresistance in Co and Ni based magnetic multilayers", no. ii, pp. 1-39, 2008.
- [3] J. M. Soler, E. Artacho, J. D. Gale, A. Garcia, J. Junquera, P. Ordejón, and D. Sánchez-Portall, "The SIESTA method for ab initio order-N materials simulation", *J. Phys.: Condens. Matter* 14, 2745, 2002.
- [4] J. Ferrer, C. J. Lambert, V. M. García-Suárez, D. Z. Manrique, D. Visontai, L. Oroszlány and L. A. Algharagholy, "GOLLUM: a next-generation simulation tool for electron, thermal and spin transport", *New J. Phys.*, 16, 093029, 2014.

Chapter 4

Theory of Quantum Transport

Chapter 3 introduced Green's function scattering formalism for different systems. In this chapter, I will describe electron transport and the transmission coefficient $\mathcal{T}(E)$. Thermoelectric coefficients such as thermopower S , the Peltier coefficient Π , thermal conductance κ and figure of merit ZT are all introduced in this chapter before being used in Chapters 5, 6 and 7.

4.1 Single electron transport

A mixture of scattering theory and a Green's function techniques will be used in this thesis to describe the electric transport and thermoelectric properties of nanoscale organic molecule systems trapped between two gold electrodes.

As was mentioned in the previous chapter on DFT, our approach is subject to the Born-Oppenheimer approximation, that describes the electron system only. The problem which has to be solved is still a complicated many electron problem of a system in nonequilibrium. This kind of problem is difficult and cannot be solved in general, because we have to describe the electron transport by time-dependent many-body wavefunctions of the whole system.

To avoid this kind of hurdle, we are going to use the single electron picture of electron transport, similar to the replacement of the many particle problem in the density functional theory chapter by a single-particle Kohn-Sham formalism.

This means treating the electronic transport as that due to many independent single-electrons. Moreover, we will assume that the single-particle states in the Kohn-Sham formalism actually describe these independent single-electrons.

In the same way, in analogy to standard band structure calculations of solids in equilibrium -in which in many cases the Kohn-Sham single particle eigenvalues and eigenstates can be successfully interpreted as the elementary excitation of the systems. We will use the same procedure in the electronic transport and assume that the effects of the atomic arrangement, of the electronic (self-consistent) charge density and single-particle potential on the current can actually be modeled by this approach. Clearly this is a simplification by introducing a number of approximations, which in some cases makes the results only applicable to main trends in quantum transport. However in many cases these are enough to sufficiently explain the underlying phenomena, while in other cases these can be made more accurate using a number of techniques (like using different exchange-correlations functionals in DFT, correcting for self-interaction and image charge effects [1], etc.).

It is worth mentioning, that there are many effects which restrict the validity of the single-electron transport approach. For instance, electron-electron scattering effects of different conducting electrons are not calculated nor are interactions with the lattice beyond the static approximation, i.e. electron phonon scattering, screening and charging effects or many particle interactions in magnetic systems. However, if these processes are sufficiently weak, then the single-particle approximations in terms of the Kohn-Sham states will provide reasonable results. This approach of this description does not include any processes by which the single particle energy of the states carrying the current is changed, therefore only elastic transport can be described, and it corresponds to the limit in which the mean-free path of the electrons is much larger than the system size. In the single particle picture the description in terms of the Kohn-Sham wavefunction will hold only on length scales shorter than this length scale, since these processes not included in

the model will lead to the scattering destroying the phase coherence of the single-electron states involved.

It is important to mention, that there are many cases this description of the electron current in terms of single-particle physics is not accurate due to quantum many-body effects. For instance, the Kondo-effect, in which a two level quantum scatterer, embedded in a metallic environment leads to conductance abnormalities at low temperatures, or correlation effects like Coulomb blockade [2].

4.2 Transmission coefficient

As mentioned in previous chapter, the main property of nanoscale system calculated in this work is the transmission coefficient $\mathcal{T}(E)$. This is the probability for an electron to pass from one lead to the other and it can easily be related to the electronic property such as conductance G and thermal properties such as the thermopower.

To calculate $\mathcal{T}(E)$, and from it the thermoelectric properties we need to set up a systematic picture for the whole system, as shown in Figure 4.1

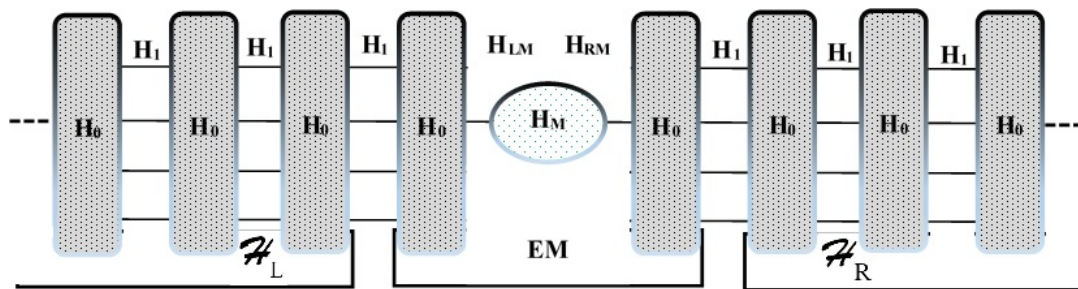


Figure 4.1: A general scattering region (described by H_M) attached to leads, made up from infinite slices of H_0 connected by H_1 . The scattering region, also called the Extended Molecule (EM) already contains part of the leads.

Based on a thermodynamic view, the system is designed with bulk electrodes (reservoirs) in thermal equilibrium with a central region (Molecules). The central region includes a part of the electrodes to form a so-called *extended molecule* (EM), μ_L and μ_R , are chemical potentials for the left and right electrodes and

they are able to exchange electrons with the EM, this situation refers to zero-bias. However, μ_L and μ_R are not equal when a bias is applied, leading to a flow of current. The method for establishing the steady state is to adiabatically switch on the coupling between the electrodes and the EM [3–5]. The probes of current-voltage maintain local charge neutrality, as they are usually made of good metals. Therefore, the effect of an external bias voltage will produce a rigid shift of the whole spectrum, for example, of all the on-site energies, which will lead to a nontrivial potential profile over the EM, that needs to be calculated self-consistently. To avoid the discontinuity of the potential profile (and the generation of spurious scattering) a set of boundary conditions must be applied, so that the resulting self-consistent electrostatic potential matches that of the leads at the boundaries of the EM. Therefore, in order to achieve a good match of the electrostatic potential, several layers of the electrodes are usually included in the EM. Their number ultimately depends upon the screening length of the leads, but in most situations, between two and four-atomic planes are sufficient [6]. It is good practice to include a few layers of the leads in the extended molecule, because the surfaces of the electrodes usually reconstruct, which might undergo additional geometrical changes when bonding to the nanoscale device, e.g. when molecules adsorb to metallic surfaces.

To model the macroscopic sized electrodes in an appropriate way, we are going to use infinitely long leads with infinite cross-sections, with a finite scattering region in between them, but this would result in an infinite Hermitian matrix \mathcal{H} . Here we are assuming, that the electrodes are semi-infinite defect-free crystalline metals, in this case \mathcal{H} will have a regular periodic structure and a unit cell along which the direction of the transport can be defined. It is convenient to introduce the concept of a principal layer (*PL*), which is defined as the smallest cell that repeats periodically in the direction of transport, constructed in a way to interact only with the nearest-neighbor *PL*'s. This means that all the matrix elements between atoms belonging to two nonadjacent *PL*'s vanish, resulting in a rather

sparse \mathcal{H} . For example, in a linear chain of hydrogen atoms described by a nearest-neighbor tight-binding model, one atom forms the unit cell. However, if nearest and next-nearest-neighbor elements are included, then the PL will contain two atoms, etc. This gives us a way to overcome the infinite size of the problem. However, we still have the infinite cross section to deal with, and we have two approximations we can use to overcome this problem. The first option is using leads with a finite cross section. In this case, no periodic boundary conditions in the transverse direction are required and the whole system is quasi one dimensional. However, special care must be taken when choosing the cross section of the electrodes in order to avoid quantum confinement effects. It is also worth noting, that leads with very small cross section make the use of the Landauer formula for transport [7] questionable. As a rule of thumb the linear dimension of the cross section should be several times the Fermi wavelength of the material forming the leads, and there should be several open scattering channels. The second option is to use periodic boundary conditions (PBC). In this case the system is repeated periodically in the transverse direction, meaning that the EM is also repeated periodically. Clearly, quantum confinement effects are eliminated, but one should be particularly careful in order to eliminate the spurious interaction between the mirror images of the EM. Therefore large unit cells must be employed even in this case. However, from a formal point of view the use of periodic boundary conditions does not change the problem setup, but it can only be used with parallel leads.

In (4.1) H_0 is a $N \times N$ matrix describing all interactions within a PL , where N is the total number of degrees of freedom (basis functions) in the PL . Similarly H_1 is the $N \times N$ matrix describing the interaction between two PL 's. In the same way H_M is the $M \times M$ matrix describing the EM and H_{LM} (H_{RM}) is the $N \times M$ ($M \times N$) matrix containing the interaction between the last PL of the left-hand side (right hand side) lead and the EM.

function techniques based on the scattering approach to solve the quantum transport problem.

4.3 Landauer formula and scattering formalism

There is an important and simple way to link or match the theoretical calculations with experimental measurements. The Landauer formula is a key formula for using the electron transmission coefficients obtained from the scattering formalism, to determine experimental quantities such as current or conductance. It is applicable for ballistic mesoscopic or phase coherent systems where the electrons can flow freely between scatterers.

Let us consider the following theoretical quasi one-dimensional transport model (Figure 4.3), a scatterer connected to two perfect and very long leads, which are contacted to two infinite electron reservoirs that have infinitesimally different chemical potentials $\mu_L - \mu_R = \delta E > 0$. This small chemical potential difference will drive the electrons from the left side to the right, through the leads and the scatterer. In fact, the reservoirs set the boundary conditions for the lead-scatterer-lead system: electrons can flow from left to right with energy $\mu = \mu_L \approx \mu_R$.

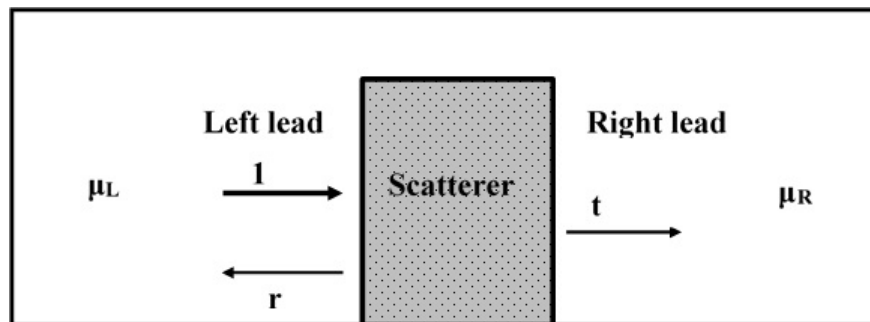


Figure 4.3: Schematics of one dimensional lead-scatterer-lead arrangement and the electron reservoirs with μ_L (left) and μ_R (right) chemical potential.

Let us examine the case when there is only one open channel, i.e. only one propagating wavefunction that satisfies the boundary condition. This means that only one electron can travel through at once (two if one consider the spin). The incident current, i.e., the current that would flow without scattering, and is proportional

to the velocity and the number of electrons within δE energy range, can formally be written as:

$$\delta I = e\nu \frac{\partial n}{\partial E} \delta E$$

where $\frac{\partial n}{\partial E}$ is the density of states and ν the group velocity in the lead at μ energy. Since the system is considered one-dimensional, we can write

$$\frac{\partial n}{\partial E} = \frac{1}{2\pi} \frac{\partial k}{\partial E} = \frac{1}{\nu h}$$

and by this we obtain the simple relation

$$\delta I = \frac{2e}{h} \delta E = \frac{e^2}{h} \delta V$$

δV is the voltage bias that corresponds to the δE chemical potential difference. This relation is remarkable because it tells us that if we measure the conductance of a perfect lead with one open channel then we would get $\frac{e^2}{h}$. Since a channel is either open and conducting, or closed and not conducting, then without scattering there is no lower finite conductivity than $\frac{e^2}{h}$. This conductance quantum corresponds to a resistance of 6.54 k Ω , which is a typical macroscopic resistance in an electric circuit. If we introduce a scatterer, there will be some electrons that will be reflected with probability \mathcal{R} , and some which will be transmitted by a probability \mathcal{T} . The current traveling through the scatterer to the right lead will be

$$\delta I = \frac{e^2}{h} \mathcal{T} \delta V$$

\mathcal{T} is the transmission coefficient of the scatterer (see equation (3.88)), and the conductance is explicitly given by the Landauer formula

$$\frac{\delta I}{\delta V} = G(\mu) = G_0 \mathcal{T}(\mu)$$

where $G_0 = \frac{2e^2}{h} = 7.74809 \times 10^{-5} \text{S}$ is the conductance quantum and $\mathcal{T}(\mu)$ is the transmission coefficient written as a function of the contact chemical potential. The factor 2 in G_0 is introduced to take into account the spin degeneracy, and in the case of multiple channels this can be written as

$$G = \frac{2e^2}{h} \sum \mathcal{T}_n$$

The complete scattering process is described by the \mathcal{S} matrix

$$\mathcal{S} = \begin{pmatrix} r & t' \\ t & r' \end{pmatrix}$$

where t, t' are the transmission amplitude matrices from left to right and right to left, and r, r' are the matrices, which contain the reflection amplitudes in the left and the right lead.

4.4 Thermoelectric coefficients

When there is a temperature difference δT and a potential drop $\Delta V = \Delta\mu/e$ ($e = -|e|$) across one system, this leads to a flow of heat current \dot{Q} and charge I . In linear response, both currents are related to the temperature and potential differences through the thermoelectric coefficients G, L, M and K [9, 10]

$$\begin{pmatrix} I \\ \dot{Q} \end{pmatrix} = \begin{pmatrix} G & L \\ M & K \end{pmatrix} \begin{pmatrix} \Delta V \\ \Delta T \end{pmatrix}$$

where

$$\Delta V = \frac{\mu_L - \mu_R}{e}$$

and

$$\Delta T = T_L - T_R$$

In the absence of a magnetic field L and M , are related by an Onsager relation (T is temperature)

$$M = -LT$$

Rearranging the above equations, gives the current relations in terms of the measurable thermoelectric coefficients: electrical resistance $R = 1/G$, thermopower S , Peltier coefficient Π and the thermal conductance κ can be write

$$\begin{pmatrix} \Delta V \\ \dot{Q} \end{pmatrix} = \begin{pmatrix} 1/G & -L/G \\ M/G & K - LM/G \end{pmatrix} \begin{pmatrix} I \\ \Delta T \end{pmatrix} = \begin{pmatrix} R & S \\ \Pi & \kappa \end{pmatrix} \begin{pmatrix} I \\ \Delta T \end{pmatrix} \quad (4.2)$$

S is defined as the potential drop due to a temperature difference in the absence of an electrical current

$$S \equiv - \left(\frac{\Delta V}{\Delta T} \right)_{I=0} = \frac{L}{G} \quad (4.3)$$

The Peltier coefficient Π can be defined as the heat transferred purely due to the charge current in the absence of a temperature difference

$$\Pi \equiv - \left(\frac{\dot{Q}}{I} \right)_{\Delta T=0} = - \frac{M}{G} = - ST \quad (4.4)$$

the thermal conductance κ is defined as the heat current due to the temperature drop in the absence of an electric current

$$\kappa \equiv \left(\frac{\dot{Q}}{\Delta T} \right)_{I=0} = K \left(1 + \frac{S^2 GT}{K} \right)$$

By looking at the value of S or Π we can have an idea of how well the device will act as a heat driven current generator or a current driven cooling device. Finally we can defined the figure of merit ZT

$$ZT = \frac{S^2 GT}{\kappa} \quad (4.5)$$

According to classical electronics, ZT is derived by finding the maximum induced temperature difference produced by an applied electrical current in the presence of Joule heating. Let's consider a current carrying conductor placed between two heat baths with temperatures T_L and T_R , and electrical potentials V_L and V_R respectively. The thermoelectric figure of merit can be defined by finding the maximum induced temperature difference of the conductor due to an electrical current. Defining \dot{Q} the flux heat from bath L to R , then from equation (4.2)

$$\dot{Q} = \Pi I + \kappa \Delta T$$

The heat transfer makes the left bath cool and the right bath heat, with increasing ΔT . The amount of Joule heating can be expressed as $\dot{Q}_J = RI^2$. which is proportional to the electrical resistance and the square of the current. This Joule heating will also affect the temperature difference induced by the heat transfer, and therefore in the steady state case

$$\Pi I - \kappa \Delta T = \frac{RI^2}{2}$$

By rearranging above formula, ΔT is

$$\Delta T = \frac{1}{\kappa} \left(\Pi I - \frac{RI^2}{2} \right) \quad (4.6)$$

Equation (4.6) shows how ΔT depends on I . To find the maximum temperature difference we differentiate (4.6) with respect to the electric current

$$\frac{\partial \Delta T}{\partial I} = \Pi - IR = 0$$

Finally by writing back $I = \Pi/R$ and substituting eq. (4.4) into eq. (4.6), for the maximum of the temperature difference we obtain

$$(\Delta T)_{max} = \frac{\Pi^2}{2\kappa R} = \frac{S^2 T^2 G}{2\kappa}$$

Therefore

$$\frac{(\Delta T)_{max}}{T} = \frac{S^2 T G}{2\kappa} = \frac{1}{2} ZT$$

The outcome is a dimensionless number that can be used to characterize the "efficiency" of a molecular device.

4.4.1 Generalized formula for the thermoelectric coefficients

In order to calculate all thermoelectric coefficients we need to know \dot{Q} , so we can write a formula for the total heat current on one of the electrodes as the difference of the left- and right-going heat currents on the same electrodes. The heat current on the left electrode is, where the $f_L(E)f_R(E)$ terms cancelled out during the derivation, we obtain

$$\dot{Q}_L = \dot{Q}_L^+ - \dot{Q}_L^- = \frac{2}{h} \int_{-\infty}^{\infty} dE T(E) ((E - \mu_L) f_L(E) - (E - \mu_R) f_R(E))$$

where $\dot{Q}_L^- \dot{Q}_L^+$ is the total heat current moving to the right or left on the left

electrode. To keep it simple we are going to define the general current I^p , which will represent the charge current if $p = 0$ or the heat current if $p = 1$, ($e = -|e|$).

$$I^p = \begin{cases} \frac{I}{e} & p = 0 \\ \dot{Q} & p = 1 \end{cases}$$

The general formula for the current is

$$I^p = \frac{2}{h} \int_{-\infty}^{\infty} dE \mathcal{T}(E) ((E - \mu_L)^p f_L(E) - (E - \mu_R)^p f_R(E)) = \frac{2}{h} \int_{-\infty}^{\infty} dE \mathcal{T}(E) A(E) \quad (4.7)$$

Assuming the below quantities

$$\mu = \frac{\mu_R + \mu_L}{2}$$

and

$$T = \frac{T_R + T_L}{2}$$

rewrite the top and bottom reservoir's Fermi distributions in terms of these with $\Delta\mu = \mu_L - \mu_R$ and $\Delta T = T_L - T_R$, giving

$$\mu_L = \mu + \frac{\Delta\mu}{2}, \quad T_L = T + \frac{\Delta T}{2}$$

$$\mu_R = \mu - \frac{\Delta\mu}{2}, \quad T_R = T - \frac{\Delta T}{2}$$

Thus, the left and right Fermi distributions become

$$f_L(E) = \left(1 + e^{\frac{E - \mu - (\Delta\mu/2)}{k_B(T + (\Delta T/2))}} \right)^{-1}$$

$$f_R(E) = \left(1 + e^{\frac{E - \mu + (\Delta\mu/2)}{k_B(T - (\Delta T/2))}} \right)^{-1}$$

Expanding equation (4.7) in a Taylor series to linear order in ΔV and ΔT yields

$$\begin{aligned} I^p &= I^p|_{\substack{\Delta T=0 \\ \Delta\mu=0}} + \frac{\partial I^p}{\partial \Delta\mu}|_{\substack{\Delta T=0 \\ \Delta\mu=0}} \Delta\mu + \frac{\partial I^p}{\partial \Delta T}|_{\substack{\Delta T=0 \\ \Delta\mu=0}} \Delta T \\ &= \frac{2}{h} \int_{-\infty}^{\infty} dE \mathcal{T}(E) \left[A(E)|_{\substack{\Delta T=0 \\ \Delta\mu=0}} + \frac{\partial A(E)}{\partial \Delta\mu}|_{\substack{\Delta T=0 \\ \Delta\mu=0}} \Delta\mu + \frac{\partial A(E)}{\partial \Delta T}|_{\substack{\Delta T=0 \\ \Delta\mu=0}} \Delta T \right] \end{aligned} \quad (4.8)$$

The first term in the Taylor expansion is zero, and the two remaining terms reduce down to the derivatives of the two Fermi distribution functions

$$\frac{\partial A(E)}{\partial \Delta\mu}|_{\substack{\Delta T=0 \\ \Delta\mu=0}} = -(E - \mu)^p \frac{\partial f(E)}{\partial E}$$

$$\frac{\partial A(E)}{\partial \Delta T}|_{\substack{\Delta T=0 \\ \Delta\mu=0}} = -\frac{(E - \mu)^{p+1}}{T} \frac{\partial f(E)}{\partial E}$$

where $f(E) = \left(1 + e^{\frac{E - \mu}{k_B T}} \right)^{-1}$ is the Fermi distribution function. Substituting these terms into the Taylor expansion (4.8) and writing the chemical potential in terms of the applied electrical bias $\Delta\mu = e \Delta V$ the currents in the linear regime can be written

$$\begin{aligned} I^p &= \frac{2e}{h} \int_{-\infty}^{\infty} dE \mathcal{T}(E) (E - \mu)^p (-1) \frac{\partial f(E)}{\partial E} \Delta V \\ &\quad + \frac{2}{h} \int_{-\infty}^{\infty} dE \mathcal{T}(E) \frac{(E - \mu)^{p+1}}{T} (-1) \frac{\partial f(E)}{\partial E} \Delta T \end{aligned}$$

We can obtain the thermoelectric coefficients G , L , M and K from above equation

$$G = \frac{2e^2}{h} \int_{-\infty}^{\infty} dE \mathcal{T}(E) (-1) \frac{\partial f(E)}{\partial E} \quad (4.9)$$

$$L = \frac{2e}{h} \int_{-\infty}^{\infty} dE \mathcal{T}(E) \frac{(E - \mu)}{T} (-1) \frac{\partial f(E)}{\partial E} \quad (4.10)$$

$$M = \frac{2e}{h} \int_{-\infty}^{\infty} dE \mathcal{T}(E) (E - \mu) (-1) \frac{\partial f(E)}{\partial E} \quad (4.11)$$

$$K = \frac{2}{h} \int_{-\infty}^{\infty} dE \mathcal{T}(E) \frac{(E - \mu)^2}{T} (-1) \frac{\partial f(E)}{\partial E} \quad (4.12)$$

It should be noted, that the integrals in above equations (4.9)-(4.12) look like the n^{th} central moments L_n of a probability function $P(E)$ which can be defined as:

$$P(E) = -\mathcal{T}(E) \frac{\partial f(E)}{\partial E}$$

However, $P(E)$ is not a real probability distribution function, since

$$\int_{-\infty}^{\infty} dE P(E) \neq 1$$

Let's define L_n as a quantity

$$L_n \equiv \int_{-\infty}^{\infty} dE (E - \mu)^n P(E) = \langle (E - \mu)^n \rangle \quad (4.13)$$

By substituting (4.13) into equations (4.9)- (4.12), the measurable thermoelectric coefficients can be written as

$$G = \frac{2e^2}{h} L_0$$

$$\begin{aligned}
 S &= -\frac{1}{e} \frac{L_1}{T L_o} \\
 \Pi &= \frac{-1}{e} \frac{L_1}{L_o} \\
 \kappa &= \frac{2}{hT} \left(L_2 - \frac{L_1^2}{L_o} \right)
 \end{aligned}$$

Normalizing all functions such that $\tilde{L}_n = L_n/L_o$, the integrals \tilde{L}_n are now the central moments of a true probability distribution function:

$$\tilde{L}_n = \int_{-\infty}^{\infty} dE (E - \mu)^n \tilde{P}(E) = \int_{-\infty}^{\infty} dE (E - \mu)^n \frac{P(E)}{\int_{-\infty}^{\infty} dE P(E)} \quad (4.14)$$

Since

$$\int_{-\infty}^{\infty} dE \tilde{P}(E) = 1$$

Therefore, the thermoelectric coefficient formulas can be reduced to

$$\begin{aligned}
 G &= \frac{2e^2}{h} L_o \\
 S &= -\frac{1}{eT} \tilde{L}_1 \\
 \Pi &= \frac{1}{e} \tilde{L}_1 \\
 \kappa &= \frac{2}{hT} L_o (\tilde{L}_2 - \tilde{L}_1^2)
 \end{aligned}$$

and the Figure of merit (4.5) can be expressed

$$ZT = \frac{\tilde{L}_1^2}{\tilde{L}_2 - \tilde{L}_1^2}$$

In this case \tilde{L}_1 is the expectation value \bar{E} of the distribution, and $\tilde{L}_2 - \tilde{L}_1^2$ is its variance σ^2 . This therefore means that both the thermopower and figure of merit are all determined by the shape of the probability distribution $P(\tilde{E})$, instead of

its absolute magnitude, for instance:

$$S = -\frac{1}{eT}\bar{E}$$

$$ZT = \frac{\bar{E}^2}{\sigma^2}$$

Bibliography

- [1] D. J. Mowbray, G. Jones, and K. S. Thygesen, "Influence of functional groups on charge transport in molecular junctions", *The Journal of Chemical Physics*, vol. 128, no. 11, p. 111103, 2008.
- [2] J. Slyom, "Fundamentals of the Physics of Solids: Volume 3 - Normal, Broken-Symmetry, and Correlated Systems. Theoretical Solid State Physics: Interaction Among Electrons", Springer, 2010.
- [3] L. P. Kadanoff, G. Baym, and D. Pines, "Quantum Statistical Mechanics: Green's Function Methods in Equilibrium and Nonequilibrium Problems", *Advanced book classics*, Perseus Books, 1994.
- [4] L. V. Keldysh, "Diagram technique for nonequilibrium processes", *Sov. Phys.JETP*, vol. 20, no. 4, pp. 1018-1026, 1965.
- [5] C. Caroli, R. Combescot, P. Nozieres, and D. Saint-James, "A direct calculation of the tunnelling current: IV. Electron-phonon interaction effects", *Journal of Physics C: Solid State Physics*, vol. 5, no. 1, p. 21, 1972.
- [6] A. Rocha, V. Garca-Surez, S. Bailey, C. Lambert, J. Ferrer, and S. Sanvito, "Spin and molecular electronics in atomically generated orbital landscapes", *Physical Review B*, vol. 73, Feb. 2006.
- [7] M. Bttiker, Y. Imry, R. Landauer, and S. Pinhas, "Generalized many-channel conductance formula with application to small rings", *Phys. Rev. B*, vol. 31, pp. 6207-6215, May 1985.

- [8] S. Datta, "Electronic Transport in Mesoscopic Systems", (Cambridge Studies in Semiconductor Physics and Microelectronic Engineering). Cambridge University Press, May 1997.
- [9] U. Sivan and Y. Imry, "Multichannel Landauer formula for thermoelectric transport with application to thermopower near the mobility edge", Phys. Rev. B, vol. 33, pp. 551-558, Jan. 1986.
- [10] N. R. Claughton and C. J. Lambert, "Thermoelectric properties of mesoscopic superconductors", Phys. Rev. B, vol. 53, pp. 6605-6612, Mar. 1996.

Chapter 5

Crown Ethers

5.1 Introduction

Crown ether is a general name for macrocyclic polyethers containing ethylene bridges separating electronegative oxygen atoms. They typically contain a central electron rich hydrophilic cavity which range in diameter from 1.2-6.0 Å. The hydrophilic cavity is ringed with electronegative binding atoms such as oxygen, nitrogen, sulphur etc. (Figure 5.1), and are surrounded by a belt of $-CH_2$ groups enabling a structure which is flexible and exhibits hydrophobic behaviour.

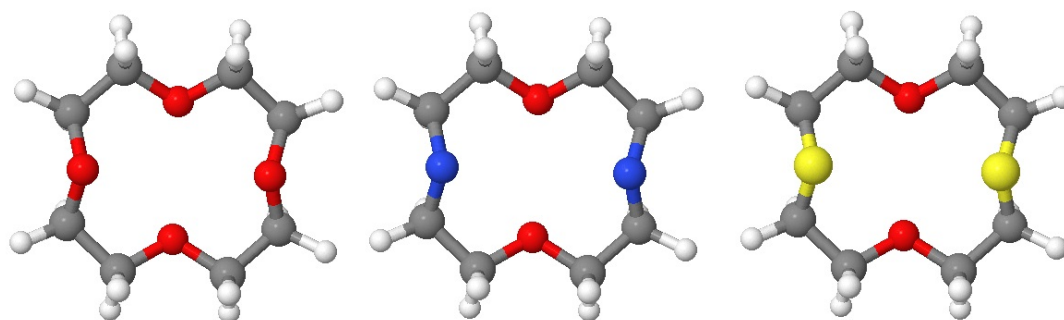


Figure 5.1: 12-Crown-4, red oxygen atoms, blue nitrogen, yellow sulfur, gray carbon and white hydrogen

The hydrophobic exteriors allow them to solubilize ionic materials into non-aqueous solutions. Macrocyclic polyethers create more stable complexes than open chains because the cation is completely surrounded by a cyclic macrocycle. Thus, when the inorganic cation fits into the cavity of a crown ether or is sandwiched

between two crown ether molecules, it becomes a lipophilic species.

5.2 Types of Crown Ethers

There are three types of crown ethers:

- 1- Coronands: Cyclic compounds. Coronands containing oxygen as donor atoms are called crown ethers, those containing oxygen and nitrogen as donor atoms are called diaza-crown ethers, and others containing oxygen and sulphur as donor atoms are called thio-crown ethers. (see Figure 5.1)
- 2- Cryptands : Macropolycyclic polyethers and are classified into bicyclic, tricyclic and tetracyclic. (see Figure 5.2)
- 3- Podands: Open chain compounds and are characterized by lacking ring and bridge structures (again in Figure 5.2) [1,2].

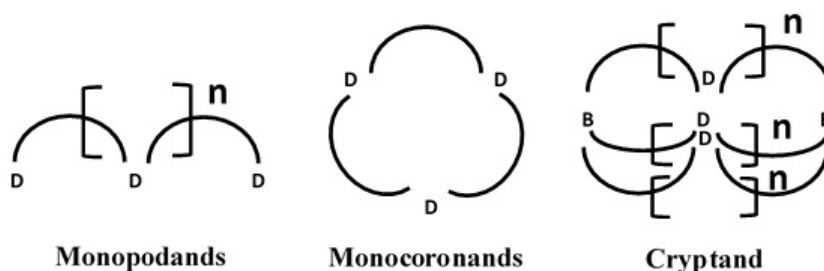


Figure 5.2: Topology and classification of crown ethers, (D: donor atom, B: bridgehead atom and \frown : chain segment without donor atom).

5.3 Nomenclature of Crown Ethers

The IUPAC names for the crown ethers are highly complex and therefore an ad-hoc naming system has been invented. These names are based on the number and types of hydrocarbon rings, the total number of atoms in the ring, the class name 'crown' and the number of oxygen atoms in the polyether ring, e.g., 1,4,7,10,13,16-hexaoxa cyclooctadecane is designated as 18C6. Here, "18" indicates the total

number of atoms in the polyether ring while "6" denotes the number of donor oxygen atoms in the polyether ring. Additional substituents like dibenzo or dicyclohexano are written first, e.g. Dibenzo-18-Crown-6, Dicyclohexano-18-Crown-6. The significant change to the basic crown ether system is the replacement of the oxygen donor atoms by nitrogen or sulfur atoms to get a much easier ligand for binding to transition metals [3].

5.4 Properties of Crown Ethers

Different groups of crown ethers are characterized by their different properties, for example colour, solubility, melting point and characteristic absorption peaks. Crown ethers with aromatic side rings are colourless crystalline compounds. The saturated crown ethers are colourless, viscous liquids or solids of low melting point which are much more soluble in all solvents than their aromatic precursors.

Complexing with a cation brings about distinctive changes in the absorption band, generally by the appearance of a second peak at about 280 nm, with a changed absorbance of the main band. The molar absorptivity of these compounds varies from $1.2 - 8.4 \times 10^{-3} \text{ cm}^{-1} \text{ mole}^{-1}$. The infrared spectra of aromatic as well as aliphatic crown ether shows the presence of ether linkages by a strong broad band around 1230 cm^{-1} for aromatic-O-aliphatic and a band at 1100 cm^{-1} for aliphatic-O-aliphatic group [4-7].

5.5 Size Fitting of the Cation

The size of the cation and the cavity diameter of the crown ether are of great importance for "Size-fitting" or "Size-matching". If the size of the cation matches the cavity diameter of the crown ether, the metal ion is trapped (Figure 5.3). Smaller cations are strongly solvated and more energy is required for desolvation (selected data are shown in table 5.1). However, larger cations are unable to attract the ligand. The selectivity of metal ions for crown ethers can not always be ascer-

tained on the basis of the size of the cation as well as on the cavity diameter of crown ether. Thus, 15C5 shows maximum affinity for potassium in methanol, even though the diameter of sodium ion is closer to the cavity diameter of 15C5. Sometimes, the complex forms with a relatively smaller ion in comparison with the cavity diameter of the crown ether, due to a large electrostatic stabilization energy e.g, extraction of gallium from hydrochloric acid medium in the 18C6 [8–11].

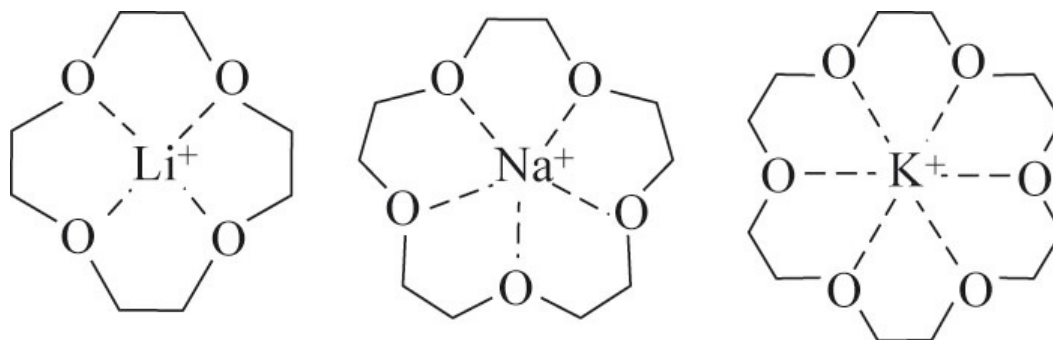


Figure 5.3: "Host-guest" complexes formed from crown ethers and ions of alkaline metals.

Compound	Cavity Diameter (Å ^o)	Ion	Ionic Diameter (Å ^o)
12C4	1.2	Li+	1.46
14C4	1.54	Li+	1.46
15C5	1.8	Na+	2.04
18C6	2.8	K+	2.76
21C7	3.8	Rb+	2.98

Table 5.1: Diameters of crown ether cavities and alkali metal ions [12]

5.6 Crown Ethers Applications

Crown ethers have divers applications in multiple fields:

- 1- Industry (purification, condensation, separation, recovery and removal of salts and rare metals, noble metals, and heavy metals and separation of isotopes).
- 2- Electrochemistry (ion transport, non-aqueous electrolysis).
- 3- Organic chemistry (reaction mechanisms and kinetics, organic synthesis, particularly as a phase transfer catalysis in polymerization).

- 4- Analytical chemistry (ion-selective electrodes, polarography and metal assay).
- 5- Environmental chemistry (capture and removal of harmful metal ions, treatment of nuclear waste).
- 6- Biochemistry and biophysics (ionophore models).
- 7- Drugs and agrochemical (removal of harmful metal ions or supply of essential metal ions and in cancer treatment). [13–16]

5.7 Selectivity of Crown Ethers

It is well known that crown ethers have high binding constants, that are achievable with alkali metals. Ligands are only found when the correct macrocycle is used for a given metal ion. For the alkali metals, which are hard cations, hard donor atoms are needed, so suitable macrocycles are the original crown ethers and their derivatives. The various factors influencing complex stability include:

- 1-The ring cavity size, being big enough to accommodate the ion.
- 2- Number of donor atoms in the ligand.
- 3- The donor atoms being held by the backbone with limited flexibility in positions suitable to match the shape of the coordination sphere [17–21] .

5.8 Binding energy

The most important feature for metal ions selectivity with crown ethers is the binding energy (ΔE), which according to the counterpoise method (described in chapter two) is given by

$$\text{BindingEnergy}(\Delta E) = E_{AB}^{AB} - E_A^{AB} - E_B^{AB} \quad (5.1)$$

The selectivities of crown ethers for alkali metal cations complexation have been studied in the gas phase for oxygen crown (OC) for different sizes 12C4 and 15C5 with three alkali metals Li^+ , Na^+ and K^+ (Figure 5.4).

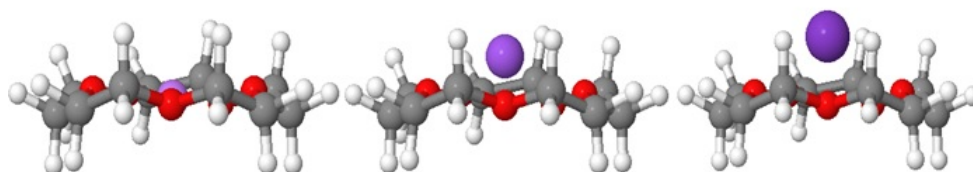


Figure 5.4: Fully optimized minimum energy structure of complex 15C5 with Li^+ or Na^+ or K^+ (left to right)

Our calculations show Li^+ binds strongly with both small and large cavity ring size in gas phase (see table 5-2). These results do not agree with general selectivity rules (size-fitting). It is worth mentioning that for the small size ring cavity (12C4), the ions do not fit inside the cavity. For instance, Li^+ sits above the centre by 1.5 \AA , whereas with relatively large size (15C5), Li fits exactly inside the cavity (distance's column in table 5-2).

Ligand	Cation	ΔE	Distance (\AA)
12C4	Li^+	-0.77	1.50
	Na^+	-0.40	2.50
	K^+	-0.56	2.50
15C5	Li^+	-1.59	0.00
	Na^+	-1.03	1.00
	K^+	-1.26	1.50

Table 5-2: Binding energy (ΔE) for different size of OC .

Despite the fact that our results do not agree with these size-matching rules, they do agree with previous DFT studies. For instance, David [22] has found three cations (Li^+ , Na^+ and K^+) fit one size (15C5). In the same way, Yahmin reported that there are two cations (Li^+ and Zn^{2+}), which fit 12C4, two years later the same researcher reported Na^+ and Cd^{2+} , fit 15C5 [23, 24].

The reason for the disagreement between theory and experiment is because the calculations are performed in the gas phase, while most of the experimental mea-

measurements are performed in solutions. So to improve our calculations we recalculate the binding energies in aqueous solution Figure 5.5 shows an example for 15C5 + Li^+ .

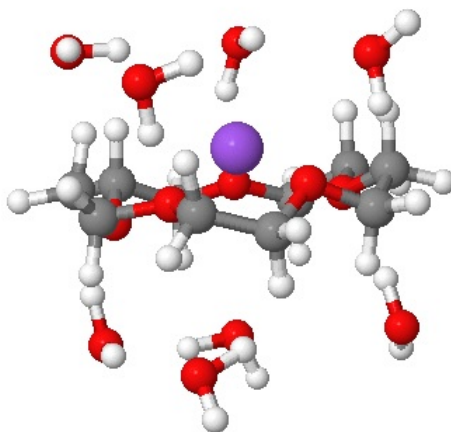


Figure 5.5: Fully optimized minimum energy structure of complex (15C5 + Li^+) in vicinity of water

Table 5 – 3 shows results of the binding energy with a water solution. The values of ΔE have increased for Li^+ and K^+ in the vicinity of solvent for small cavity ring, whereas they have decreased for all ions within the large cavity ring. The selectivity to the alkali ions still does not agree with the size-fitting rules for both cavity sizes.

Ligand + Solvent	Cation	ΔE	Distance (\AA°)
12C4	Li^+	-0.99	1.50
	Na^+	-0.26	2.00
	K^+	-0.68	2.50
15C5	Li^+	-1.16	1.00
	Na^+	-0.75	1.00
	K^+	-0.86	1.50

Table 5-3: Binding energy (ΔE) for different size of OC in vicinity of water.

To benchmark my results with experimental measurements, the size-fitting selectivity concept does not always apply. Doubt has arisen about the validity of this

concept [25], and there are many experimental measurements that do not agree with the size-fitting concept, here I am going to refer to three studies. Luke has found K^+ , fits (12C4) and Na^+ , fits both (15C5) and (18C6) [26]. Costaa has done many studies on two cavity size (18C6) and (21C7), in 2002 he reported that Li^+ fits both of them, and in 2005 he reported another cation Mg^{2+} to fit those cavities size [27,28].

5.9 Structure of Molecular Wires

After studying the binding energy for OC (two size 12C4 and 15C5). I shall now study two types of crown ethers that attached to other units. The structure of each one consists of three parts:

- 1- Central unit Anthraquinone (the three rings with two pendant oxygen/nitrogen atoms).
- 2- Pendant group linked to the central unit which is the crown ether.
- 3- Two arms (alkyl chains that terminated with thiol anchor groups).

I call these mixture (Anthraquinone Crown-Ether-Bridged) (AQC), and the two types of crowns are oxygen crown (OC), diaza-crown (NC, aza=N). So the final labeling is AQOC or AQNC, as shown in the chemical sketch (5.6)

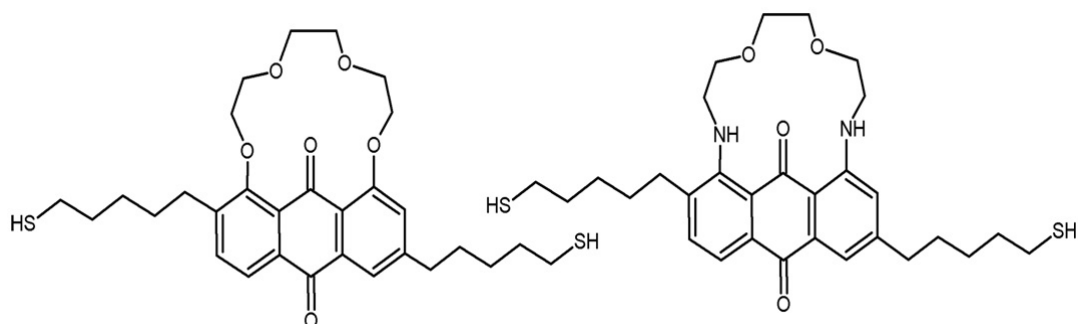


Figure 5.6: Molecular wires containing ether bridges. left AQOC, right AQNC

5.10 Controlled Shifting of Transmission Resonances

To calculate the electronic properties and the electrical conductance of these molecules (AQOC and AQNC) placed between gold electrodes, I use the SIESTA implementation of density functional theory (DFT) [29], combined with the GOLLUM code [30], which is a newly developed quantum transport code. The optimum geometry of the isolated molecule was first calculated using DFT, with all forces on atoms relaxed to a tolerance of 0.01 eV/Å. In all calculations, a double-zeta-plus-polarization (DZP) basis set, with norm-conserving pseudopotentials was employed and the Hamiltonian and overlap matrices were calculated on a real space grid defined by a plane wave cutoff of 200 Ry. After calculating the optimum geometry of the molecular wire, it was attached to gold electrodes as shown in the example of Figure 5.7. After removing the hydrogen atoms from the terminal thiol groups, the equilibrium distance between the S atom and a top atom on the surface of the gold electrode was found to be 2.3 Å (using a counterpoise method (Chap.2)). The gold electrodes consist of tip comprising seven layers of (111) gold with each layer containing 12 gold atoms, connected thereafter to semi-infinite gold leads. A Hamiltonian describing this structure is generated using SIESTA and then GOLLUM is used to calculate the zero bias transmission coefficients $\mathcal{T}(E)$ describing electrons of energy E passing from one electrode to the other via the molecular wire. The electrical conductance is then related to the transmission through the Landauer formula.

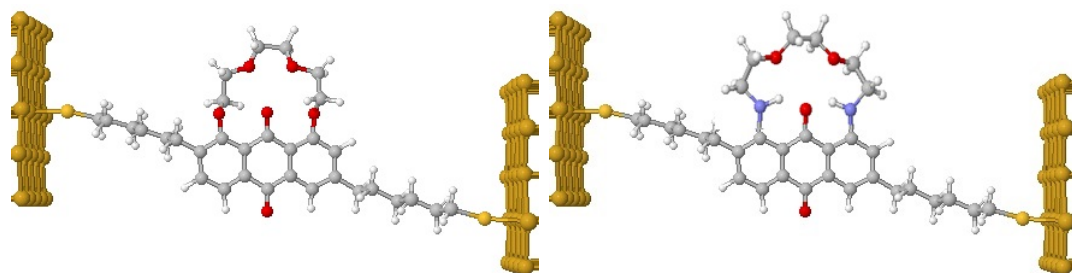


Figure 5.7: Geometry of the molecular junction containing AQOC(12C4) and AQNC(12C4) molecular wire attached between two gold electrodes

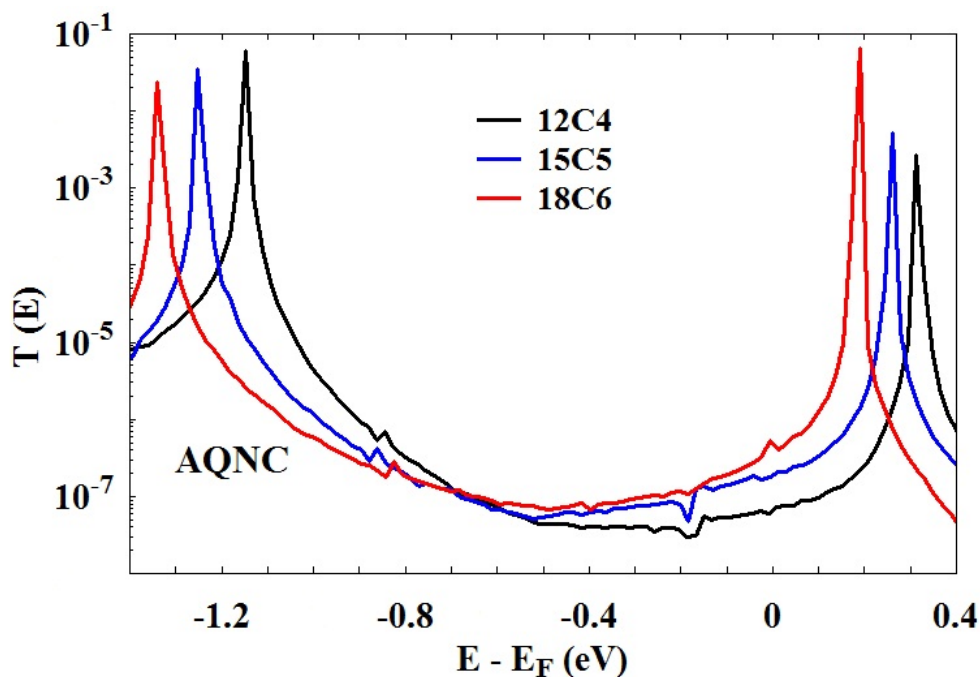


Figure 5.8: Transmission coefficient AQNC (12C4, 15C5 and 18C6)

Figure 5.8 shows the transmission curves for the AQNC molecule, it is clear that the conductance has increased with increasing the cavity size. We see that the HOMO-LUMO gap is constant for all three molecules, therefore the increase in conductance is due to the shifting of the LUMO resonance closer to Fermi energy. The LUMO resonance for (12C4) is at 0.31 eV while (15C5) has shifted to 0.26 eV, and for the larger ring (18C6) the shifting is much bigger, to about 0.18 eV from the Fermi energy. This shifting can be attributed to an increase in the number of oxygen atoms in the ring.

We see the same behavior in Figure 5.9 for the AQOC based crown ether. Here the difference is the AQOC molecule has an anti-resonance in the HOMO-LUMO gap, this anti-resonance has been shifted from -0.58 eV (12C4) to -0.92 eV (18C6). Again the increase in conductance is due to the increase in the number of oxygen atoms shifting the LUMO, but also shifting the position of the anti-resonance. Anti-resonances are very important feature in in quantum interference, as they open up the possibility of controlling quantum transport and may be a useful tool in the design of molecular sensors. The anti-resonance here is due to the different

transmission paths an electron can take.

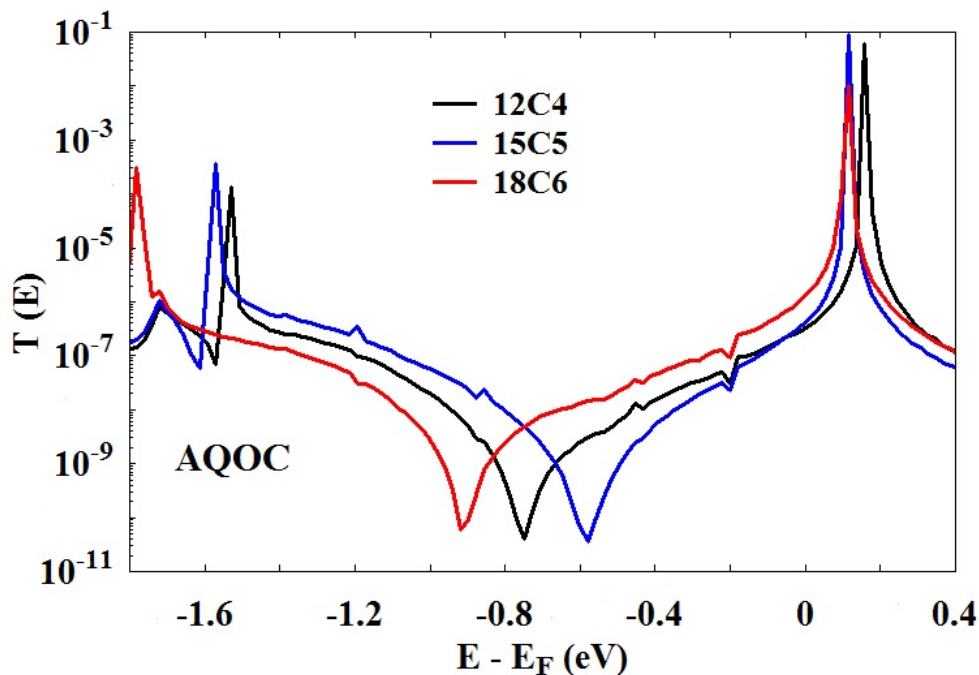


Figure 5.9: Transmission coefficient AQOC (12C4, 15C5 and 18C6)

5.11 Sensing Mechanism

As was mentioned previously, crown ethers are ideal molecules, to accommodate alkali cations in their cavity. Figure 5.10 shows a simple diagram of sensing mechanism. Molecule backbone places between the drain and source. A pendant group attached to the molecule backbone and this part is responsible for sensing a target cation for example. In my case the the molecule backbone is Anthraquinone with alkyl linkers to thiol anchors while the pendant group is the crown ether, which will sense the target analyte.

To demonstrate sensing, I examined the effect of varying the positions of the Li^+ cation (and its counter ion PF_6^-), by placing the Li^+ at 245 different positions above the cavity AQOC (12C4), as shown Figure 5.11. In each case I computed the binding energy and the transmission coefficient $\mathcal{T}(E)$.

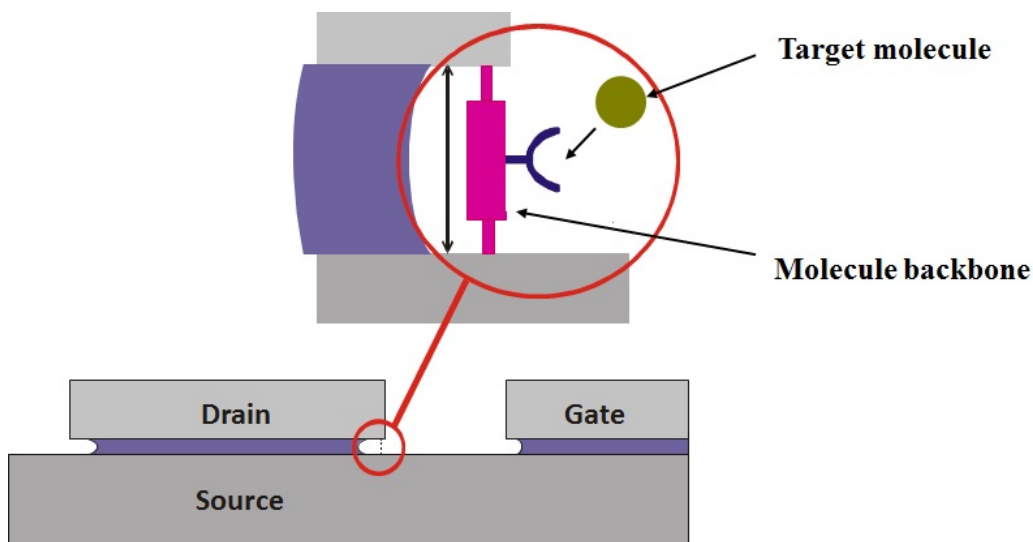
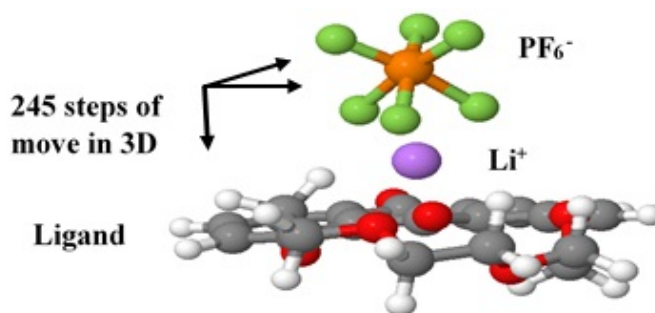


Figure 5.10: Diagram of sensing mechanism

Figure 5.11: Sampling the cation (Li^+ ion) position in the vicinity of AQOC (12C4) cavity. (For clarity the alkyl arms and electrodes are not shown.)

To find what is the most favourable binding position the difference in total energy with the (Li^+ and PF_6^-) at different positions was calculated as shown in Figure 5.12 below. This shows that the strongest binding for (Li^+ and PF_6^-) occurs at position 88 which corresponds to the Li^+ cation being located in the middle of the cavity about 1.5 \AA above the crown (as shown in Figure 5.11 above).

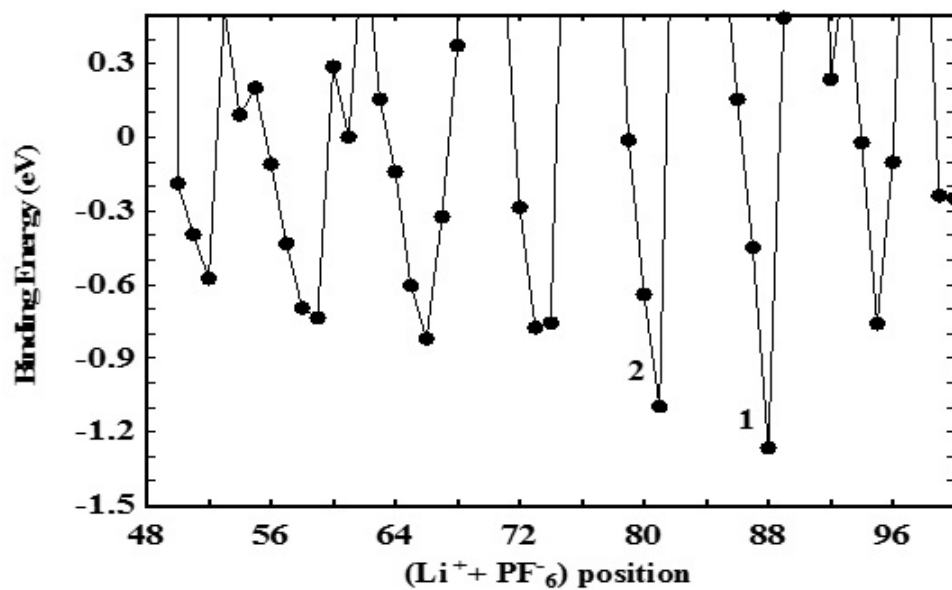


Figure 5.12: Binding energy of AQOC (12C4) as a function of Li^+ position

The transmission coefficients $\mathcal{T}(E)$ for these most favourable binding positions are shown in Fig 5.13)

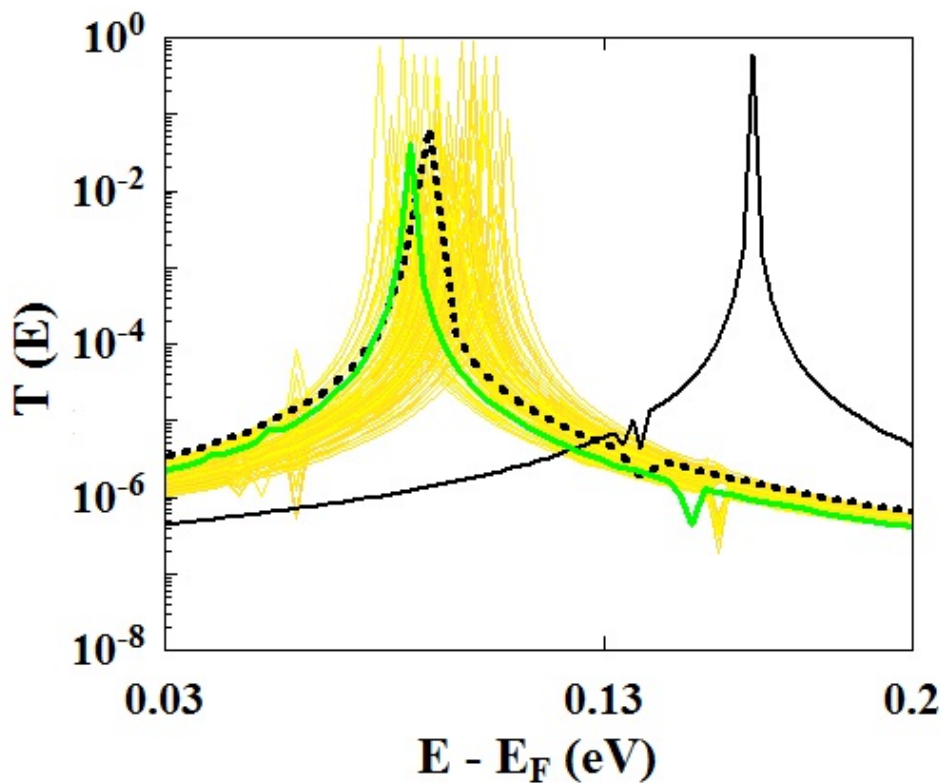


Figure 5.13: Transmission curves, the black dotted line is the transmission curve for the optimum binding of $(Li^+$ and $PF_6^-)$ to AQ (12C4). The yellow curves show the transmission coefficient for a selection of the 245 possible configurations of the 245 possible configurations of $(Li^+$ and $PF_6^-)$ bound to AQ (12C4), whose binding energies are shown in Fig 5.12. The green curve shows the ensemble-averaged transmission $\langle \mathcal{T}(E) \rangle$, obtained by averaging the 245 yellow curves weighted by a Boltzmann factor.

To examine the role of fluctuations, from the 245 transmission curves and their corresponding binding energies E_i , I computed the average transmission curve $\langle \mathcal{T}(E) \rangle$ defined by

$$\langle \mathcal{T}(E) \rangle = \sum_{i=1}^N \mathcal{T}_i(E) \rho_i \quad (5.2)$$

where ρ_i is the Boltzmann factor

$$\rho_i = A e^{-\beta E_i} \quad (5.3)$$

and

$$A = \sum_{i=1}^N e^{-\beta E_i} \quad (5.4)$$

The resulting $\langle \mathcal{T}(E) \rangle$ is shown as the green line in Fig 5.13, which is rather close to the most energetically-favourable transmission curve (black-dotted line) and demonstrates that the difference between this and the bare transmission is not washed out by fluctuations.

To further investigation sensing, calculations are also carried out with three alkali ions, Li^+ , Na^+ and K^+ to form so-called complexes (ligand + ions). To form these complexes we need to add a counter ion in addition to the ion (to maintain neutral charge). PF_6^- and BF_4^- are used as a counter ions, these counter ions are negatively charged whereas cations are positively charged as shown in Figure 5.14.

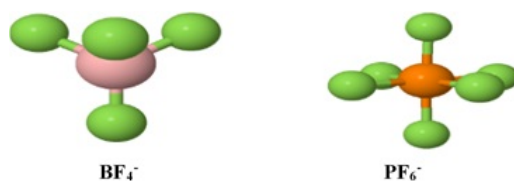


Figure 5.14: Counter ions left BF_4^- and PF_6^- right

Here I am going to focus on one crown size in two different crown ether molecules, these are AQOC (15C5) and AQNC (15C5) Figure 5.15.

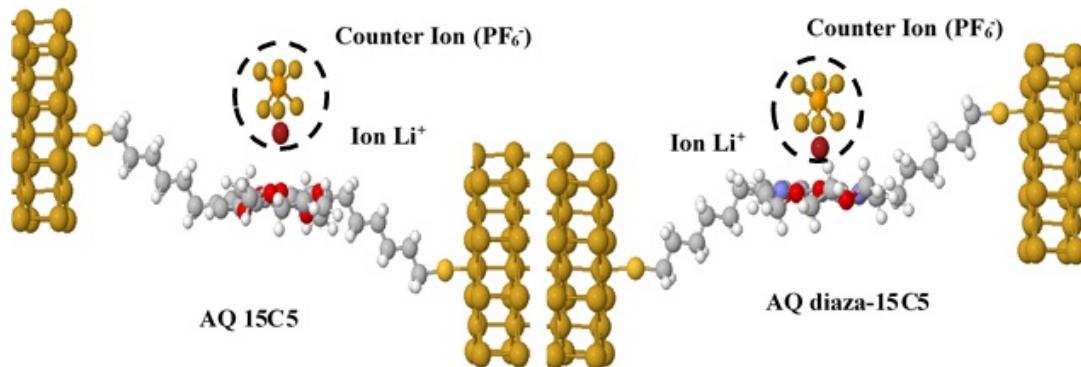


Figure 5.15: Complexes left AQOC (15C5) and AQNC (15C5) right

In Figure 5.16 (AQNC and AQOC) there are four curves one for the bare molecule (*black*) and the rest complexes (*red, blue* and *green*). Bare LUMO resonance at 0.26 eV has shifted to towards Fermi energy by capturing an ion. For example, K^+ ion causes a shifting to 0.06 eV, shifting the LUMO resonance means increasing the conductance (bare 10^{-7} , with ions 10^{-6} at predict $E_F^{DFT} = 0$, and could be up 10^{-4} with slight shift in Fermi, i.g $E_F^{DFT} = 0.05$ for K^+). The sensing in AQNC is bigger than AQOC and different ion causes different sensing (Top panel Figure 5.16).

Lower panel Figure 5.16 shows how we could shift the resonance by trapping ions inside the cavity of the crown and that resulting shift causes an increase in the conductance. We see that the nature of the ion causes different amounts of shifting. This is due to different binding geometry and charging effects.

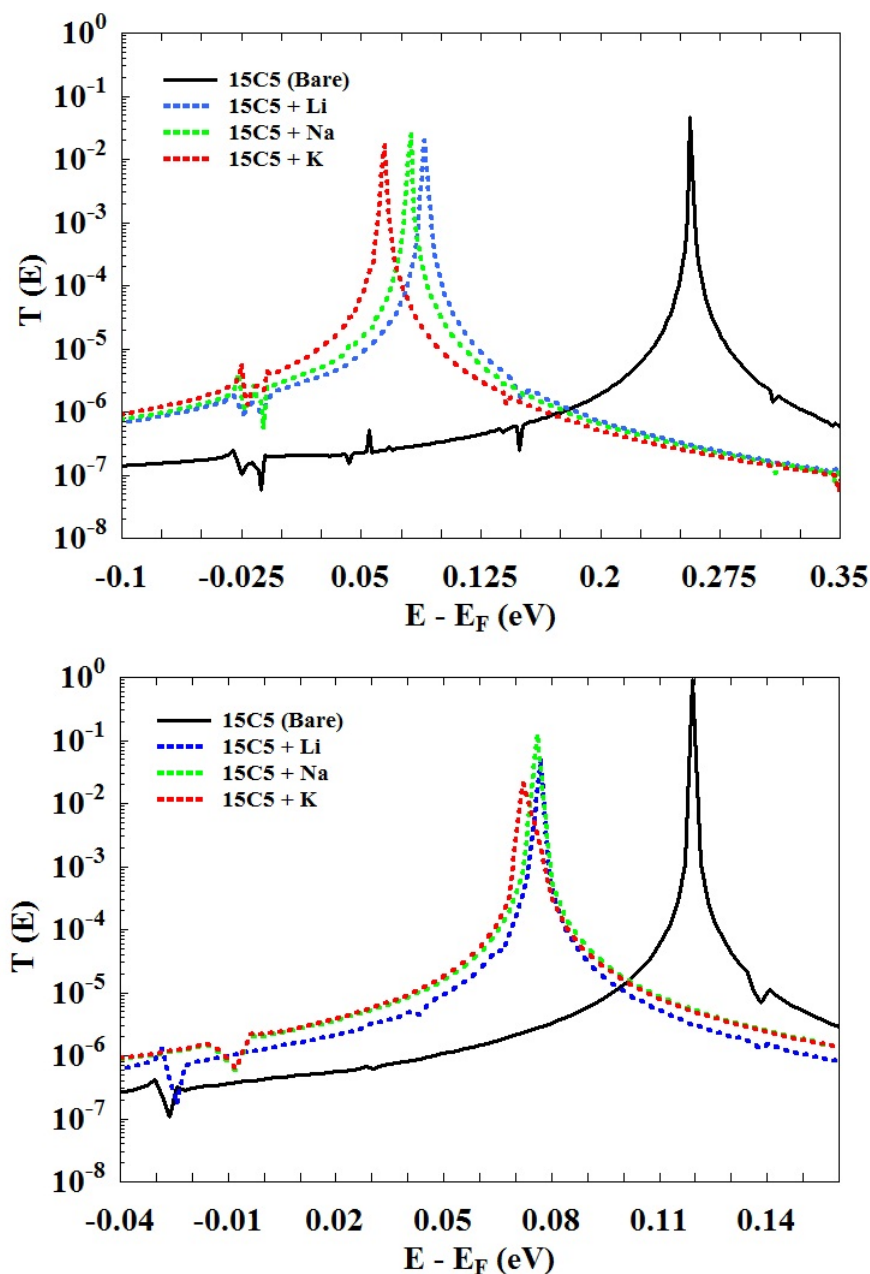


Figure 5.16: Transmission coefficient curves. Top panel AQNC, Lower panel AQOC, both trapped ($15C5$) Li^+ , Na^+ and K^+

The next step is to construct complexes which include two alkali ions K^+ with ligands to form a so-called sandwich (Figure 5.17), the ions lie above and below the crown ether.

Adding another ion with its counter ion results in more shifting to the left of the LUMO resonance, toward low energy for both complexes as shown in Figures 5.18 and 5.19. The bare LUMO resonance for AQNC has shifted from 0.26 eV to 0.06 eV for one ion and to 0.04 eV for two ions.

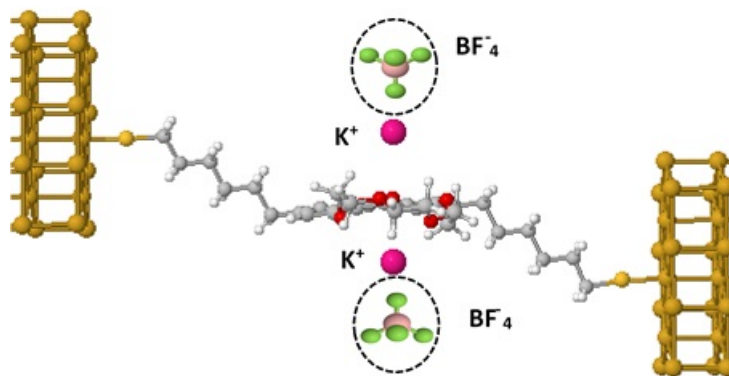


Figure 5.17: Sandwich (two ions, above and beneath the ligand) *AQOC* (15C5), BF_4^- counter ion

Although G is roughly the same for one and two ions at the DFT predicted Fermi energy $E_F^{DFT} = 0$, but could be different with slight shift in Fermi, and again the difference between the bare case and with two ions is still large (Figure 5.18).

Figure 5.19 the bare LUMO resonance (*AQOC*) shifted from 0.11 eV to 0.07 eV when there is one ion K^+ and the second K^+ has increased the shift to 0.04 eV. In this case (*AQOC*) the difference is clear between one and two ions. This opens up the possibility to control the shifting of the resonance, and the behaviour is similar for all these types of ion Li^+ , Na^+ and K^+ , and different cavity sizes.

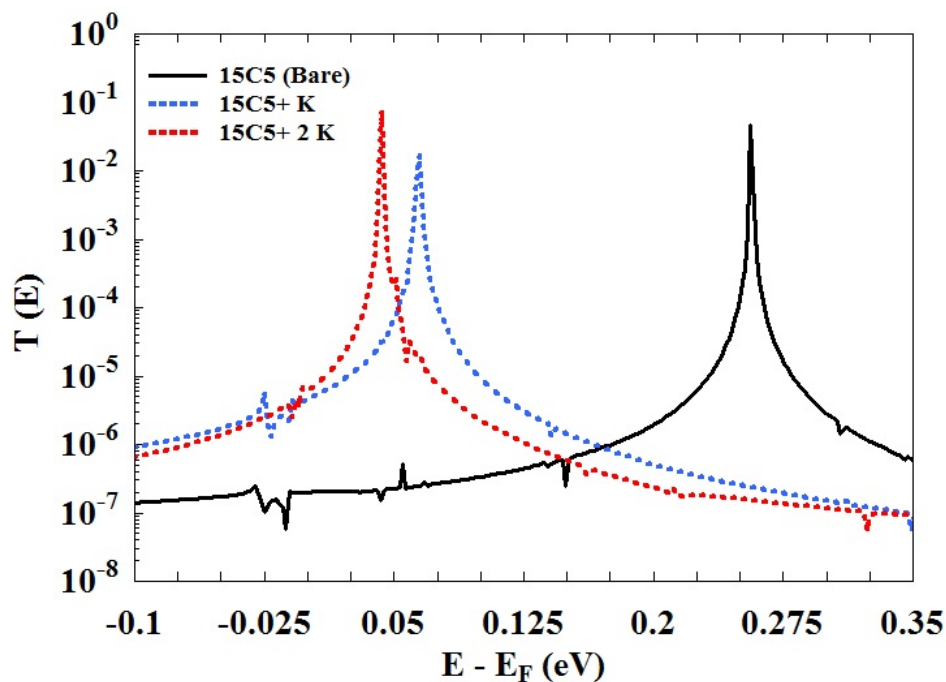


Figure 5.18: Transmission coefficient sandwich *AQNC* (15C5), blue one ion (K^+) and red two ions ($2K^+$)

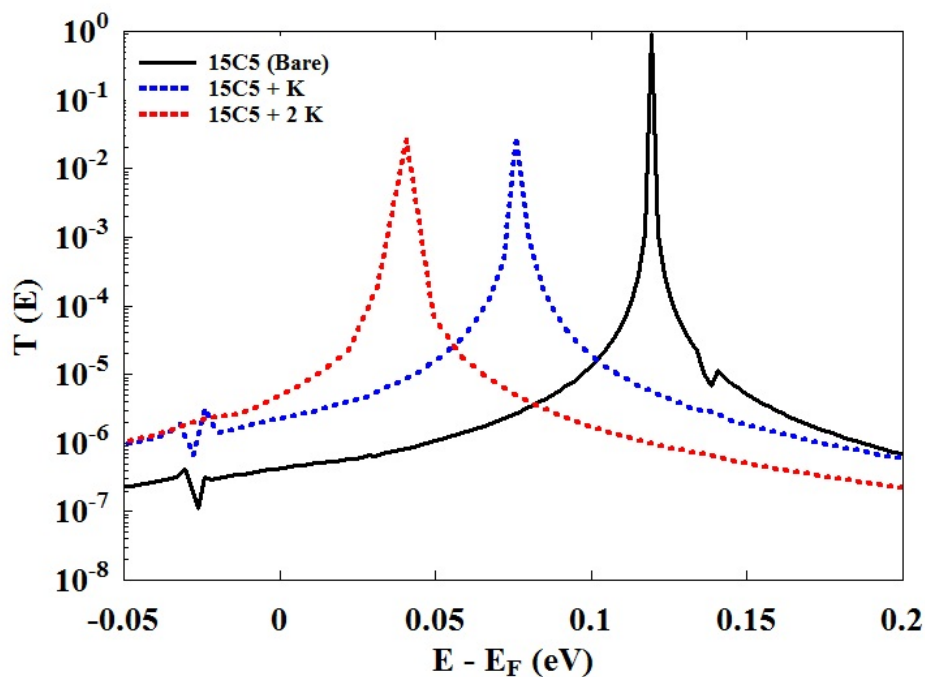


Figure 5.19: Transmission coefficient sandwich AQOC (15C5), blue one ion (K^+) and red two ions ($2K^+$)

To test the role of the counter ion in the transport calculation, I used both BF_4^- and PF_6^- complexed with Li^+ ion, in this calculation for AQOC (15C5). Both counter ions yield the same result as shown in Figure (5.20). Therefore the nature of the counterion is unimportant.

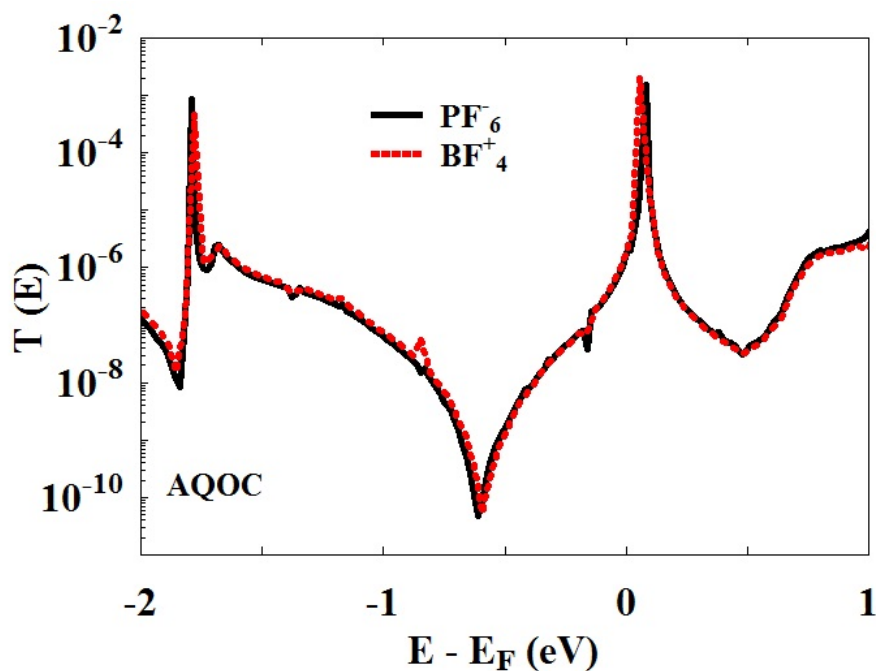


Figure 5.20: Transmission coefficient for AQOC (15C5) with PF_6^- (black) counterion and BF_4^- (red) when complexed with Li^+ ion

5.12 Doping of crown ethers with donor and acceptor molecules

Previously, I have shown that complexing with ions can enhance the conductance. Now, I show how this can be improved further by investigating the effect of forming complexes with molecular donors and acceptors. Tetracyanoethylene (TCNE), is an example of an acceptor and tetrathiafulvalene (TTF) is a donor molecule that I have employed in this study, Figure 5.21 shows the structure of TTF and TCNE.

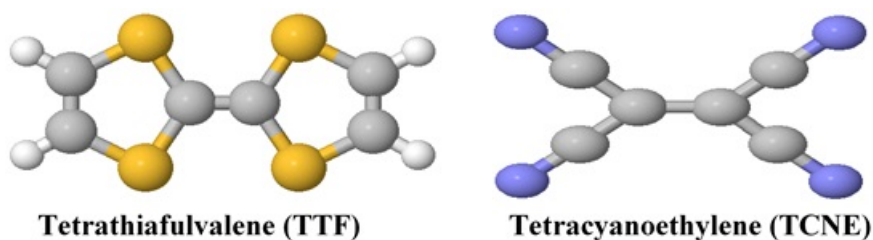


Figure 5.21: Fully relaxed structure of TTF and TCNE

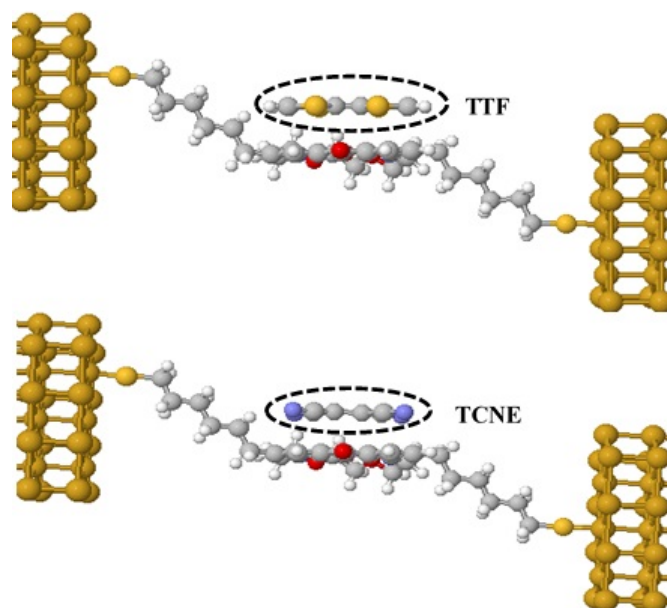


Figure 5.22: Optimum geometry of *AQOC* 15C5 with TTF (Top) and TCNE (Bottom)

Here, I placed in the proximity TTF to *AQOC* (15C5) and TCNE attached to the same ligand (*AQOC*), then I relaxed them to obtain the optimum geometries and connect them to two gold leads, as shown in Figure 5.22. Figure 5.22 shows the formation of a charge transfer complex (optimum geometry). To investigate this shift due to the presence of TCNE, I evaluate the charge transfer from *AQOC* 15C5 backbone to the TCNE molecule using a Mulliken analysis. I find that the TCNE molecule gains 0.21 electrons from the *AQOC* molecular wire, and it is this transfer of charge which shifts the LUMO resonance a way from the Fermi energy to high energies.

While the charge has gained by *AQOC* from TTF is $0.28 e^-$ (the electrons go in the opposite direction of TCNE). For *AQNC* no optimum geometry added (same like *AQOC*), but the transmission curves showed at lower panel of Figure 5.23.

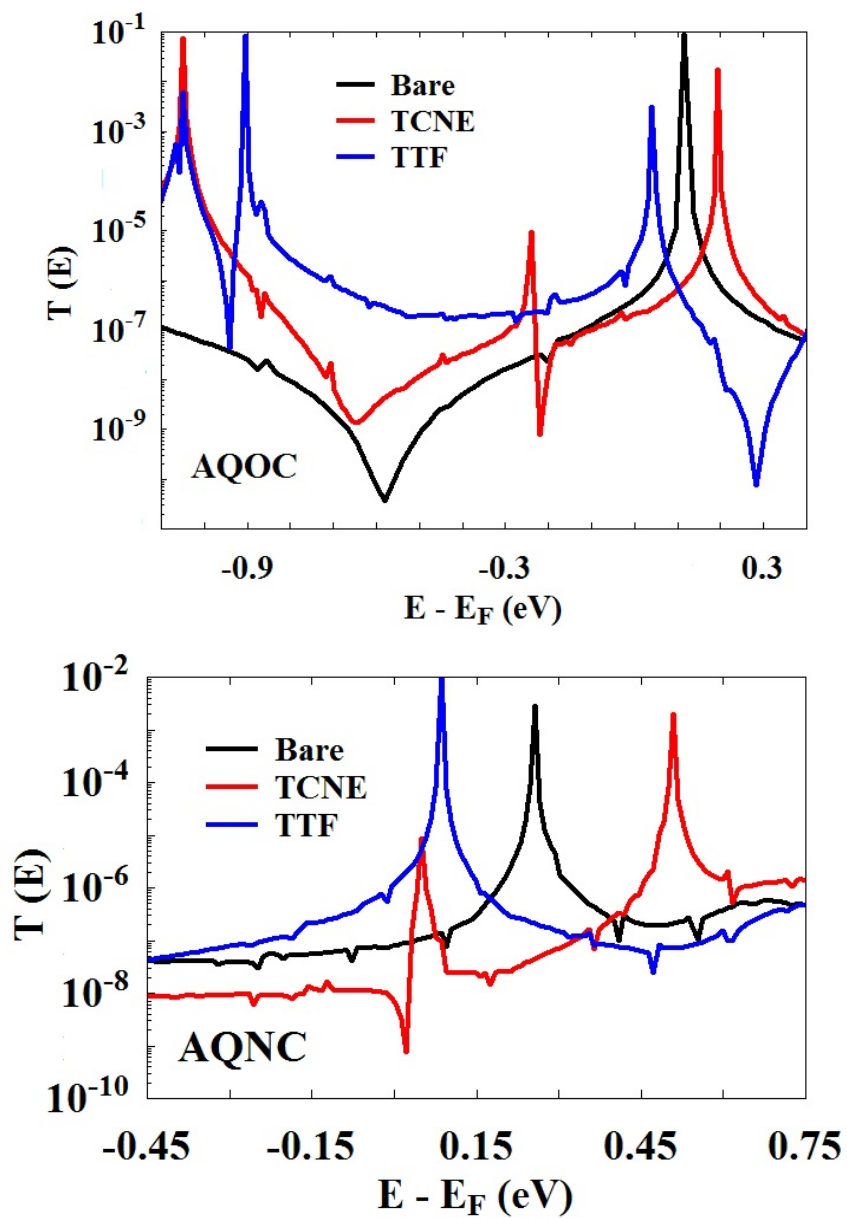


Figure 5.23: Transmission coefficient *AQOC* (15C5) + TTF and TCNE (Top), and *AQNC* + TTF and TCNE (Bottom)

Figure 5.23 Top panel shows the transmission curves in three cases, bare molecule AQOC (15C5), bare with TCNE (red) and bare with TTF (blue). It shows that we have control of shifting the LUMO resonance (around 0.075 eV) either to the left or to the right depending on using donor or acceptor molecule. It is clear *TCNE* has shifted the resonance towards high energy (accepting charge), whereas *TTF* caused shifting in opposite way (donating charge).

Looking at the curves in Figure 5.23 AQNC (15C5), the lower panel shows the same behavior, however, the shifts are much bigger and it is about 0.25 eV to the right and 0.17 eV to the left. Looking at curves in top and bottom we can say in general TCNE molecule has decreased the conductance (for AQNC), in contrary TTF has increased the conductance around Fermi level, but of course, if we speak about the case when we are on resonance (Fano), that is not correct. It is worth mentioning, TCNE has caused a resonance close to the Fermi and that is well known effect for TCNE molecule (both AQNC and AQOC).

5.13 Discriminating sensing of cations in crown-ether-bridged anthraquinones

As it was mentioned before, a crown ether is a molecule, which can accommodate a preferred cation in its hollow. Here, I will examine charge transfer for the six molecules (two types of molecules (AQOC and AQNC), with three different size 12C4, 15C5 and 18C6), the room temperature electrical conductance and some selected binding energies.

For the AQOC molecule, Figure 5.24a shows the transmission coefficient $\mathcal{T}(E)$ for the 3 different-size ether bridges, for energies close to the DFT-predicted Fermi energy (0 eV), which for these series of molecules lies close to the LUMO resonance. The smallest bridge (12C4) has the LUMO resonance at $E-E_F = 0.16$ eV and as the bridge size is increased the LUMO resonance shifts closer to the Fermi energy and thus the conductance is increased. The size of the HOMO-LUMO gap decreases as

the number of atoms in the bridge is increased, leading to the largest bridge (18C6) having the highest conductance. To investigate the sensing properties of the wire, a lithium ion and PF_6^- counter ion (the distance of the counter ion from the ion is 2.35 \AA) is brought into close proximity to the ether bridge. The optimum binding location is found to be at a distance of 1.5 \AA above the centre of the crown-ether ring and the binding energy is -0.77 eV . The transmission coefficient $\mathcal{T}(E)$ in the presence of the lithium is given by the dashed line in Fig 5.24a and shows that the LUMO resonance is shifted by 0.1 eV to $E - E_F = 0.07 \text{ eV}$ and $\mathcal{T}(E_F)$ conductance increases from $8.68 \times 10^{-7} G_0$ (bare case) to $3.6 \times 10^{-5} G_0$, which is over an order of magnitude increase.

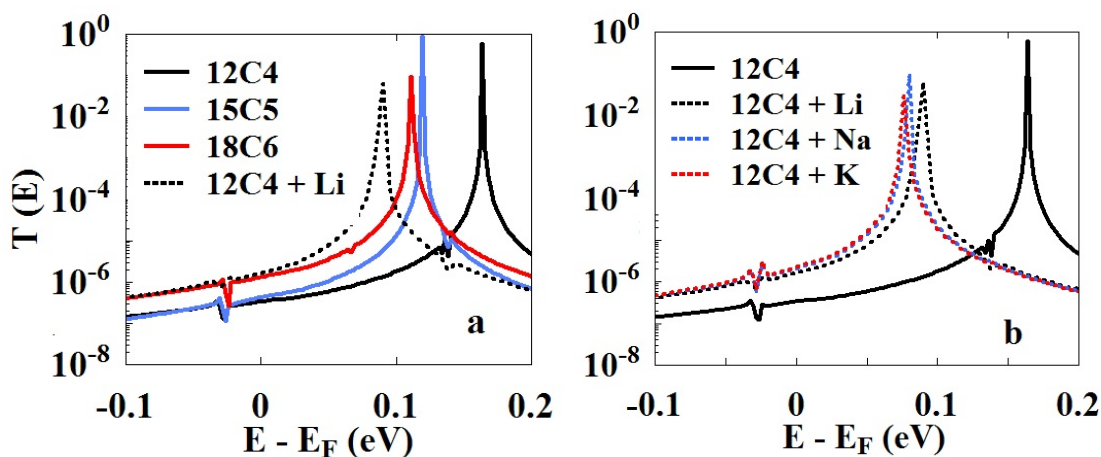


Figure 5.24: Zero bias transmission coefficient, $\mathcal{T}(E)$ of AQOC for different cavity sizes (12C4, 15C5 and 18C6) plus alkali Li^+ (a). Ligand (12C4) with different alkalis Li^+ , Na^+ and K^+ (b)

To investigate this shift due to the presence of an analyte, I evaluate the charge transfer from the lithium ion to the AQOC (12C4) wire using a Mulliken analysis. Here we find that the Li^+ ion donates 0.160 electrons to the molecular wire, and it is this transfer of charge which shifts the LUMO resonance towards the Fermi energy.

Figure 5.24b shows the effect of different metal ions on AQOC (12C4). The Na^+ ion is found to sit a distance 2.50 \AA above the crown and shifts the LUMO resonance to 0.08 eV , which is a greater shift than for lithium. The charge transfer in this case is also greater with 0.172 electrons transferred. The binding energy

is calculated to be -0.40 eV. For K^+ , the resonance shifts even further to 0.07 eV with a charge transfer of 0.193 electrons (ion distance = 2.50 \AA , binding energy = -0.56 eV). This shows that the charge transfer increases with the size of the alkali ion, leading to a difference in the calculated conductance for each type of analyte. The data for the charge transfer for all ions and the six different types of molecular wires is shown in Table 5-4.

	AQOC			AQNC		
Alkali	12C4	15C5	18C6	12C4	15C5	18C6
Li^+	0.306 (0.160)	0.117 (0.076)	0.328 (0.157)	0.341 (0.172)	0.084 (0.011)	0.376 (0.171)
Na^+	0.402 (0.172)	0.183 (0.084)	0.360 (0.155)	0.382 (0.181)	0.191 (0.099)	0.429 (0.181)
K^+	0.550 (0.193)	0.172 (0.073)	0.390 (0.179)	0.392 (0.190)	0.354 (0.113)	0.588 (0.201)

Table 5-4: The non-bracketed numbers show the total number of electrons transferred from the alkali ion to the complex ligands and PF_6^- counterions. The numbers in brackets show the number of electrons transferred to the crown ether, with the remainder transferred to the PF_6^- .

I now repeat the above analysis for the second type of crown-ether bridge. Figure 5.25a shows that for the AQNC molecular wires, increasing the size of the crown again reduces the HOMO-LUMO gap and shifts the LUMO resonance closer to the Fermi energy. For the smallest crown, the LUMO lies at $E-E_F = 0.33 \text{ eV}$, so for this wire, the Fermi energy is furthest from the LUMO, leading to a low transmission coefficient of $\mathcal{T}(E_F) = 7.1 \times 10^{-8}$. Adding the lithium ion (dotted line) shifts the LUMO resonance by 0.2 eV to $E-E_F = 0.11 \text{ eV}$, which is a greater shift than that produced in the AQOC (12C4) wire. The charge transfer (Table 5-4) for this case is 0.172 electrons. Figure 5.25b shows the transmission for the Na^+ and K^+ ions, and again the K^+ produces the largest shift.

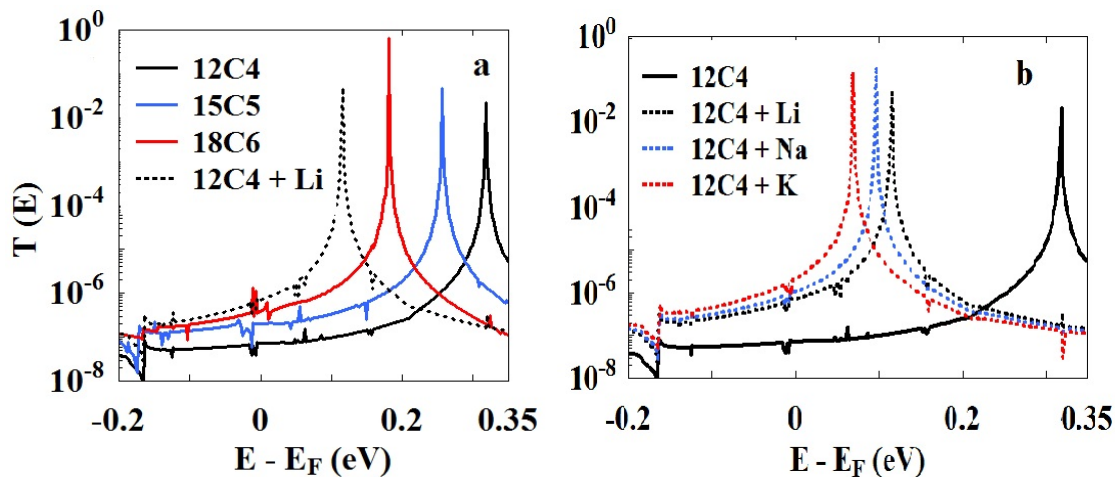


Figure 5.25: Zero bias transmission coefficient, $\mathcal{T}(E)$ of AQNC for different cavity sizes (12C4, 15C5 and 18C6) plus alkali Li^+ (a). Ligand (12C4) with different alkalis Li^+ , Na^+ and K^+ (b)

Figure 5.26 shows the room temperature electrical conductance (in units of the conductance quantum $G_0 = 2e^2/h = 77$ nanoSiemens) of all six molecular wires when the three different ions are added. Compared with the bare wire, the change in conductance increases in the order $K^+ > Na^+ > Li^+$. With the greatest change in conductance occurring for the largest crown (18C6), where there is an increase of over two orders of magnitude. These results clearly show that the response of these wires to analyte binding is analyte specific and can therefore be used to discriminate between analytes.

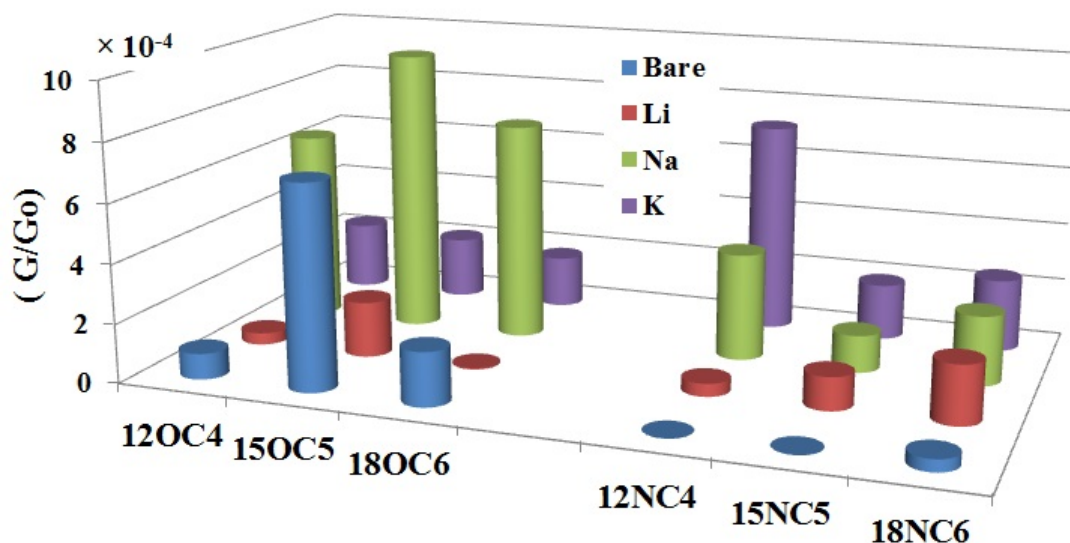


Figure 5.26: The change in conductance, $\mathcal{T}(E)$ calculated at $E_F = 0eV$ for six molecules and three ions (Note: AQOC and AQNC written in short OC and NC on X-axis)

5.14 Thermoelectric properties of crown-ether-bridged anthraquinones

After studying the sensing capabilities of crown-ether-bridged anthraquinones, I now examine the possibility of using analyte binding to modify their thermoelectric properties. The thermopower (or Seebeck coefficient) S of a material or nanoscale device is defined as $S = -\Delta V / \Delta T$, where ΔV is the voltage difference generated between the two ends of a junction when a temperature difference ΔT is established between them, here I am using the same molecules AQOC and AQNC (Figure 5.7).

As is stated in chapter 4, thermopower S is related to the gradient of the transmission curve. I have discussed, adding a cation to the ligand has shifted the LUMO resonance towards Fermi energy (E_F), which means the slope at E_F has been modified and this leads to S changing. The amount of this change depends on the effect of the cation.

To begin with, Figure 5.27 shows the effect of adding three alkali cations (Li^+ , Na^+ and K^+), to both ligands (AQOC and AQNC).

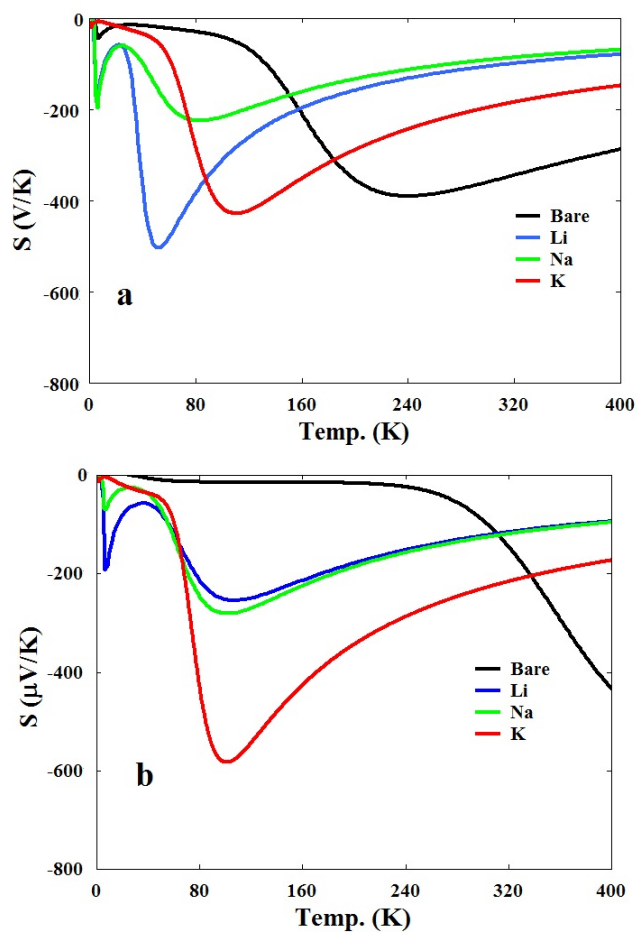


Figure 5.27: The change in thermopower S for different cation compared with the bare (ligand). Top panel AQOC and lower panel AQNC (12C4)

Figure 5.27 Top panel shows the effect of accommodating the Li^+ ion. I find $S \approx -500$ ($\mu V/K$) at low temperature and decreases with increasing T , in case of Na^+ and K^+ have less influence at low temperature. Figure 5.27 Bottom panel shows the thermopower for AQNC ligand. The Figure shows that K^+ increases S for a wide range of temperatures.

To maximise S , my aim is to modify systematically the structures of AQOC and AQNC, by complexing them with combinations of alkali cations and the donor TTF or the acceptor TCNE.

$$L^n(T) = \int_{-\infty}^{\infty} dE (E - E_F)^n \mathcal{T}(E) \left(-\frac{df}{dE}\right) \quad (5.5)$$

From a mathematical viewpoint, equation (5.5) tells us that the coefficient L^1 and hence S is maximised by creating an asymmetric $\mathcal{T}(E)$ in the vicinity of the Fermi energy, because L^1 vanishes when $\mathcal{T}(E)$ is a symmetric function of $(E - E_F)$. This is achieved when $\mathcal{T}(E)$ possesses a sharp maximum located within a few $k_B T$ either above or below the Fermi energy. Chemically, our challenge is to identify optimum combinations of dopants which deliver this feature.

To fully explore the range of accessible thermopowers, I have computed the thermopowers of AQOC and AQNC after binding to different combinations of K^+ , Li^+ or Na^+ cations and complexation with TCNE and TTF. To maintain charge neutrality both PF_6^- or BF_4^- were again used as counter ions. The predicted thermopowers and electrical conductances were found to be the same for both counter ions. In what follows I label each complex (AQOC and AQNC) as either bare (ie 1 or 2 alone), TTF (i.e 1 or 2 with a single adsorbed TTF), TCNE (i.e 1 or 2 with a single adsorbed TCNE), TCNE+K (ie 1 or 2 with a single adsorbed TCNE, a single bound K^+ and its counter ion PF_6^-), TCNE+2K (ie a for AQOC or b for AQNC with a single adsorbed TCNE, two bound K^+ s and their two counter ions PF_6^-), etc.

Figure 5.28 shows that the thermopower S of all such combinations is negative over a wide range of temperature and that the optimum combination of dopants depends on the temperature range of interest. The thermopowers of both 1 and 2 are negative and at room temperature are optimised by binding with TTF alone, achieving thermopowers of $-600 \mu V/K$ and $-285 \mu V/K$ respectively. At much lower temperatures, which are relevant to cascade coolers, I find that for 1, a combination

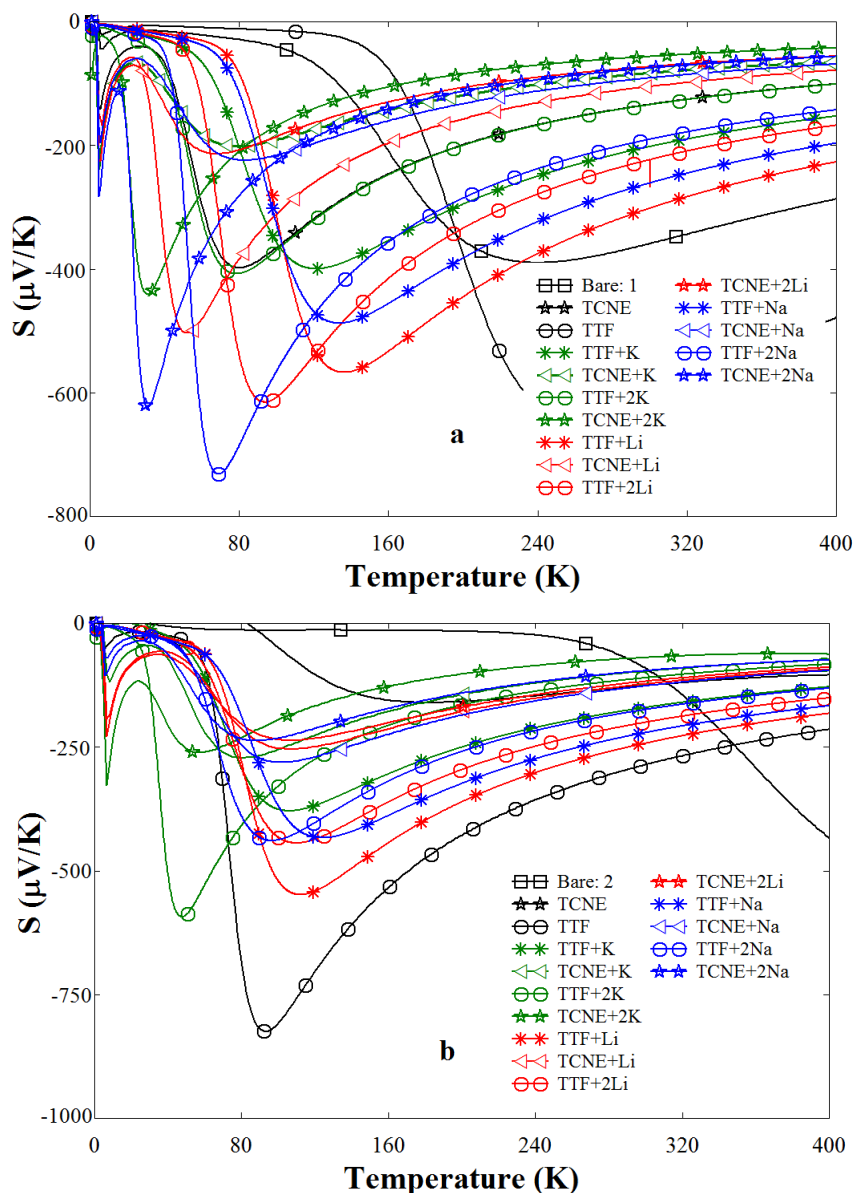


Figure 5.28: Thermopower as function of temperature for complexes of AQOC (a) and AQNC (b)(12C4)

of TTF and 2Na^+ yields a maximum thermopower of $-710 \mu\text{V}/\text{K}$ at 70K , whereas a combination of TTF and 2Li^+ yields a maximum thermopower of $-600 \mu\text{V}/\text{K}$ at 90K . For 2, we find that TTF doping yields a maximum thermopower of $-800 \mu\text{V}/\text{K}$ at 90K , whereas at 50K , the largest thermopower of $-600 \mu\text{V}/\text{K}$ is obtained by a combination TTF and 2K^+ doping.

To highlight correlations between the thermopower and electrical conductance, Figure 5.29 shows plots of thermopower versus electrical conductance at four different temperatures: 250, 300, 350 and 400 K. For all curves apart from bare case (AQNC) in Figure 5.29 b, the temperature increases from the bottom (250K) to the top (400K). These curves show that for most of the complexes, the thermopower becomes increasingly negative with decreasing temperature apart from the bare 2 (AQNC). The 1-TTF has the highest thermopower of $-640 \mu\text{V}/\text{K}$ at 250K, which is higher than any single-molecule thermopower measured to date.

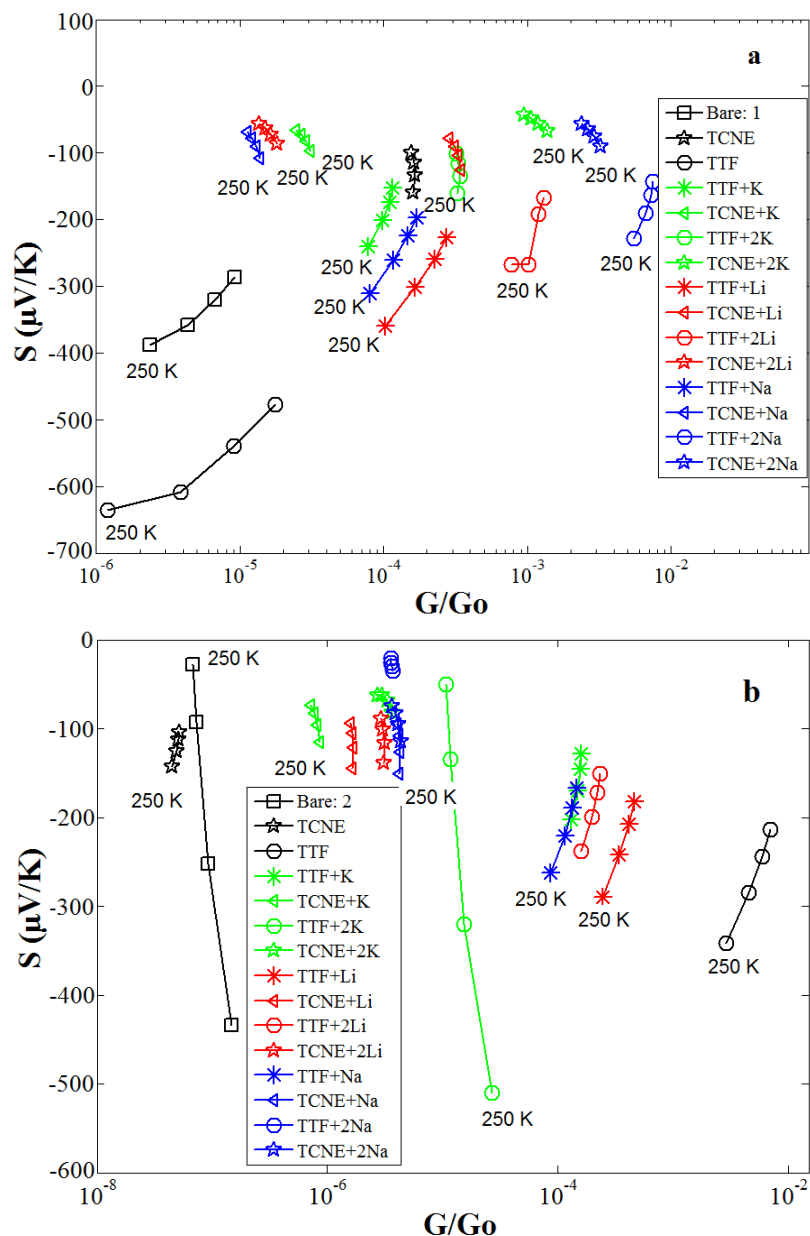


Figure 5.29: Thermopower as function of conductance for complexes of AQOC (a) and AQNC (b) (12C4)

In practice, the dimensionless figure of merit $ZT = (P/\kappa)T$ is difficult to measure experimentally, because the thermal conductance of a single molecule is not directly accessible. However the numerator of ZT (ie the power factor P) is accessible and is defined as $P = S^2\sigma$, where σ is the electrical conductivity. The notion of conductivity is not applicable to transport through single molecules, but to compare with literature values for bulk materials, we define $\sigma = GL/A$, where L and A are equal to the length and the cross-sectional area of the molecule

respectively. In what follows, the values $L = 2.45\text{nm}$ and $A = 7.44\text{nm}^2$ are used. From the results of Figure 5.29, the power factors $P = S^2GL/A$ for each of the studied complexes are shown in Figure 5.30.

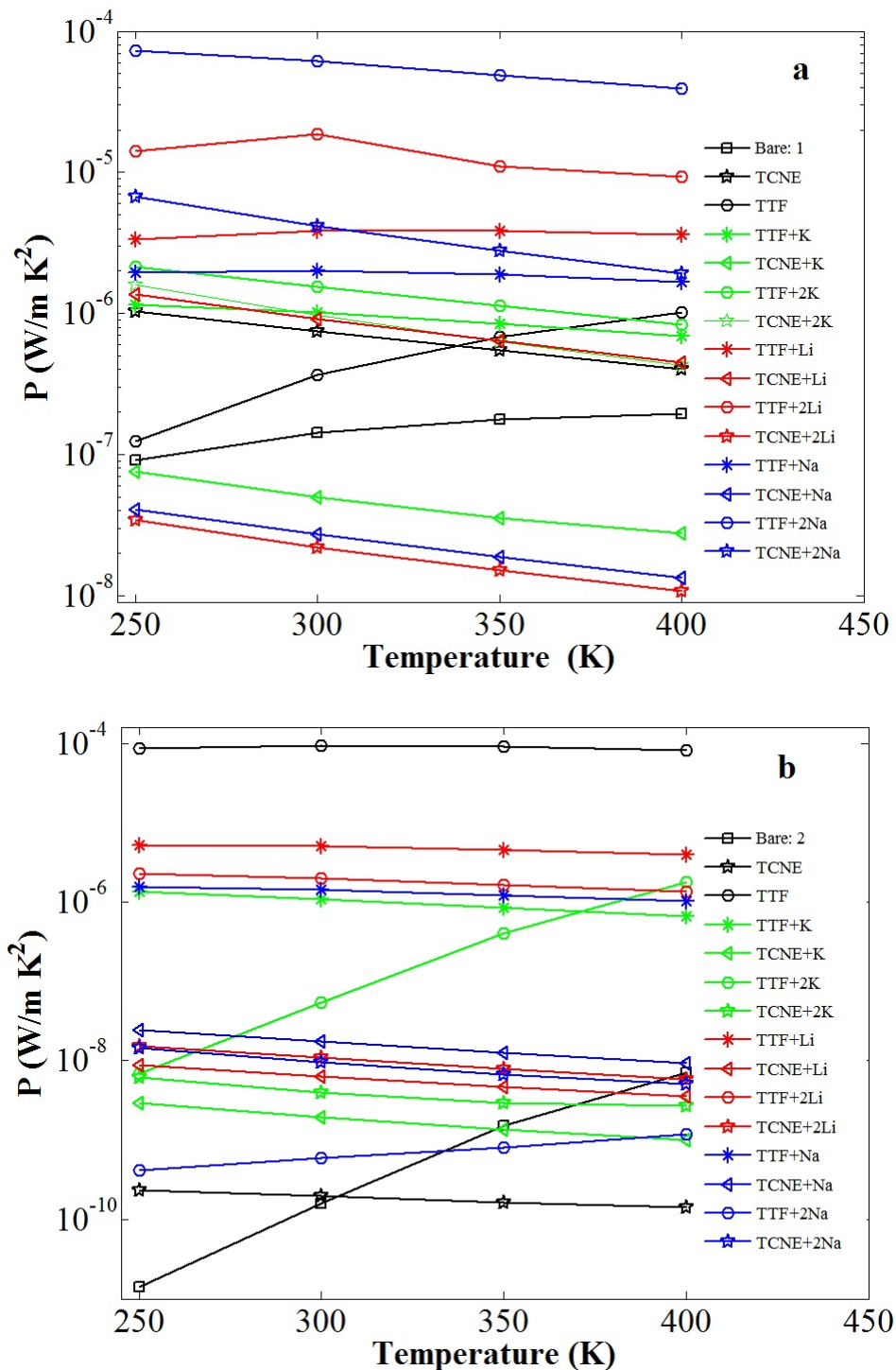


Figure 5.30: Power factor as function of temperature for complexes of AQOC (a) and AQNC (b)

Figure 5.30b reveals that for 2 (AQNC) complexation with TTF and with TTF + Li^+ yields the highest and next-highest power factors respectively, whereas complexation with TCNE has the lowest. Figure 5.30a shows that for 1 (AQOC), complexation with TTF + $2Na^+$ and TTF + $2Li^+$ yield the highest and next-highest power factors respectively, while complexation with TCNE + $2Li^+$ yields the lowest. In all cases, these reflect the positions of transmission resonances relative to the Fermi energy.

The thermoelectric properties of a series of molecular wires have been calculated in the presence of one or two alkali cations and in the presence of acceptor (TCNE) and donor (TTF) molecules. Due to charge transfer between the host and adsorbates, complexation produces a shift in the LUMO transmission resonances, resulting in orders of magnitude variation in both the thermopower and power factor. In the case of TTF the resonance shifts away from the Fermi energy, leading to a decrease in the value of S , while for TCNE, the resonance shifts closer to the Fermi energy, causing the thermopower to increase. At room temperature I find that AQOC doped with TTF possesses the largest calculated thermopower of $-640 \mu V/K$, which is higher than any single-molecule thermopower measured to date. At room temperature, we obtain power factors of $73 \mu W/m.K^2$ for $1+TTF+2Na^+$ and $90 \mu W/m.K^2$ for AQNC + TTF. These compare favourably with power factors of other organic materials, whose reported values range from $0.016 \mu W/m.K^2$ and $0.045 \mu W/m.K^2$ for polyaniline and polypyrrole respectively [31], to $12 \mu W/m.K^2$ for PEDOT:PSS [32] and $(12 \mu W/m.K^2)$ for $C_{60}/C_{s_2}C_{o_3}Dph - BDT$ [33].

This chapter has demonstrated thermoelectric and sensing properties of crown-ether-bridged anthraquinones for two types of crown ether AQOC and AQNC. This study has investigated three size crowns for each type 12C4, 15C5 and 18C6. So in total there are 6 molecules, each one of these have sensed with three alkali cations Li^+ , Na^+ and K^+ and then adopt with either donor and acceptor.

Bibliography

- [1] C. J. Pedersen, "Cyclic polyethers and their complexes with metal salts", Journal of the American Chemical Society 89.26: 7017-7036 1967.
- [2] C. J. Pedersen, "Ionic complexes of macrocyclic polyethers", Federation Proceedings. Vol. 27. No. 6. 1967.
- [3] R. M. Izatt, R. E. Terry, B. L. Haymore, L. D. Hansen, N. K. Dalley, A. G. Avondet and J. J. Christensen, "Calorimetric titration study of the interaction of several uni-and bivalent cations with 15-crown-5, 18-crown-6, and two isomers of dicyclohexo-18-crown-6 in aqueous solution at 25. degree. C and. $\mu = 0.1$.", Journal of the American Chemical Society 98.24 : 7620-7626, 1976.
- [4] C. J. Pedersen, "Crystalline salt complexes of macrocyclic polyethers", Journal of the American Chemical Society 92.2: 386-391, 1970.
- [5] C. J. Pedersen, "Crystalline complexes of macrocyclic polyethers with thiourea and related compounds", The Journal of Organic Chemistry 36.12 : 1690-1693, 1971.
- [6] C. J. Pedersen and H. K. Frensdorff, "Macrocyclic polyethers and their complexes", Angewandte Chemie International Edition in English 11.1 : 16-25, 1972.
- [7] R. Poonia, S. Narinder and V. Amritlal Bajaj, "Coordination chemistry of alkali and alkaline earth cations", Chemical Reviews 79.5 : 389-445, 1979.

- [8] F. P. Remoorter and F. P. Boer, "Cyclomer complexes. Crystal structure of a 2: 1 pentahydrate complex of 1, 4, 7, 10-tetraoxacyclododecane with sodium chloride $[\text{Na}+(\text{C}_8\text{H}_{16}\text{O}_4)_2][\text{Cl}_5\text{H}_2\text{O}]$ ", *Inorg. Chem* 13 : 2071-2078, 1974.
- [9] K. Wong, H. Kam , B. Marc and S. Johannes, "Spectrophotometric detection of ion paircrown ether complexes of alkali picrates", *Journal of the Chemical Society, Chemical Communications* 17: 715-716, 1974.
- [10] P. R. Mallinson and M. R. Truter, "Crystal structures of complexes between alkali-metal salts and cyclic polyethers. Part V. The 1: 2 complex formed between potassium iodide and 2, 3, 5, 6, 8, 9, 11, 12-octahydro-1, 4, 7, 10, 13-benzopentaoxacyclopentadecin (benzo-15-crown-5)", *Journal of the Chemical Society, Perkin Transactions* 2 12 : 1818-1823, 1972.
- [11] A. Cram, J. Donald and J. M. Cram, "Host-Guest Chemistry Complexes between organic compounds simulate the substrate selectivity of enzymes", *Science* 183.4127 : 803-809, 1974.
- [12] L. E. Collie, "Lithium transport in crown ether polymers", Durham theses, Durham University 1995. Available at Durham E-Theses Online: <http://etheses.dur.ac.uk/5196/>
- [13] McDowell, W. Jack, G. N. Case, J. A. McDonough and R. A. Bartsch, "Selective extraction of cesium from acidic nitrate solutions with didodecyl-naphthalenesulfonic acid synergized with bis (tert-butylbenzo)-21-crown-7", *Analytical Chemistry* 64, no. 23 : 3013-3017, 1992.
- [14] M. Hiraoka, "Crown Compounds: Properties and Applications", Tokyo, 1982.
- [15] A. K. Ghosh and Yong Wang, "Synthetic studies of antitumor macrolide laulimalide: a stereoselective synthesis of the C 17C 28 segment", *Tetrahedron Letters* 41.24 : 4705-4708, 2000.

- [16] L. J. Mathias and C. E. Carraher, "Crown Ethers and Phase Transfer Catalysis in Polymer Science", Plenum Press: New York and London, 2003.
- [17] M. A. Thompson, E. D. Glendening and D. Feller, "The nature of K^+ /crown ether interactions: a hybrid quantum mechanical-molecular mechanical study", *The Journal of Physical Chemistry* 98.41 : 10465-10476, 1994.
- [18] E. D. Glendening and D. Feller, "An ab initio investigation of the structure and alkaline earth divalent cation selectivity of 18-crown-6", *Journal of the American Chemical Society* 118.25 : 6052-6059, 1996.
- [19] D. Feller, M. A. Thompson and R. A. Kendall, "A theoretical case study of substituent effects and microsolvation on the binding specificity of crown ethers", *The Journal of Physical Chemistry A* 101.39 : 7292-7298, 1997.
- [20] D. Feller, "Ab initio study of M^+ : 18-crown-6 microsolvation", *The Journal of Physical Chemistry A* 101.14 : 2723-2731, 1997.
- [21] E. D. Glendening, D. Feller and M. A. Thompson, "An ab initio investigation of the structure and alkali metal cation selectivity of 18-crown-6", *Journal of the American Chemical Society* 116.23 : 10657-10669, 1994.
- [22] Zanuy, David, P. Julien, E. A. Perpete and C. Aleman., "Response of crown ether functionalized polythiophenes to alkaline ions", *The Journal of Physical Chemistry B* 116.15: 4575-4583, 2012.
- [23] Y. Yahmin, D. P. Harno and R. Armunanto, "AB INITIO INVESTIGATION OF 12-CROWN-4 AND BENZO-12-CROWN-4 COMPLEXES WITH Li^+ , Na^+ , K^+ , Zn^{2+} , Cd^{2+} , AND Hg^{2+} ", *Indonesian Journal of Chemistry* 10.1 : 106-109, 2010.
- [24] Y. Yahmin, D. P. Harno and R. Armunanto, "THEORETICAL STUDY ON 15-CROWN-5 COMPLEX WITH SOME METAL CATIONS", *Indonesian Journal of Chemistry* 12.2: 135-140, 2012.

- [25] Izatt, Reed M, "The synthesis and ion bindings of synthetic multidentate macrocyclic compounds", *Chemical Reviews* 74.3: 351-384, 1974.
- [26] C. Luke E, "Lithium transport in crown ether polymers", Diss. Durham University, 1995.
- [27] J. Costaa, M Caridade and P. M. S. Rodrigues, "Complexation Study of Alkali Metal Ions by Crown Ether Derivatives in Nonaqueous Solvents by Potentiometric Methods", *Portugaliae Electrochimica Acta* 20: 167-178, 2002.
- [28] J. Costa, M Caridade and P. M. S. Rodrigues, "Complex Formation Between Alkaline-Earth Cations and Anthraquinone Crown Ethers in Methanol and Acetonitrile", *Portugaliae Electrochimica Acta* 23.2: 289, 2005.
- [29] J. M. Soler, E. Artacho, D. G. Julian, G. Alberto, J. Javier, O. Pablo and D. Snchez-Portal, "The SIESTA method for ab initio order-N materials simulation", *J. Phys.: Condens. Mat.* 14, 2745, 2002.
- [30] J. Ferrer, C. J. Lambert, V. M. Garca-Surez, D. Zs Manrique, D. Visontai, L. Oroszlany, Rubn Rodrguez-Ferrads, "GOLLUM: a next-generation simulation tool for electron, thermal and spin transport." *New Journal of Physics* 16, no. 9: 093029., 2014.
- [31] A. Shakouri and Li. Suquan, "Thermoelectric power factor for electrically conductive polymers", In *Thermoelectrics, 1999. Eighteenth International Conference on*, pp. 402-406. IEEE, 1999.
- [32] H. Shi, C. C. Liu, J. K. Xu, H. J. Song, Q. L. Jiang, B. Y. Lu, W. Q. Zhou and F. X. Jiang. "Electrochemical fabrication and thermoelectric performance of the PEDOT: PSS electrode based bilayered organic nanofilms", *Int. J. Electrochem. Sci* 9: 7629-43. 2014.
- [33] M. Sumino, K. Harada, M. Ikeda, S. Tanaka, K. Miyazaki and C. Adachi, "Thermoelectric properties of n-type C60 thin films and their application in

organic thermovoltaic devices”, Applied Physics Letters 99, no. 9: 093308, 2011.

Chapter 6

Fullerenes and Endohedral Metallofullerenes

6.1 Introduction

This chapter is divided into two parts: an experimental part and a theoretical part. I will introduce fullerenes and endohedralfullerenes and then provide a brief description of the STM and associated measurements of the conductance G , thermopower S and power factor P for both C_{60} and $Sc_3N@C_{80}$. The second part starts with answering the question of whether the Sc_3N rotates inside the cage. After finding the binding energy for $Sc_3N@C_{80}$ on gold, I calculate their collective parameters G, S and P . Finally comparing the theory with experiment, I introduce a new concept of "bi-thermoelectricity".

6.1.1 Fullerenes

The possibility of making large hollow carbon cages was first suggested in 1966 by Jones [1], and in 1970 Osawa predicted the existence of C_{60} [2]. It was Kroto and co-workers who first discovered C_{60} in 1985, when they investigated the mass spectra of laser evaporated carbon in a helium atmosphere [3], and a short time after that a fairly symmetric truncated isosahedral structure for C_{60} was suggested

(Figure 6.1).

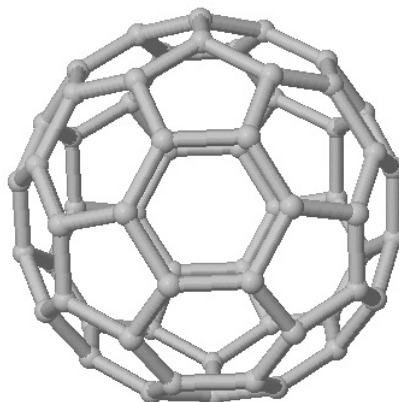


Figure 6.1: Buckminsterfullerene (C_{60})

The symmetric structure was confirmed from ^{13}C nuclear magnetic resonance (NMR) experiments. Due to lack of materials most of the research on fullerenes were theoretical studies [4, 5]

The second striking discovery in the fullerene field was accomplished in 1990 by Kratschmer, Huffman and their groups. They announced an easy way to produce macroscopic quantities of fullerenes (C_{60} , C_{70} and other empty-cages) from the vaporization of inexpensive graphite rods in a helium atmosphere [5]. With this invention, scientists opened the door to large scale fullerene research, which spread out into physics, chemistry and material science [6].

6.1.2 Endohedral Metallofullerenes

Due to the fact that fullerenes are empty molecules, it was foreseeable that it might be possible to accommodate atoms inside the cage. One week after the discovery of C_{60} , the Kroto's group [7] observed the first endohedral metallofullerene, $La@C_{60}$, in the mass spectrum of a sample prepared by laser vaporization of a $LaCl_2$ impregnated graphite rod. The symbol @ is used to mark the atoms in the interior of the fullerene cage. To prove that metal atoms were encapsulated inside the buckyball Smalley and his group [8] found that both C_{60} and $La@C_{60}^+$ complexes did not react with H_2 , O_2 , NO , and NH_3 . This showed that the reactive metal

atoms were protected from the surrounding gases and were indeed trapped inside closed fullerene cages.

Much work has been done in the following years on endohedral metallofullerenes: Chai et al. employed high temperature laser vaporization of $La_2O_3/graphite$ composite rods and the corresponding contacted arc technique to produce macroscopic quantities of lanthanofullerenes [9]. The major lanthanofullerene was $La@C_{80}$ due to its relatively high stability. Two and three metal atoms, can also be engaged into a fullerene. For instance, Shinohara et al [10], produced and isolated a series of scandium metallofullerenes ($Sc@C_{80}$, $Sc@C_{82}$, $Sc_2@C_{84}$ and $Sc_3@C_{84}$) in macroscopic quantities. In recent years, group 3 metals (Scandium, Yttrium and Lanthanum) and most lanthanide metals have been trapped inside the larger fullerenes, such as C_{80} , C_{82} , C_{84} etc., to provide mono-, di- and trimetallofullerenes [11]. Several metal carbide endohedral fullerenes were also synthesized, such as $Sc_2C_2@C_{84}$ and $Sc_3C_2C_{80}$ [12, 13].

6.1.3 Trimetallic Nitride Endohedral Metallofullerenes

In 1999 Stevenson and co-workers [14] produced a four-metallic-atom icosahedrally I_h symmetrical endohedral fullerene, $Sc_3N@C_{80}$ (Figure 6.2 right).

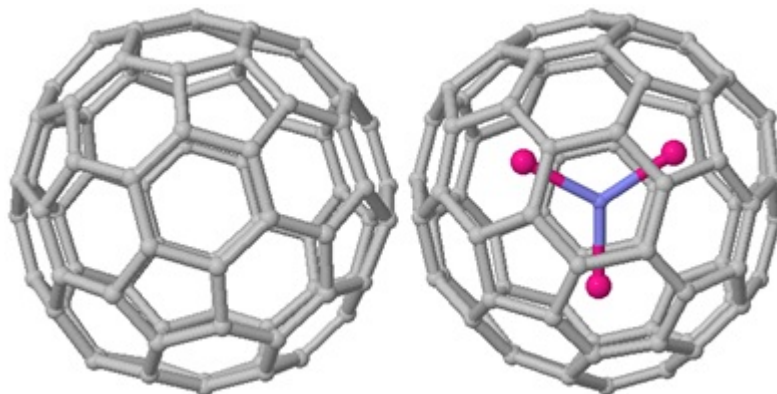


Figure 6.2: I_h isomer (C_{80}), $Sc_3N@C_{80}$

The new molecule was produced by a trimetallic nitride template method (TNT)(vaporizing graphite rods packed with Sc_2O_3 in a Kratschmer-Huffman generator under He/N_2 atmosphere). The TNT method opened the way to produce

a variety of new trimetallic nitride endohedral metallofullerenes with different encapsulated metals and carbon cages, for example: $Sc_3N@C_{80}$ (Figure 6.2 right) or $A_3N@C_{2n}$ ($A = Y, Gd, Tb, Dy, Ho, Er, Tm,$ and Lu) [15]. What is more, a mixture of TNT molecules have been synthesized recently, such as: $Er_xSc_{(3-x)}N@C_{80}$, $CeSc_2N@C_{80}$ and four atoms $ScYErN@C_{80}$ [16, 17].

6.1.4 Production of $Sc_3N@C_{80}$

To produce $Sc_3N@C_{80}$ in a macroscopic amounts, a Kratschmer-Huffman generator is used (Figure 6.3) [6]. This generator consists of an evaporation chamber, which is linked to a pump system and a gas inlet. In arc vaporization of graphite rods [18, 19], two graphite rods are kept in close, but not direct contact. A voltage is applied across the two graphite rods by a DC power supply, which is used to maintain the arc discharge between them. A gap of approximately 4 mm is determined to attain maximum brightness of the plasma. The carbon soot generated in the arc is condensed onto a water-cooled stainless steel cylinder. The buckyballs are subsequently obtained by extracting the crude soot with organic solvents, such as toluene. This technique allows an efficient evaporation of carbon, and a very high yield [20].

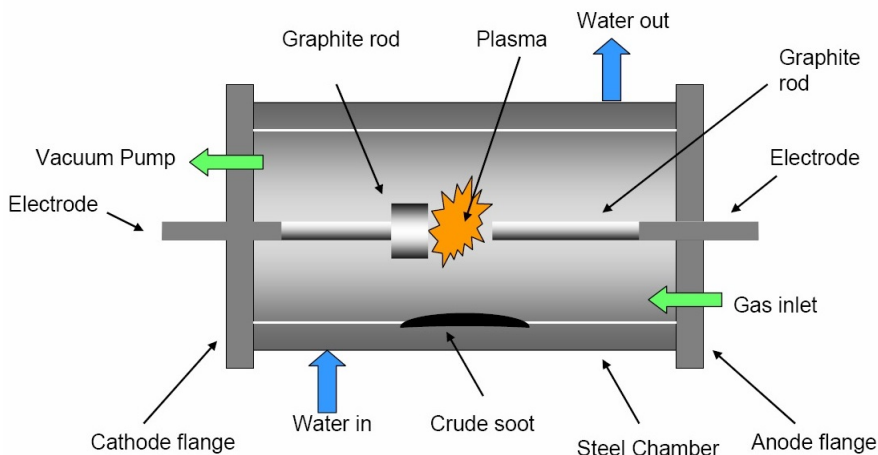


Figure 6.3: Apparatus used to produce fullerenes by arc vaporization of graphite rods [6]

6.2 Geometry and Electronic Properties of Fullerenes

6.2.1 Electronic Properties of Hollow Cage Fullerenes

Buckminsterfullerenes are carbon clusters containing an even number of carbon atoms in the form of an empty ball. The cage is made by pentagonal and hexagonal rings and they are defined by C_n , where n indicates the number of carbon atoms. Buckminsterfullerene C_{60} is the most plentiful fullerene and I_h is the most stable C_{60} isomer. D_{5h} is the next stable isomer for C_{70} . Increasing the number of carbons results in increasing the number of isomers, C_{60} , C_{70} and C_{76} have one isomer whereas C_{78} has five and seven for C_{80} and so on.

Theoretical calculations showed that the *LUMO* and *LUMO* + 1 levels of C_{60} are triply degenerate molecular orbitals. Thus, C_{60} is predicted to be electronegative, i.e. it is able to accept up to six electrons [21–23].

6.2.2 Electronic Properties of Trimetallic Nitride Endohedral Metallofullerenes

C_{80} has seven isomers, which have the following point group symmetry $I_h, D_3, D_2, D_{5h}, D_{5d}$ and two C_{2v} . However, many authors refer to them only as a particular nomenclature of letters [24]. Out of all these isomers, only two have been prepared and characterized as pristine structures: these are D_2 [25] and D_{5d} [26] (See Figure 6.4).

Based on the LUMO-HOMO gap study and ^{13}C NMR analysis of the C_{80} fullerene [27, 28], the D_2 isomer is the most stable of the 7 possible isomers. However, theoretical calculations and NMR analysis, suggest that the least stable isomer I_h turns out to be the most favorable structure when one or more metallic atoms are encapsulated inside the fullerene cage (Figure 6.5).

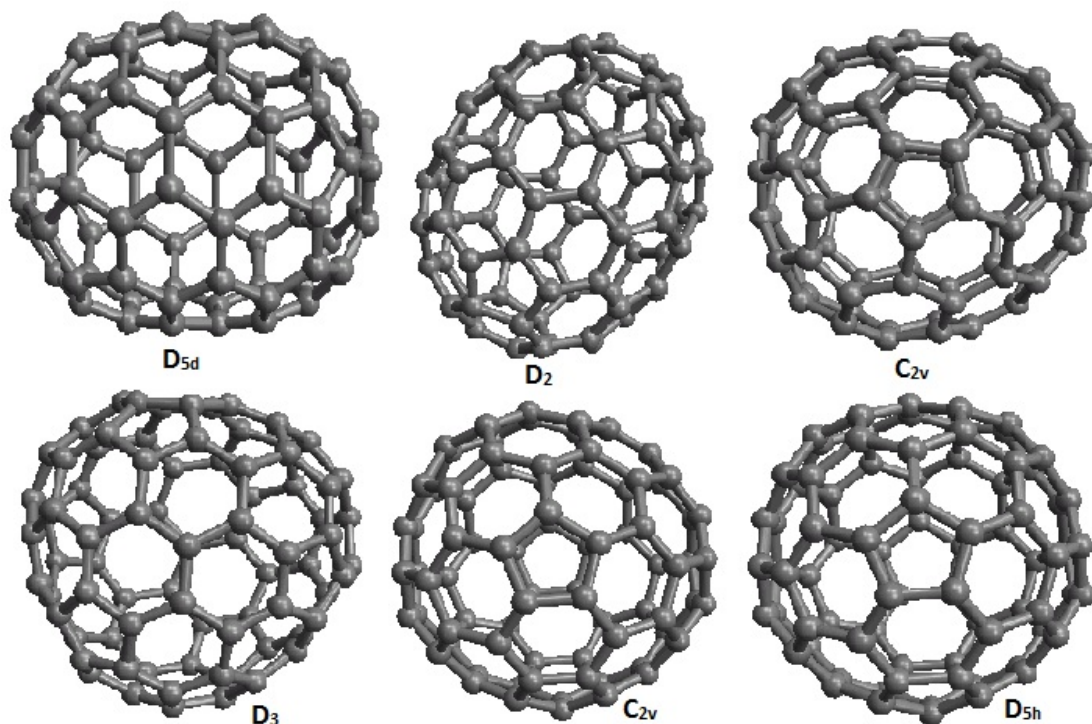


Figure 6.4: Six isomers of C_{80}

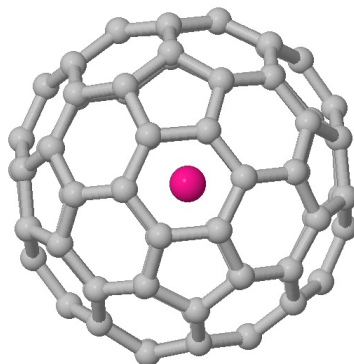


Figure 6.5: An example of stable isomer $Gd@C_{82}$

The explanation for that is the charge is transferred from the internal metal atoms to the cage, making the whole structure more stable. The I_h isomer has only two electrons in the four-fold degenerate *HOMOs*, so it can easily accept six more electrons from the metallic atoms to compose a stable closed shell electronic structure with a large HOMO-LUMO gap. The electronic structure can be described as $(M^{3+})_2C_{80}$ (M =metallic atom) [27].

The metallofullerene family, $Sc_{3-n}M_nN@C_m$ ($M = Y, Sc$ and *lanthanides*, $n =$

0–3, $m = 68, 78, 80$) is produced in relatively high yields by the TNT method [15]. $Sc_3N@C_{80}$ is a representative member of this family and its yield even exceeds the empty-cage C_{84} . $Sc_3N@C_{80}$ has been thoroughly studied by many researchers around the world theoretically, and experimentally by ^{13}C , NMR and X-ray diffraction. It is widely accepted that the charge distribution in $(Sc_3N)^{6+}@C_k$ metallofullerenes may be formally described as $(Sc_3N)^{6+}@C_k^{6-}$. Many theoretical calculations on $Sc_3N@C_{80}$ have proposed that the inorganic part Sc_3N transfers six electrons to the cage, which resulting in a closed shell electronic structure which is described as $(Sc_3N)^{6+}@C_{80}^{6-}$ [29].

The C^{13} NMR spectrum of $Sc_3N@C_{80}$ shows only two lines with an intensity ratio of 3:1. The $ScNMR$ spectrum displays a single symmetric line. The information from NMR experiments indicated the Sc_3N^{6+} is not fixed inside the C_{80} Cage (this point is going to be discussed in more details later).

The positive charges on scandium are very effective for electrostatic attractive interaction with the negatively charged nitrogen and carbon cage. In order to avoid severe electrostatic repulsions between the scandium atoms, the Sc_3N prefers to adopt a planar shape in $Sc_3N@C_{80}$ in order to increase Sc-Sc distance [30].

6.3 Applications of Fullerenes and Endohedral Fullerenes

Endohedral metallofullerenes have attracted a wide interest, due to their functional characteristics and potential applications in many areas of research, for instance, biomedical science and nanomaterials [31]. In past years, metallofullerene-doped nanotubes ('peapods') have also attracted experimental attention due to their structural and electronic properties [32–34] and have been proposed as a possible self-assembled quantum computing architecture. Additionally, recent experimental studies of $Gd@C_{82}$ in single-walled carbon nanotube ($(Gd@C_{82})@SWNT$) peapods have shown novel transport behavior [35].

One of the attractive properties of fullerenes intrinsic to their closed-cage structure is the possibility of using them as robust containers for other species. A range of bare, exohedral, and endohedral fullerene derivatives have been assessed for the ability to achieve an increased V_{OC} (Voltage open circuit) in polymer heterojunction solar cells [36].

6.4 Experimental measurements of single-molecule conductance and thermopower

The following work was carried out by myself and in collaboration with the group of Professor Nicols Agrat (Departamento de Física de la Materia Condensada, Universidad Autónoma de Madrid, Madrid, Spain). I will start with a brief description of the STM method, and then I will present our experimental work on C_{60} and $Sc_3N@C_{80}$. I will then show the theoretical calculations. The results presented here were published in the following paper:

”Rincón-García, Laura, Ali K. Ismael, Charalambos Evangelidis, Iain Grace, Gabino Rubio-Bollinger, Kyriakos Porfyrakis, Nicols Agrat, and Colin J. Lambert. ”Molecular design and control of fullerene-based bi-thermoelectric materials.” *Nature materials*, Vol.15, Issue3, P254 (2015)”.

6.5 Scanning Tunneling Microscopy (STM)

The Nobel Prize in physics was given to Binnig and Rohrer in 1986 for their invention of the scanning tunneling microscope (STM) [37], where a voltage difference is applied between a sharp tip and flat surface separated by a vacuum barrier. Quantum theory predicts electrons can tunnel through this classically forbidden vacuum region between sample and tip, yielding a tunneling current which is sensitive to the tip-sample separation as well as the electronic properties of the sample. STM has been used for many purposes, such as studying atomic and electronic

structure of conductive surfaces, the dispersion relation between metallic surface states [38], and probing the electronic structure of highly correlated materials like high-TC superconductors [39]. STM tip can be used to manipulate the positions of atoms and molecules on conductive surfaces [40]. STM has been used to determine the vibrational [41] and magnetic [42] structure of several systems at the atomic scale and there have been many other useful uses of STM.

6.6 Basic Principle of Scanning Tunneling Microscopy

When a sharp atomic scale metal tip is brought into close proximity to the sample of interest, a small voltage V_b between the tip and the sample, causes electrons to tunnel between the sample and the tip. The exponential decay of the wavefunctions (tip and sample) into the vacuum gap requires the distance between them to be roughly 10 \AA so that there is a sufficient overlap to measure a tunneling current I in the range of 1 nA (for $V_b = 1 \text{ V}$).

In this section I am going to give a brief description of the STM used in this study. Figure 6.6 illustrates the set up of the STM. A sharp metallic tip that is typically made of Au (but can be a number of different metals) is fitted onto a piezoelectric transducer. The tip is brought close to a conductive sample using coarse-motion piezoelectric motors.

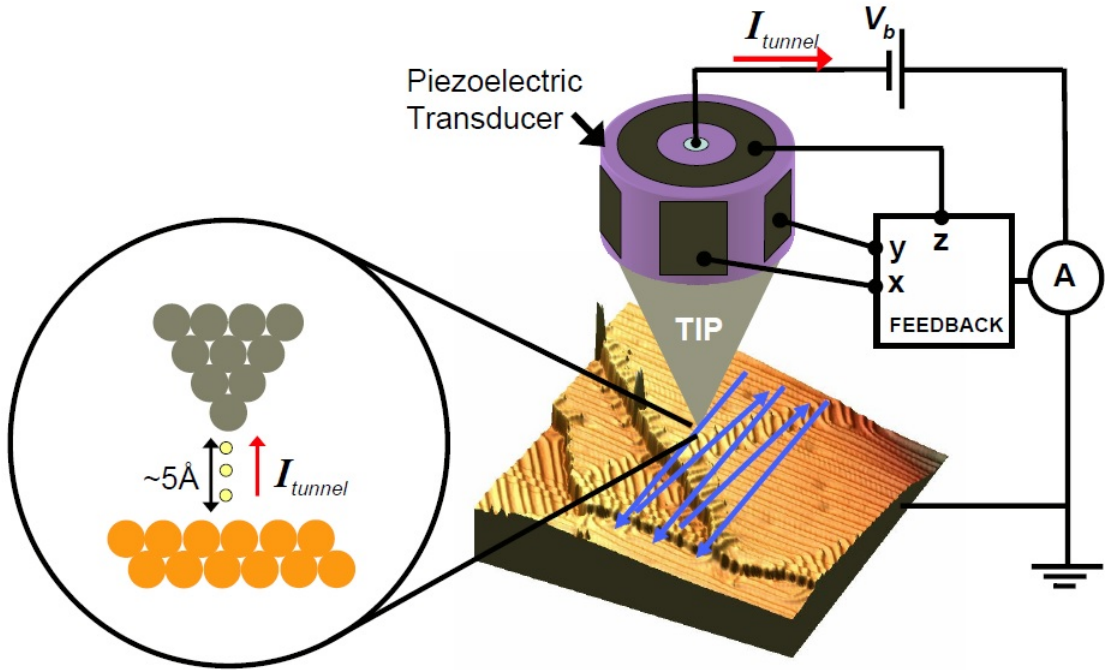


Figure 6.6: Diagram of a STM tip scanning an Au(111) surface. The Au(111) surface is revealed to have a *herringbone* reconstruction pattern as well as atomic step edges [43]

A bias V_b is applied between the sample and the tip and the tip is slowly brought closer to the sample by applying a voltage across the z -axis of the piezoelectric transducer. The current passing through the tip I is continuously monitored, and once it reaches a certain setpoint value (typically a fraction of a nA) the tip is held at a constant height above the surface. The absolute value of the tip height is never known for sure, but it is typically estimated to be $\sim 5\text{\AA}$ above the surface for a current of a fraction of a nA . A topographic image of the surface, can be produced by raster scanning the STM tip back and forth across the surface via application of x and y -axis biases to the piezoelectric transducer. The tip voltage is kept constant and the current is continuously monitored.

$$I \sim \exp[-2(\lambda^2 + k^2)^{\frac{1}{2}}|z|] \quad (6.1)$$

where λ is decay rate in vacuum ($\lambda^2 = \sqrt{2m\bar{\Phi}/\hbar}$), $\bar{\Phi}$ is the average value of the work functions of the tip and sample, k -vector and z tip-surface distance.

The current has a strong exponential dependence on the distance from the tip to

the surface, as shown in equation (6.1), and this dependence allows for a feedback circuit to detect minute changes in the tip height and apply a corrected z-bias to the transducer to bring the STM tip back to the correct height. Figure 6.7 shows example for a topographic image. This kind of image shows that the STM can detect sub- \AA height changes in the surface, thus revealing the topographic structure produced by single atoms.

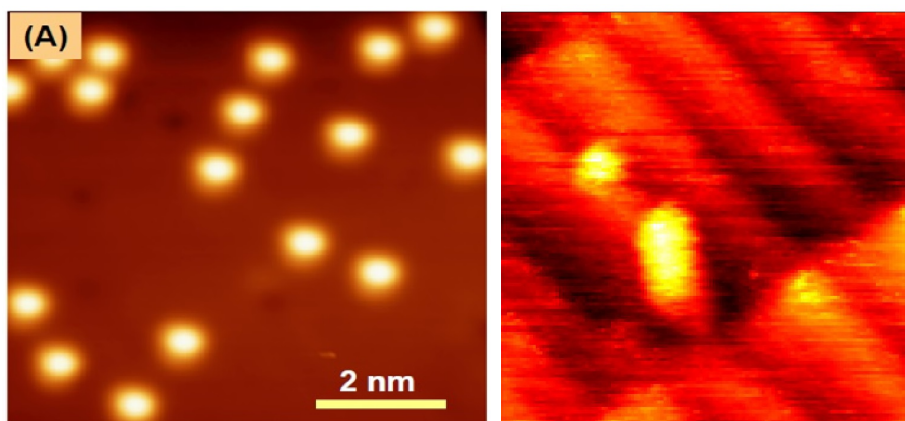


Figure 6.7: Example of topographic images, left image at low temperature

6.7 Experimental Method (STM)

One of the main aims of this thesis is to theoretically model experimental conductance measurements on molecular junctions. What follows is a brief introduction to the techniques used in these types of experiment.

6.7.1 Substrate preparation, experimental setup and technique

Endohedral fullerenes are deposited using the drop casting technique from a very dilute ($10^{-7} - 10^{-8}M$) 1,2,4-trichlorobenzene solution. Specifically, a drop of the solution is left on an annealed gold surface for about 3 minutes, and then is blown off with dry nitrogen and allowed to dry overnight. Once the sample is dry, we mount it on a homebuilt STM and let it stabilize for about one hour in order to

minimize the thermal drift. Using this procedure we are able to deposit isolated molecules both on terraces and step edges and forming small islands, as shown in Fig. 6.8b-d. The molecules at the steps are generally more stable under scanning.

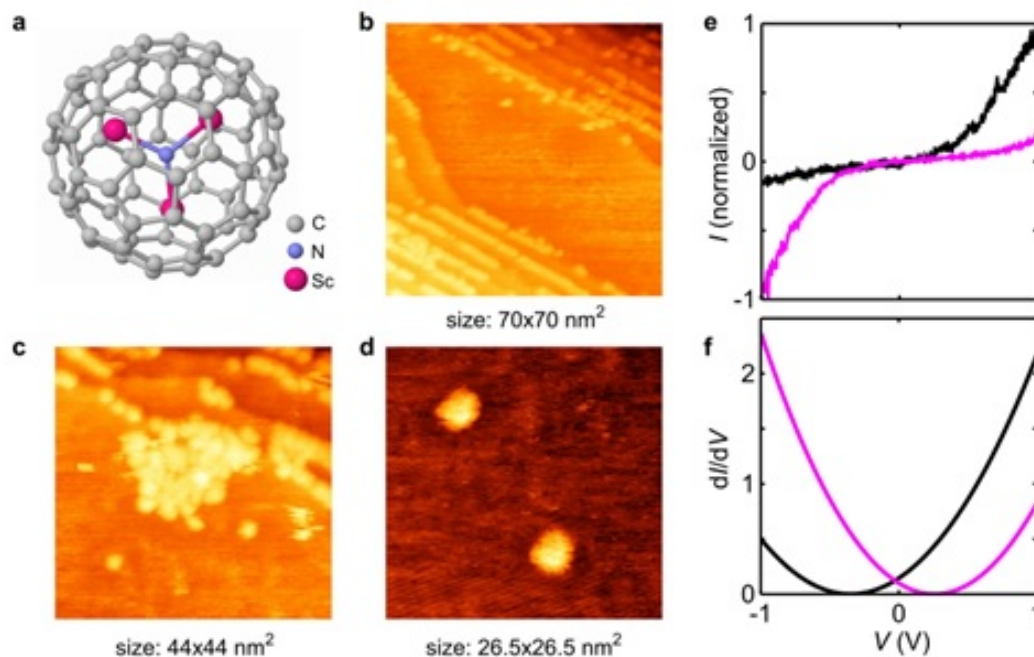


Figure 6.8: Scanning tunnelling microscope images and tunnelling spectroscopy. a, Schematic of the endohedral fullerene $Sc_3N@C_{80}$ used in this work; notice the Sc_3N in the centre of the fullerene cage. b-d STM images of the molecules on atomically flat (111) Au surfaces showing preferential adsorption at step edges (b), islands (c) and isolated molecules (d). e,f IV characteristics (e) and differential conductance (f) in tunnelling regime on two different molecules, presenting opposite rectifying behaviour.

In order to measure the thermopower of the molecular junctions, we have modified our STM setup by adding a surface mount $1 \text{ k}\Omega$ resistor which acts as a heater to the tip holder while the substrate was maintained at room temperature. Two thermocouples connected to the tip and sample holders were used to monitor the resulting temperature difference, which was set to approximately 40 K in the herein reported experiments; the sample is maintained approximately at 298 K (room temperature). We found that the temperature stabilized in about 15-30 minutes and the thermal drift increased, making it necessary to use fast imaging to locate the isolated molecules. The thermopower of molecular junctions is measured

during the approach and the retraction of the STM tip to the molecule as described in Fig.6.9.

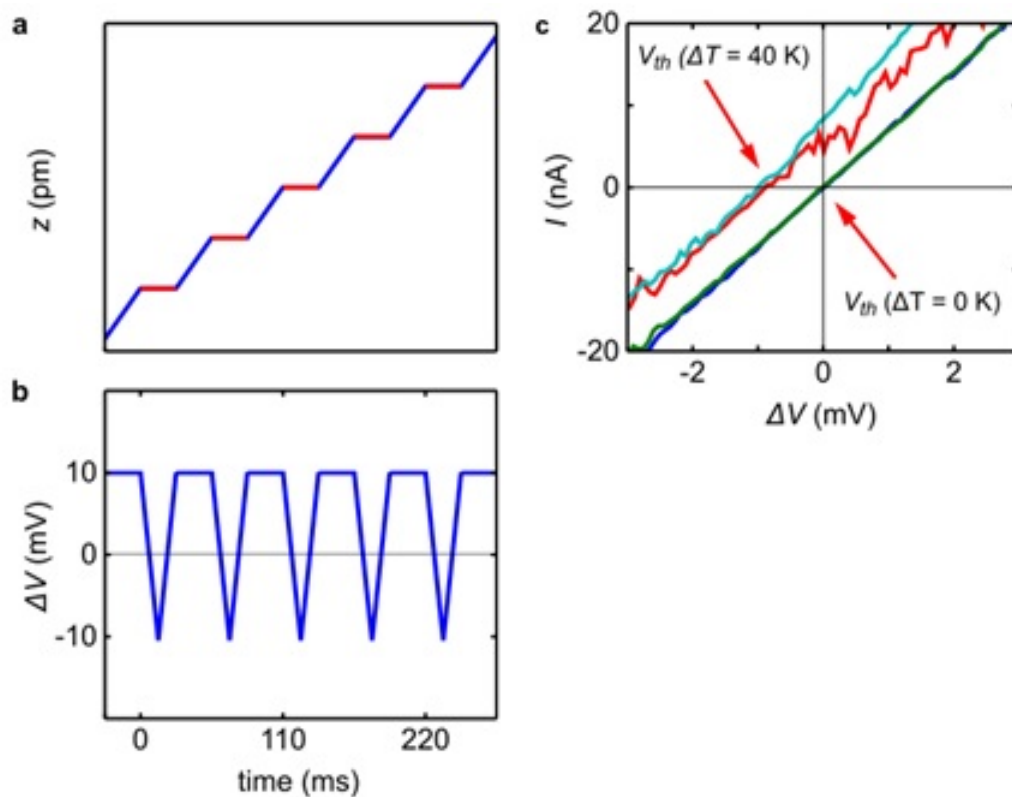


Figure 6.9: Technique for the simultaneous measurement of conductance and thermopower. *a, b*, Tip displacement z and applied bias voltage ΔV at the molecular junction, respectively, as a function of time. The bias voltage is maintained at a fixed value ΔV_0 during the tip motion (in blue in *a*) and every few picometers it is swept between $\pm\Delta V_0$ while the tip is stationary (in red in *a*). In the experiments, the bias voltage ΔV_0 was set to 6–10 mV and the tip was stopped every 15 – 25 pm. In each approaching-separating cycle, 50 – 100 $I - V$ traces are acquired. *c*, Experimental $I - V$ curves showing the voltage offset due to the temperature difference.

6.7.2 Thermal circuit

By heating the tip we not only establish a temperature difference between the tip and the substrate but also a temperature gradient across the tip-connecting lead, which gives rise to an additional thermoelectric voltage. The equivalent circuit for measuring the thermopower is shown in Fig.6.10. Considering the equivalent

circuit, we can write (6.2)

$$\frac{I}{G} = V_{bias} - S(T_h - T_c) - S_{lead}(T_c - T_h) = V_{bias} - S\Delta T + S_{lead}\Delta T \quad (6.2)$$

where V_{bias} is the bias voltage, S is the thermopower of the junction, S_{lead} is the thermopower of the *tip – connecting* lead, T_c is the temperature of the substrate and $T_h = T_c + \Delta T$ is the temperature of the tip. The *tip – connecting* lead is a copper wire, so $S_{lead} = S_{Cu} = 1.83\mu V/K$ [44]. From equation (6.2) and for $I = 0$, the temperature-dependent voltage offset V_{th} of the $I - V$ curve is given by

$$V_{th} = S\Delta T - S_{lead}\Delta = (S - S_{lead})\Delta \quad (6.3)$$

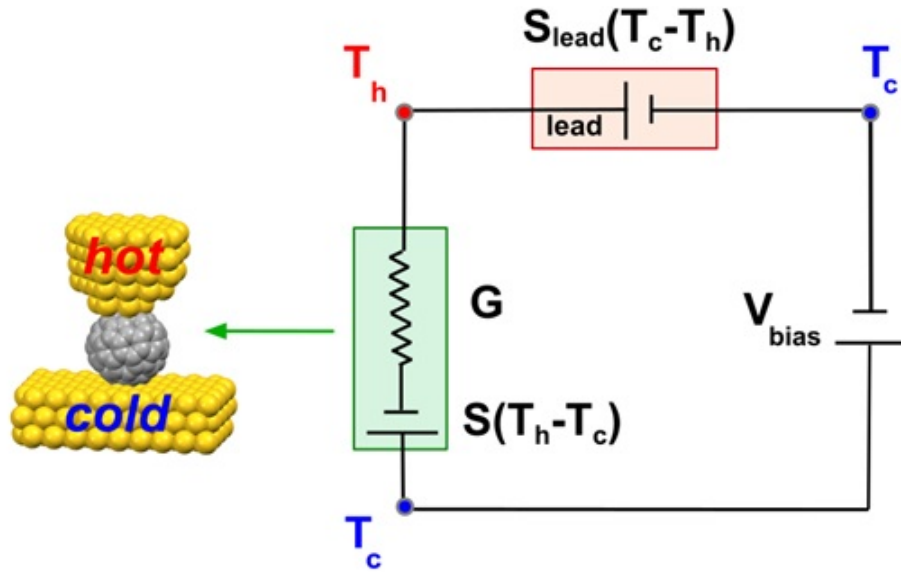


Figure 6.10: Equivalent thermal circuit of the setup for the determination of the thermopower. The substrate and body of the *STM* are at ambient temperature T_c while the tip is heated to a temperature $T_h = T_c + \Delta T$ above ambient temperature. S is the thermopower of the molecular junction and S_{lead} is the thermopower of the *tip – connecting* lead. V_{bias} is the bias voltage applied to the junction.

6.8 Experimental results

Figure 6.11a-b show examples of conductance G (in blue) and thermopower S (in green) curves measured on two different junctions while the tip approaches to touch the $Sc_3N@C_{80}$ molecule. It was found that the conductance of $Sc_3N@C_{80}$ behaves similarly to the case of C_{60} junctions with a jump-to-contact signalling the first-contact as the tip atoms touch the molecule. Typical values for the first-contact conductance are smaller by a factor of three when compared to C_{60} (as shown in Fig. 6.11d).

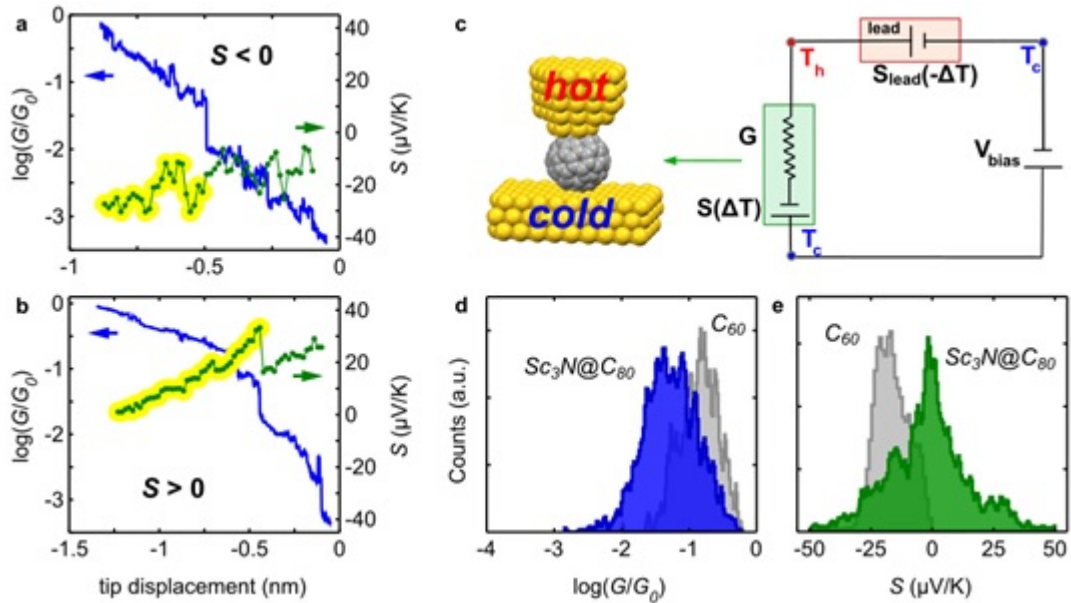


Figure 6.11: Thermopower and conductance simultaneous measurements. a,b, Conductance, G (blue), and thermopower, S (green), simultaneously acquired while approaching individual $Sc_3N@C_{80}$ molecules. For the molecule in a, the thermopower is always negative, while for that one in b, it is always positive. In these measurements the temperature difference was $\Delta T \simeq 40\text{K}$. $G_o = (2e^2)/h$, where e is the electron charge, and h is Plancks constant, is the conductance quantum. The portion of the thermopower trace highlighted in yellow corresponds to molecular contact with the tip. c, Schematic representation of the experimental setup. The tip is heated to a temperature T_h above ambient temperature T_c , while the substrate is maintained at T_c . d,e, Conductance G and thermopower S at first-contact histograms of $Sc_3N@C_{80}$ (in blue and green, respectively) compared to C_{60} (in grey). For the $Sc_3N@C_{80}$ histograms, the mean conductance value is $\bar{G} = 0.05G_o$ and the mean thermopower is $\bar{S} = -2\mu\text{V/K}$.

The thermopower at first-contact of $Sc_3N@C_{80}$ molecules, in contrast to C_{60} , can be positive, negative, or close to zero depending on the selected molecule (Fig.

6.11a-b), resulting in a broad histogram centred around zero, as shown in Fig. 6.11e. The next step is to investigate the variation of thermopower as the tip advances after the first contact, compressing the $Sc_3N@C_{80}$ molecule. The tip was positioned on a selected isolated molecule and performed small amplitude ($< 0.5nm$) compression (approach-retraction) cycles, always maintaining contact with the molecule. In these cycles a variable pressure is exerted on the molecule by the STM tip.

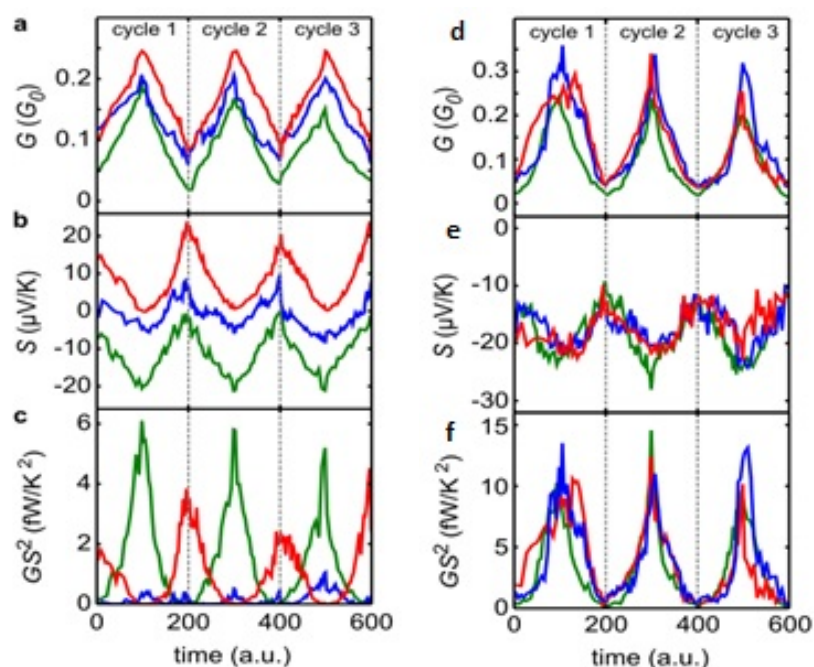


Figure 6.12: Effect of pressure on $Sc_3N@C_{80}$ molecular junctions. a-c, Periodical variations of the conductance G , thermopower S and power factor GS^2 , respectively, as the STM tip advances and retracts during three cycles. Each half cycle corresponds to less than 0.5 nm . Each colour corresponds to a different molecule. d-f, the same effect of pressure but on C_{60}

In Fig.6.12a-b, we present the simultaneous variations of G and S measured during three cycles for three different molecules. The periodic nature of these curves indicates that, in response to the pressure, the junction, i.e., the molecule and the gold electrodes, deforms elastically. Larger amplitude ($> 0.5nm$) cycles destroy this periodicity indicating the onset of plastic deformation (atomic rearrangements) in the gold electrodes [45]. Taking into account previous results

for gold contacts [46] and the fact that fullerene molecules are much stiffer than gold [47], we can safely assume that most of the elastic deformation corresponds to the electrodes and that the maximum pressure at the junction during our measurements is about 4 GPa [45].

The traces shown in Fig. 6.12a-c correspond to three molecules with different behaviours: the red traces correspond to a molecule which showed large positive thermopower at first contact (molecule 1); the blue traces, to a molecule with small positive thermopower (molecule 2); and the green traces, to a molecule with almost zero thermopower (molecule 3).

We observe that for all molecules both the conductance and thermopower vary monotonically with pressure: the conductance increases and the thermopower decreases, becoming more negative, as the tip presses the molecule. This behaviour of the conductance is to be expected, since pressing will result in an increased coupling and consequently in a larger conductance. However, the behaviour of the thermopower is most unusual: very large variations are observed and even a change in sign for molecule 2 (bi-thermoelectric). This extreme sensitivity of thermopower of molecular junctions to pressure had never been reported and has a marked effect on the power factor, GS^2 , as shown in Fig. 6.12c. For molecule 1, the power factor decreases with compression, while for molecule 2, it increases reaching values of around 5 fW/K^2 . In contrast, for molecule 3, GS^2 remains small during the whole cycle.

For C_{60} Fig. 6.12d-f the conductance is higher comparing $Sc_3N@C_{80}$, whereas the thermopower is always negative and this is due to C_{60} has no resonance in its transmission curve, as we will see in theory part (see Fig 6.17). Power factor is roughly double than $Sc_3N@C_{80}$.

6.8.1 Pressure variation with tip displacement of the conductance, the thermopower, and the power factor of $Sc_3N@C_{80}$ junctions

Figure 6.13 left panel shows the effect of pressing $Sc_3N@C_{80}$ by the tip, and the right panel is the theoretical modeling for the same process which shows the same trend. The following section provides details of the theoretical modeling.

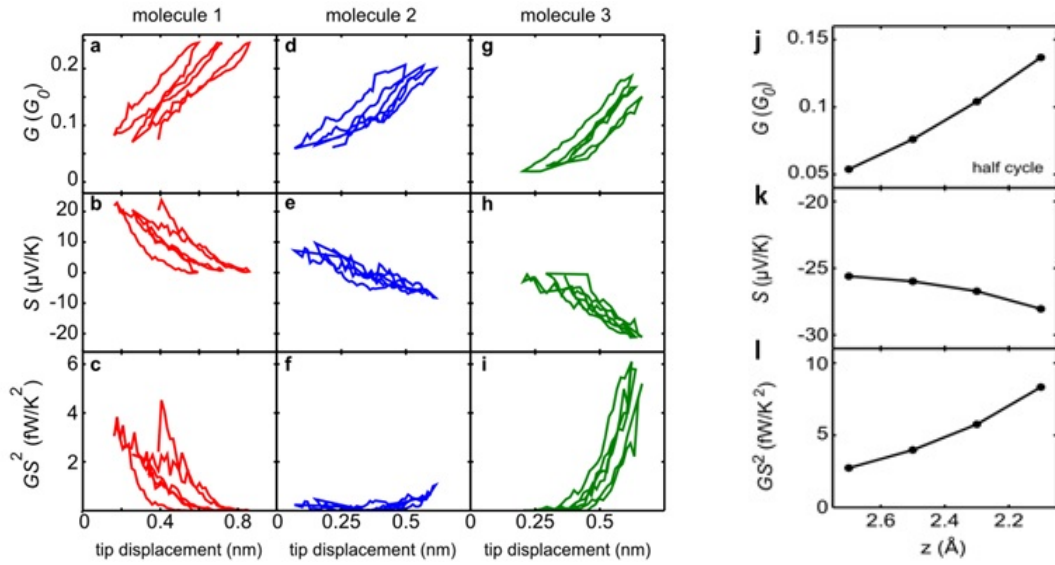


Figure 6.13: Effect of pressure on $Sc_3N@C_{80}$ junctions as a function of tip displacement. Periodical variations of the conductance G (a,d,g), the thermopower S (b,e,h), and power factor GS^2 (c,f,i) as a function of the tip displacement. This is the same data as in Fig.6.12a-c and the colours correspond to same three molecules detailed in the main text (1, 2 and 3). For molecule 1 (red), compressing the molecule results in S varying from $+20\mu V/K$ to almost $0\mu V/K$; for molecule 2 (blue), S varies from $+10\mu V/K$ to $-5\mu V/K$; and for molecule 3 (green), S varies from approximately $0\mu V/K$ to $-20\mu V/K$. Each half cycle corresponds to less than 0.5 nm. This representation is directly equivalent to the plot of the theoretical calculations j-l.

6.9 Theoretical modeling of thermopower switching

Here, I calculate the parameters G , S and P for the molecules C_{60} and $Sc_3N@C_{80}$. Firstly, I need to know whether Sc_3N rotates inside C_{80} cage and what is the binding energy of $Sc_3N@C_{80}$ on gold. Then I will use this information to initiate calculations the G , S and P .

6.10 Does Sc_3N rotate inside the cage?

Some experimental studies have proposed that the metallic part Sc_3N cluster rotates rapidly inside the cage (see Figure 6.14). NMR experiment data suggest that the Sc_3N^{6+} rotates inside the negatively charged cage [15], the electrostatic potential map of C_{80}^{6-} showed almost concentric circles with no clear minima [32]. This indicates that the encapsulated metal cluster Sc_3N^{6+} is not fixed at specific internal bonding sites but can freely rotate inside the C_{80} Cage (Figure 6.14b), as found for $La_2@C_{80}$ [48].

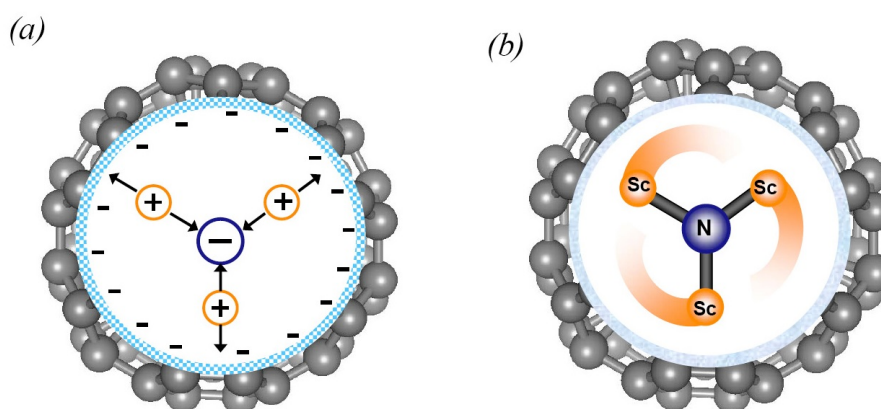


Figure 6.14: (a) Charge transfer model for $Sc_3N@C_{80}$ (b) Rapid circular motion of the Sc_3N cluster inside the $I_h C_{80}$ cage.

To test whether the Sc_3N^{6+} rotates inside the cage when the $Sc_3N@C_{80}$ is attached to gold electrodes, the optimum geometry of the isolated molecule $Sc_3N@C_{80}$ was

calculated using DFT, with all forces on atoms relaxed to a tolerance of 0.01 eV/Å. A double-zeta-plus-polarization (DZP) basis set, with norm-conserving pseudopotentials was employed and the Hamiltonian and overlap matrices were calculated on a real space grid defined by a plane wave cutoff of 200 Ry. After calculating the optimum geometry of the molecular wire, it was attached to gold electrodes.

I calculated the energy barrier to rotate the metallic part Sc_3N inside the cage using the BSSE method (2.8). Figure 6.15, shows the resulting energy versus rotation angle and demonstrates that the energy barrier is more than 10 times bigger than 25 meV and therefore the Sc_3N is locked in position at room temperature.

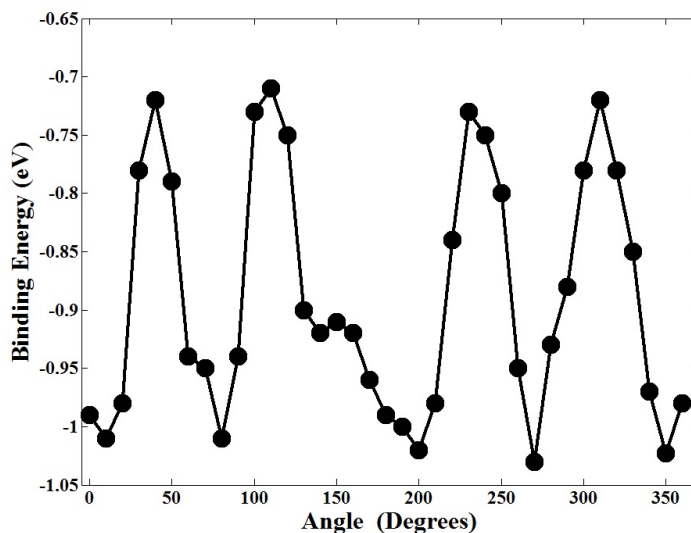


Figure 6.15: Binding energy as a function of rotation of Sc_3N within the fixed $I_h - C_{80}$ cage.

6.11 Binding energy of $Sc_3N@C_{80}$ on gold

To calculate the optimum binding distance for a $Sc_3N@C_{80}$ molecule between two gold (111) surfaces I use *DFT* and the counterpoise method, which removes basis set superposition errors (*BSSE*) (See 2.8). The binding distance z is defined as the distance between the gold surface and the C_{80} cage at the closest point. Here the $Sc_3N@C_{80}$ molecule is defined as monomer A and the gold electrodes as monomer B.

Since there are many orientations for the $Sc_3N@C_{80}$ to orientate itself with respect to a gold substrate, I selected the most favourable two configurations and calculated their binding energy. The angle θ defines the orientation of the Sc_3N molecule within the cage with respect to the gold surface. $\theta = 0^\circ$ corresponds to the plane of this molecule being perpendicular to the gold surface (Fig.6.16 top left) and $\theta = 90^\circ$ (Fig.6.16 top right) is when the plane of the Sc_3N molecule lies parallel to the gold surface. Figure 6.16 shows that the highest binding energy when the metallic part is parallel to the face of the electrode.

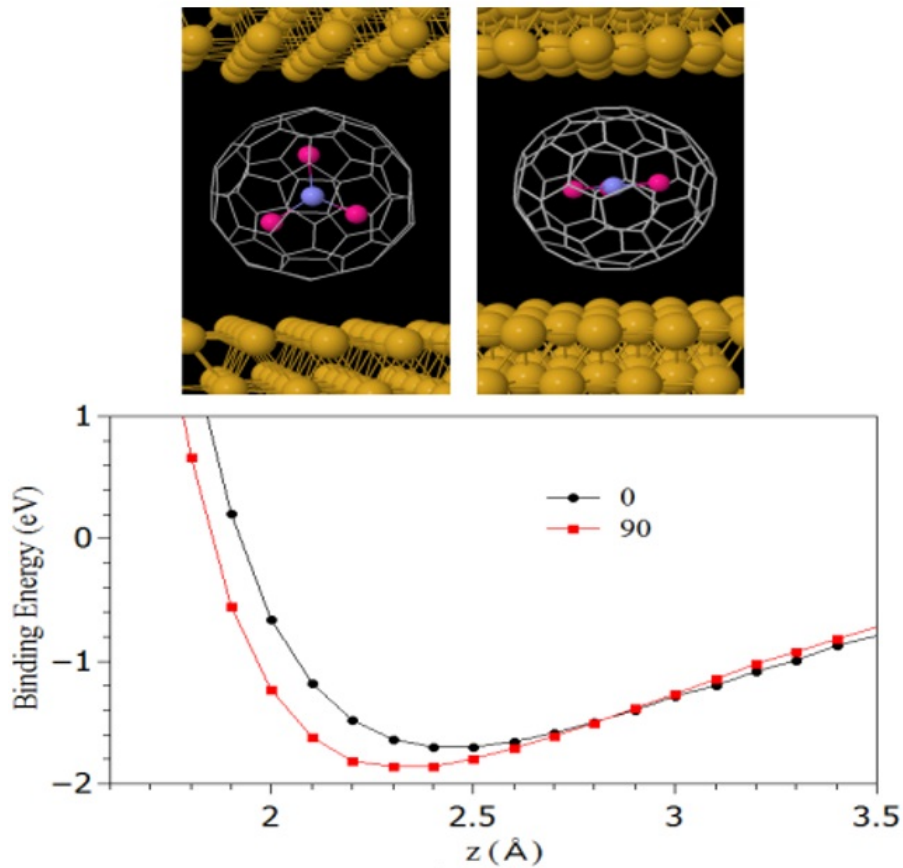


Figure 6.16: $Sc_3N@C_{80}$ on a gold surface. Top panels: Orientation of the $Sc_3N@C_{80}$ molecule with respect to the gold leads corresponds to the defined angle (left) $\theta = 0^\circ$ and (right) $\theta = 90^\circ$. Lower panel: Binding energy of $Sc_3N@C_{80}$ to gold as a function of molecule-contact distance. The equilibrium distance is found to be approximately 2.3 Å from the minimization of the binding energy.

The ground state energy of the total system is calculated using SIESTA and is denoted E_{AB}^{AB} , with the parameters defined in section 2.8. Here the gold leads con-

sist of 3 layers of (111) gold consisting 25 atoms. The energy of each monomer is then calculated in a fixed basis, which is achieved through the use of ghost atoms in *SIESTA*. Hence the energy of the individual $Sc_3N@C_{80}$ in the presence of the fixed basis is defined as E_A^{AB} and for the gold is E_B^{AB} . The binding energy is then calculated using the following equation (6.4), (See chapter 2)

$$BindingEnergy = E_{AB}^{AB} - E_A^{AB} - E_B^{AB} \quad (6.4)$$

Figure 6.16 shows that for an orientation $\theta=0^\circ$ the optimum binding distance z is 2.5 \AA and the binding energy is approximately 1.6 eV . For an angle of $\theta=90^\circ$ the value of z is approximately 2.4 \AA and has a binding energy of 1.8 eV .

6.12 Comparison between Fullerenes and Endohedral Fullerenes

As previously mentioned, a fullerene is just a cage of carbon atoms, whereas endohedral fullerene is a cage with a metallic part encapsulated inside the cage. Here, I am going to make a comparison between C_{60} and $Sc_3N@C_{80}$ in terms of their transmission coefficients (Figure 6.17).

The main difference between their transmission curves is the resonance present in the case of the endohedral fullerene close to LUMO. This resonance is due to the metallic part Sc_3N inside the cage, whereas in C_{60} case we can see a smooth HOMO-LUMO gap, as shown in Figure 6.17.

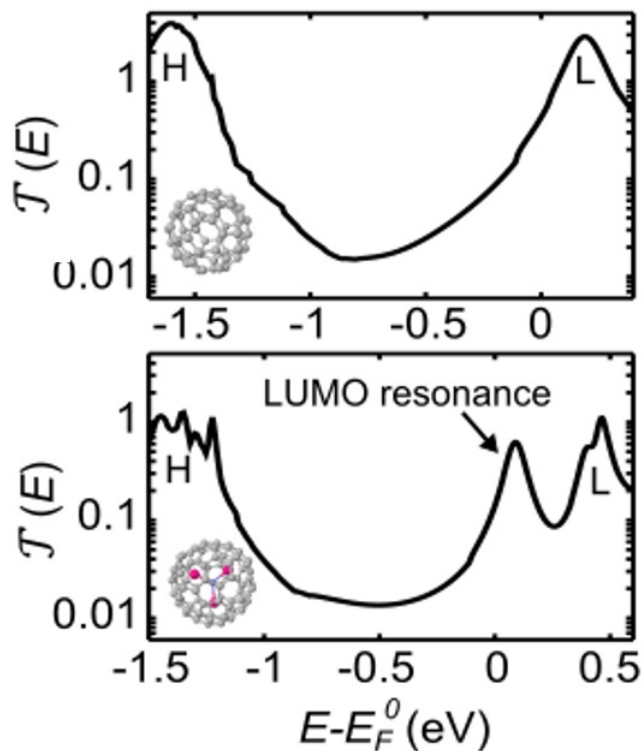


Figure 6.17: Transmission curves, for C_{60} and $Sc_3N@C_{80}$ junctions, respectively. Letters H and L indicate the HOMO and LUMO peaks of the fullerene cages.

6.13 Frontier Orbitals of the $Sc_3N@C_{80}$ Molecule

Extra evidence to support the view that the LUMO resonance of $Sc_3N@C_{80}$ is due to the Sc_3N is found in the frontier of the orbitals. From Figure 6.18, we can see there is no weight on the cage I_h for both LUMO and LUMO+1, whereas it is clear there is a weight on the scandium atoms. In comparison the HOMO orbitals show no weight inside the cage.

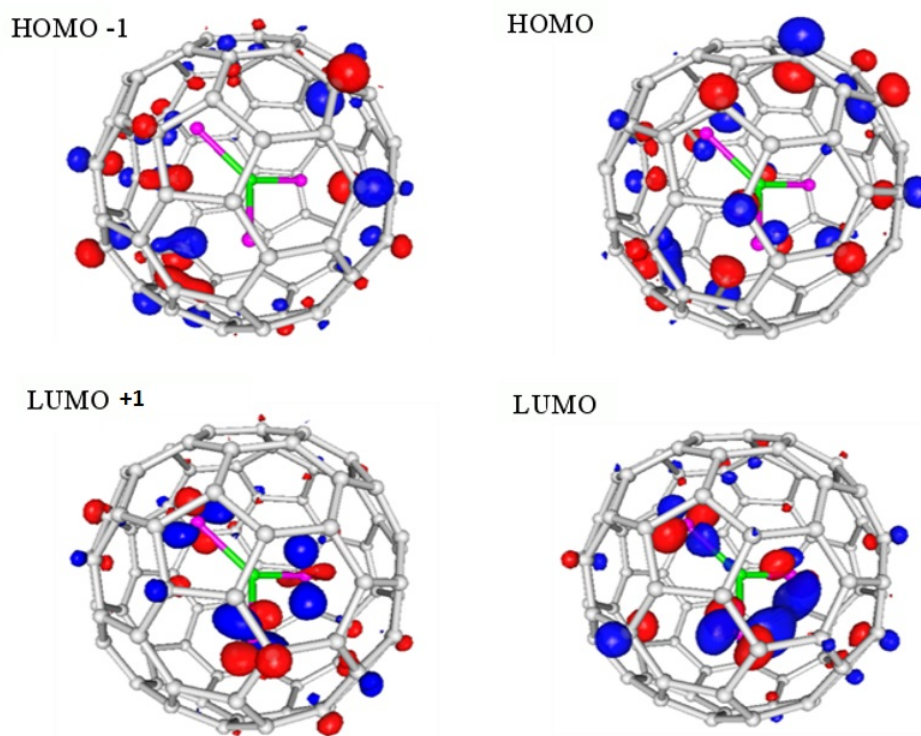


Figure 6.18: Wavefunctions of the *HOMO* – *LUMO* orbitals of the $Sc_3N@C_{80}$ molecule.

6.14 Transmission coefficient as a function of orientation of the $Sc_3N@C_{80}$ molecule

In this part, I am going to focus on the effect of changing the orientation of the endohedral fullerene and the application of external pressure on the fullerene cage. The idea is to cover the two cases, when the scandium atoms have the shortest distance from the gold electrodes ($\theta = 0^\circ$), and the longest distance at $\theta = 90^\circ$ this for rotation. For compression is to see whether $Sc_3N@C_{80}$ is going to deform.

6.14.1 Rotating

Figure 6.19 shows the definition of the orientation angle of the Sc_3N molecule for $\theta = 0^\circ$ and 90° . Figure 6.20 shows the individual transmission coefficients $\mathcal{T}(E)$ for various angles as the molecule is rotated through 180° , for identical tip separations of $z = 2.3 \text{ \AA}$ at each electrode. The DFT-predicted Fermi energy E_F^0 is close to the LUMO resonance and the effect of rotation causes this peak to shift

and broaden. In the case of $\theta = 90^\circ$ the resonance is narrowest and shifted furthest to the left. This is because at this orientation the scandium atoms are furthest from the gold surfaces and as the LUMO is located mainly on these atoms (Fig. 6.18) the coupling to the leads is weakest for this geometry.

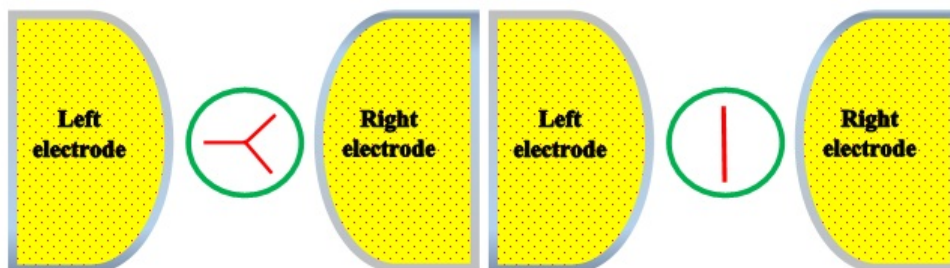


Figure 6.19: Rotation angles θ between 0° and 90° of the $Sc_3N@C_{80}$ molecule with respect to the gold leads.

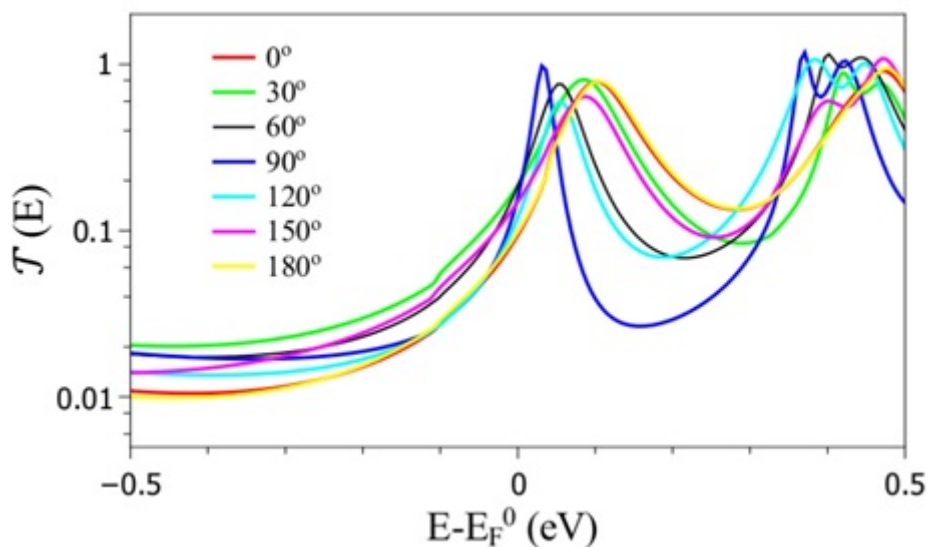


Figure 6.20: Transmission coefficient as a function of orientation. Zero bias transmission coefficient $\mathcal{T}(E)$ versus electron energy E for rotation angles θ between 0° and 180° of the $Sc_3N@C_{80}$ molecule with respect to the gold leads.

6.14.2 Pressing

Figure 6.21 illustrates the pressing of the two molecules C_{60} and $Sc_3N@C_{80}$ in between the electrodes, which is achieved by varying the distance between the electrodes to make tip-molecule separation z decreases from 2.7° to 2.1° . Figure 6.21 shows that C_{60} and $Sc_3N@C_{80}$ barely distort at 2.1° (the shortest z). In these simulations, the gold is not allowed to relax.

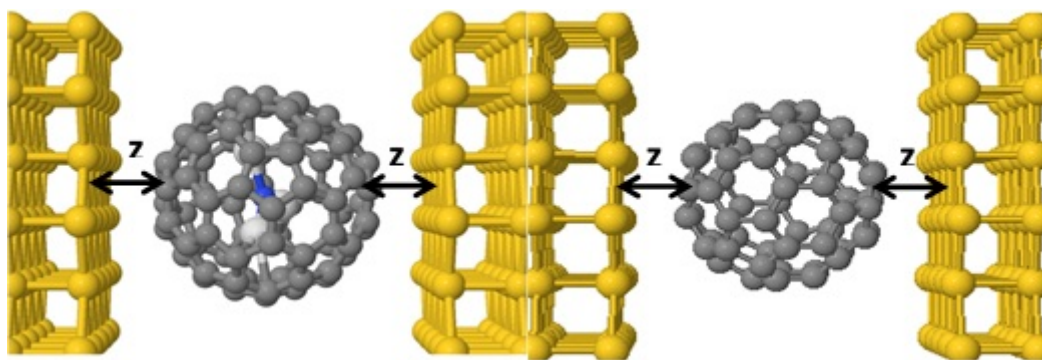


Figure 6.21: Optimized geometries of $Sc_3N@C_{80}$ and C_{60} junctions.

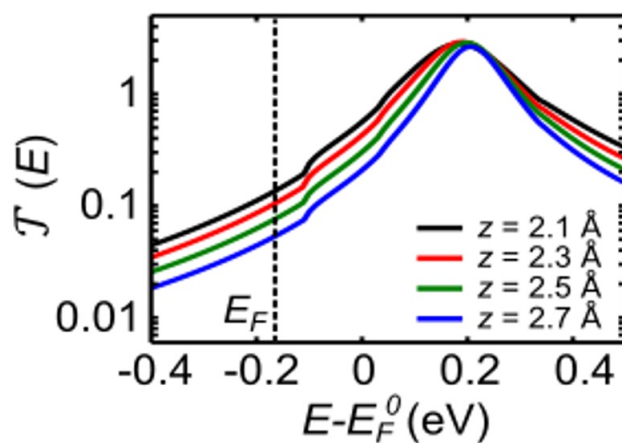


Figure 6.22: Transmission curves, $\mathcal{T}(E)$, for different z (C_{60}). The Fermi level is shifted from the position given by *DFT* and the black dotted line indicates the true Fermi level as explained in the text. In this case, $E_F = E_F^0 - 0.165\text{eV}$, chosen such as to present similar amplitude variations as the experimental curves.

Figure 6.22 shows the effect of pressure on C_{60} molecular junction. From Figure 6.22, we can see the thermopower is always negative, i.e the gradient of $\mathcal{T}(E)$ is positive at E_F .

To elucidate the origin of the bi-thermoelectric effect (change in the sign of S , mentioned in the experimental part, see Fig.6.12b) of the endohedral fullerene junctions I have chosen three different orientations ($\theta = 150^\circ$, $\theta = 57^\circ$, and $\theta = 63^\circ$, for different z , as shown in Figure 6.23

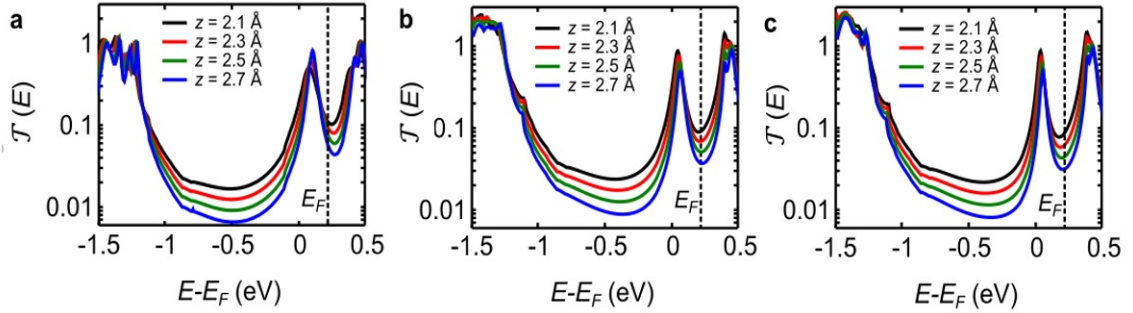


Figure 6.23: Transmission coefficient as a function of orientation and tip separation. Transmission curves, $\mathcal{T}(E)$, for three different orientations ($\theta = 150^\circ$, $\theta = 57^\circ$, and $\theta = 63^\circ$, respectively) and for different z .

Figure 6.24 shows the thermopower S evaluated at room temperature for orientation angles of θ from 0° to 180° and at four different tip separations z from 2.7 ($D=13.6\text{\AA}$) to 2.1 \AA as shown in Fig.6.25

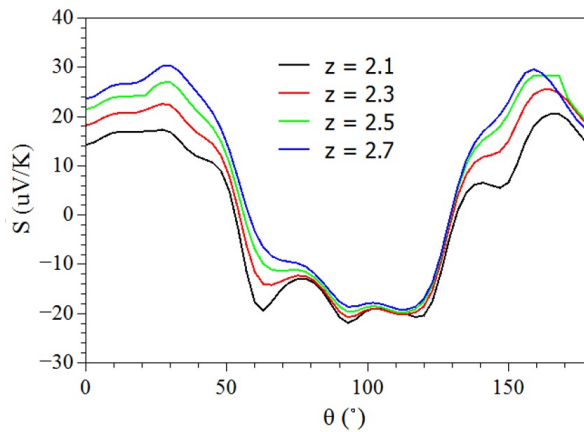


Figure 6.24: Thermopower as a function of orientation and tip separation. Thermopower S versus orientation angle at a value of $E_F = 0.23$ eV, for different tip-substrate distances z .

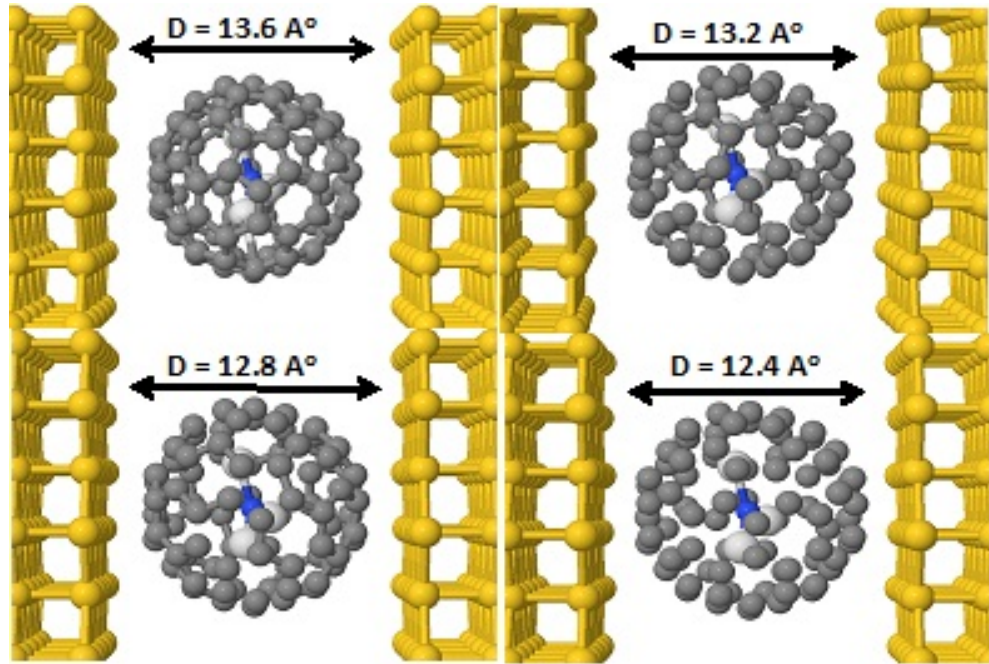


Figure 6.25: Optimized geometries of $Sc_3N@C_{80}$ junctions. Four optimized geometries corresponding to tip-carbon distances of 2.7, 2.5, 2.3 and 2.1 Angstroms. They show that the C_{80} barely distorts over such a range. In these simulations, the gold is not allowed to relax.

In Figure 6.24 the value of the Fermi energy is $E_F = E_F^0 + 0.23eV$, where E_F^0 is the DFT-predicted value of E_F . This value of E_F has been optimized to give the best agreement with the experimental measurements. This plot shows how the behaviour of the thermopower is sensitive to the orientation of the Sc_3N molecule within the cage. At low and high angles, i.e. less than 50° and greater than 130° the thermopower is positive, while between these angles it is negative. As the tip is moved closer to the molecule the value of the thermopower decreases at all angles, and at certain angles such as approximately 60° the sign of S goes from positive to negative. The general pressing causes the thermopower to become more negative occurs at all angles. If we choose three angles i.e $\theta = 150^\circ$, $\theta = 57^\circ$, and $\theta = 63^\circ$ as seen in Figure 6.23, which shows that at three angles we get excellent agreement with the experimental values shown in Figure 6.12.

In conclusion, I have demonstrated a new concept of bi-thermoelectricity, in which the sign and magnitude of the thermopower of a given material can be tuned. This effect was realised by identifying a molecule with a transmission resonance close to the Fermi energy, whose energetic location is sensitive to orientation and pressure. In this chapter, I demonstrated bi-thermoelectricity in $Sc_3N@C_{80}$, but more generally the effect should be present in any material with orientation-dependent and pressure-dependent transmission resonances, which can be caused to pass through the Fermi energy. For the future, if appropriate templating strategies could be implemented, which select appropriate orientations of such molecules, then single-material, nanoscale tandem devices with alternating-sign thermopowers could be realised.

Bibliography

- [1] D. E. Jones, "Hollow molecules", *New Sci* 32: 245, 1966.
- [2] E. Osawa, "Kagaku (Kyoto) 1970, 25, 854", Japanese; *Chem. Abstr* 74, 1970.
- [3] H. W. Kroto, J. R. Heath, S. C. O'Brien, R. F. Curl and R. E. Smalley, "C₆₀: buckminsterfullerene", *Nature* 318, no. 6042: 162-163, 1985.
- [4] F. Arena, F. Bullo, F. Conti, C. Corvaja, M. Maggini, M. Prato and G. Scorrano, "Synthesis and EPR studies of radicals and biradical anions of C₆₀ nitroxide derivatives", *Journal of the American Chemical Society* 119, no.4: 789-795, 1997.
- [5] V. P. Gubskaya, L. Sh. Berezhnaya, A. T. Gubaidullin, I. I. Faingold, R. A. Kotelnikova, N. P. Konovalova, V. I. Morozov, I. A. Litvinov and I. A. Nuretdinov, "Synthesis, structure and biological activity of nitroxide malonate methanofullerenes", *Organic and biomolecular chemistry* 5, no.6: 976-981, 2007.
- [6] W. Kratschmer, "L m LD, FOSTIROPOULOS K. and HUFFMAN DR", *Nature* 347 , 1990.
- [7] S. Holger, "EMS: efficiency measurement system users manual", *Operations Research and Wirtschaftsinformatik*. University of Dortmund, Germany, 2000.
- [8] J. R. Heath, S. C. O'brien, Q. Zhang, Y. Liu, R. F. Curl, F. K. Tittel, and R. E. Smalley, "Lanthanum complexes of spheroidal carbon shells", *Journal of the American Chemical Society* 107, no. 25: 7779-7780, 1985.

- [9] F. D. Weiss, J. L. Elkind, S. C. O'Brien, R. F. Curl and R. E. Smalley, "Photophysics of metal complexes of spheroidal carbon shells", *Journal of the American Chemical Society* 110, no. 13: 4464-4465, 1988.
- [10] Y. Chai, T. Guo, C. Jin, and R. E. Hau, "er, LPF Chibante, J. Fure, L. Wang, JM Alford and RE Smalley", *J. Phys. Chem* 95 : 7564-7568, 1991.
- [11] M. Inakuma and H. Shinohara, "Temperature-Dependent EPR Studies on Isolated Scandium Metallofullerenes: Sc@ C82 (I, II) and Sc@ C84", *The Journal of Physical Chemistry B* 104, no. 32: 7595-7599, 2000.
- [12] S. Liu and S. Sun, "Recent progress in the studies of endohedral metallofullerenes", *Journal of Organometallic Chemistry* 599, no. 1: 74-86, 2000.
- [13] C. -Ru Wang, T. Kai, T. Tomiyama, T. Yoshida, Y. Kobayashi, E. Nishibori, M. Takata, M. Sakata and H. Shinohara, "A scandium carbide endohedral metallofullerene:(Sc₂C₂)@ C84", *Angewandte Chemie International Edition* 40, no. 2: 397-399, 2001.
- [14] C. Shu, T. Cai, L. Xu, T. Zuo, J. Reid, K. C. Dorn and H. W. Gibson, "Manganese (III)-catalyzed free radical reactions on trimetallic nitride endohedral metallofullerenes", *Journal of the American Chemical Society* 129, no. 50: 15710-15717, 2007.
- [15] S. Stevenson, G. Rice, T. Glass, K. Harich, F. Cromer, M. R. Jordan, J. Craft, E. Hadju, R. Bible, M. M. Olmstead, "Small-bandgap endohedral metallofullerenes in high yield and purity", *Nature* 401, no. 6748: 55-57, 1999.
- [16] L. Dunsch and Y. Shangfeng, "Metal nitride cluster fullerenes: their current state and future prospects", *Small* 3, no. 8: 1298-1320, 2007.
- [17] M. M. Olmstead, A. de Bettencourt-Dias, J. C. Duchamp, S. Stevenson, Harry C. Dorn and A. L. Balch, "Isolation and crystallographic characterization of

- ErSc₂N@ C80: an endohedral fullerene which crystallizes with remarkable internal order”, *Journal of the American Chemical Society* 122, no. 49 : 12220-12226, 2000.
- [18] X. Wang, T. Zuo, M. M. Olmstead, J. C. Duchamp, T. E. Glass, F. Cromer, A. L. Balch and H. C. Dorn, ”Preparation and structure of CeSc₂N@ C80: An icosahedral carbon cage enclosing an acentric CeSc₂N unit with buried f electron spin”, *Journal of the American Chemical Society* 128, no. 27 : 8884-8889, 2006.
- [19] N. Chen, Er-Yun Zhang and C.-Ru Wang, ”C80 encaging four different atoms: The synthesis, isolation, and characterizations of ScYErN@ C80”, *The Journal of Physical Chemistry B* 110, no. 27: 13322-13325, 2006.
- [20] K. Fisher, C. Largeau and S. Derenne, ”Can oil shales be used to produce fullerenes?”, *Organic geochemistry* 24, no. 6: 715-723, 1996.
- [21] R. E. Haufler, J. Conceicao, L. P. F. Chibante, Y. Chai, N. E. Byrne, S. Flanagan, M. M. Haley, S. C. O’Brien and C. Pan, ”Efficient production of C60 (buckminsterfullerene), C60H36, and the solvated buckide ion”, *Journal of Physical Chemistry* 94, no. 24: 8634-8636, 1990.
- [22] P. Jakes and D. Klaus-Peter, ”Chemically induced spin transfer to an encased molecular cluster: An EPR study of Sc₃N@C80 radical anions”, *Journal of the American Chemical Society* 123, no. 36: 8854-8855, 2001.
- [23] D. A. Loy and R. A. Assink, ”Synthesis of a fullerene C60-p-xylylene copolymer”, *Journal of the American Chemical Society* 114, no. 10: 3977-3978, 1991.
- [24] A. A. Popov and L. Dunsch, ”Hindered Cluster Rotation and ⁴⁵Sc Hyperfine Splitting Constant in Distonoid Anion Radical Sc₃N@ C80, and Spatial Spin Charge Separation as a General Principle for Anions of Endohedral Fullerenes with Metal-Localized Lowest Unoccupied Molecular Orbitals”, *Journal of the American Chemical Society* 130, no. 52: 17726-17742, 2008.

- [25] C. M. Cardona, B. Elliott and L. Echevoyen, "Unexpected chemical and electrochemical properties of $M_3N@C_{80}$ ($M = Sc, Y, Er$)", *Journal of the American Chemical Society* 128, no. 19: 6480-6485, 2006.
- [26] Z. Slanina, Shyi-Long Lee, F. Uhlk, L. Adamowicz and S. Nagase, "Computing relative stabilities of metallofullerenes by Gibbs energy treatments", *Theoretical Chemistry Accounts* 117, no. 2: 315-322, 2007.
- [27] C. Thilgen, A. Herrmann and F. Diederich, "Die kovalente Chemie der hheren Fullerene: C_{70} und jenseits davon", *Angewandte Chemie* 109, no. 21 (1997): 2362-2374, 1996.
- [28] C. -R. Wang, T. Sugai, T. Kai, T. Tomiyama and H. Shinohara, "Production and isolation of an ellipsoidal C_{80} fullerene", *Chemical Communications* 7: 557-558, 2000.
- [29] K. Kobayashi, N. Shigeru and T. Akasaka, "A theoretical study of C_{80} and $La_2@C_{80}$ ", *Chemical physics letters* 245, no. 2: 230-236, 1995.
- [30] M. M. Olmstead, A. de BettencourtDias, J. C. Duchamp, S. Stevenson, D. Marciu, H. C. Dorn and A. L. Balch, "Isolation and structural characterization of the endohedral fullerene $Sc_3N@C_{78}$ ", *Angewandte Chemie International Edition* 40, no. 7: 1223-1225, 2001.
- [31] K. Kobayashi, Y. Sano and S. J. Nagase, "Small-bandgap endohedral metallofullerenes in high yield and purity", *Comput. Chem* 22: 1353, 2001.
- [32] K. Kobayashi, N. Shigeru and A. Takeshi, "Endohedral dimetallofullerenes $Sc_2@C_{84}$ and $La_2@C_{80}$. Are the metal atoms still inside the fullerece cages?", *Chemical physics letters* 261, no. 4 : 502-506, 1996.
- [33] D. S. Bethune, R. D. Johnson, J. R. Salem, M. S. De Vries and C. S. Yannoni, "Atoms in carbon cages: the structure and properties of endohedral fullerenes", *Nature* 366, no. 6451 (1993): 123-128, 1993.

- [34] X. Liu, T. Pichler, M. Knupfer, M. S. Golden, J. Fink, H. Kataura, Y. Achiba, K. Hirahara and S. Iijima, "Filling factors, structural, and electronic properties of C_{60} molecules in single-wall carbon nanotubes." *Physical Review B* 65, no. 4 :045419, 2002.
- [35] T. Shimada, T. Okazaki, R. Taniguchi, T. Sugai, H. Shinohara, K. Suenaga, Y. Ohno, S. Mizuno, S. Kishimoto, T. Mizutani, "Ambipolar field-effect transistor behavior of $Gd@C_{82}$ metallofullerene peapods", *Applied physics letters* 81, no. 21: 4067-4069 2002.
- [36] J. Lee, H. Kim, S-J. Kahng, G. Kim, Y-W. Son, J. Ihm, H. Kato, "Bandgap modulation of carbon nanotubes by encapsulated metallofullerenes", *Nature* 415, no. 6875: 1005-1008, 2002.
- [37] G. Binnig, H. Rohrer, C. Gerber, and E. Weibel, "Surface Studies by Scanning Tunneling Microscopy", *Physical Review Letters* 49, 57-61, 1982.
- [38] M. F. Crommie, P. C. Lutz, and M. Donald, "Confinement of electrons to quantum corrals on a metal surface", *Science* 262.5131: 218-220, 1993.
- [39] S. H. Pan, E. W. Hudson, K. M. Lang, H. Eisaki, S. Uchida, and J. C. Davis, "Imaging the effects of individual zinc impurity atoms on superconductivity in $Bi_2Sr_2CaCu_2O_8+$ ", *Nature*, 403(6771), 746-750, 2000.
- [40] D. M. Eigler and E. K. Schweizer, "Positioning single atoms with a scanning tunnelling microscope", *Nature*, 344(6266), 524-526, 1990.
- [41] B. C. Stipe, M. A. Rezaei and W. Ho, "Single-molecule vibrational spectroscopy and microscopy", *Science*, 280(5370), 1732-1735, 1998.
- [42] C. F. Hirjibehedin, C. P. Lutz and A. J. Heinrich, "Spin coupling in engineered atomic structures", *Science*, 312(5776), 1021-1024, 2006.
- [43] V. W. Brar, "Scanning tunneling spectroscopy of graphene and magnetic nanostructures", 2010.

- [44] N. Cusak and P. Kendall, "The absolute scale of thermoelectric power at high temperature", Proc. Phys. Soc. 72, 898-901, 1958.
- [45] N. Agrat, G. Rubio and S. Vieira, "Plastic Deformation of Nanometer-Scale Gold Connective Necks", Phys. Rev. Lett. 74, 3995, 1995.
- [46] G. Rubio-Bollinger, S. R. Bahn, N. Agrat, K. W. Jacobsen and S. Vieira, "Mechanical properties and formation mechanisms of a wire of single gold atoms", Phys. Rev. Lett. 87, 026101, 2001.
- [47] R. S. Ruoff and A. L. Ruoff, "The bulk modulus of C_{60} molecules and crystals: a molecular mechanics approach", Applied physics letters 59, no. 13: 1553-1555, 1991.
- [48] T. Akasaka, S. Nagase, K. Kobayashi, M. Wlchli, K. Yamamoto, H. Funasaka, M. Kako, T. Hoshino and T. Erata, " ^{13}C and ^{139}La NMR studies of $\text{La}_2@C_{80}$: First evidence for circular motion of metal atoms in endohedral dimetallofullerenes", Angewandte Chemie International Edition in English 36, no.15: 1643-1645, 1997.

Chapter 7

Summary and Suggestions for Further Research

7.1 Summary

In this thesis, I have presented the theoretical methods that I used to model single molecule junctions. These include Density Functional Theory (DFT), Green's functions quantum transport calculations and Tight Binding Model (TB). The theoretical work has focused on providing insight into possible new features in molecular transport with the aim of designing new single molecule devices. The thesis was carried out with the additional aim of modelling and understanding experimental measurements.

This work is divided into two results chapters: Crown-Ether-Bridged Anthraquinones and Fullerenes and Endohedral Metallofullerenes (theory calculations and experiment measurements). The properties of several molecules have been calculated, with some of them being measured experimentally. One of the goals was to demonstrate how the theoretical methods are able to understand and explain the experimental results for both electronic conductance and thermoelectric properties.

In the crown ether calculations (Chapter 5), I investigated two kinds of molecular

scale devices based on AQ-crown-ether- bridged and Diaza-AQ-crown-ether-bridged, each type having three different cavity size. The six molecules accommodated three different sized cations (Li^+ , Na^+ and K^+). Moreover, a donor (TTF) or acceptor (TCNE) was put beneath the anthraquinone part to form complexes. The ability of sensing was tested for the six bare molecules and their complexes. It was shown that the conductance changes when the ions bind leading to the design of a possible molecular sensor. This was achieved through the mechanism of charge transfer from the ion to the molecule.

The second part of Chapter 5 dealt with the thermoelectric properties for the same six molecules and their complexes, including thermopower (S) and power factor (P), and created a map of S versus G . It has shown that thermoelectric properties can be tailored by modifying the nature of the complex.

In Chapter 6 I used C_{60} and $Sc_3N@C_{80}$ as examples of fullerenes and endohedral metallofullerenes. The electronic conductance (G), was calculated for both molecules for different rotating angles and squeezing pressure. S and P were calculated as a function of rotating and pressing the molecule. The experimental measurements I carried out on these molecules show an excellent agreement between the theory and experiment. The nature of the bi-thermoelectric behaviour contributes to the localized orbital within the cage which is sensitive to the junction geometry.

7.2 Suggestions for Further Research

This thesis has opened up many potential future research directions. For instance, in the case of crown ethers, it would be useful to focus on the ability of crown-ether-based molecular wires for discriminating sensing of alkali-metal ions, especially for ring cavities that have sulfur atoms. The design of new molecules which could attract bigger cations and form complexes such as sandwich (two crowns with cation) is a possibility that could also be explored. These studies would show

that the response of each molecular wire to analyte binding is different, and the range of responses from a collection of such wires constitutes a unique fingerprint that further increases the ability of such wires to discriminate between different analytes.

The key to enhancing thermoelectric performance lies in taking advantage of resonances in the electronic density of states (associated with the discrete spectrum of molecular levels) because the thermopower is loosely proportional to the slope of the density of states at the Fermi energy of the electrodes. In C_{60} and all single molecules measured to date, the Fermi energy is far away from any molecular energy levels and there currently exists no experimental evidence of the effect of resonant transport on thermoelectric properties.

One interesting direction of study would be assessing the transport properties of a single atom inside a cage as a further example of endohedral metallofullerenes, examining also the phononic part due to the rattling atom inside the cage. The calculations of the thermopower in this thesis have focused on the electrical contribution. The contribution of phonons may play an important role in the design of efficient devices (i.e maximising ZT), so the theoretical method should be expanded to include this contribution. Exohedral fullerenes are another promising type of molecules, especially in trying to use P-type and N-type to form the tandem devices that increased the generated voltage as shown in Figure 7.1.

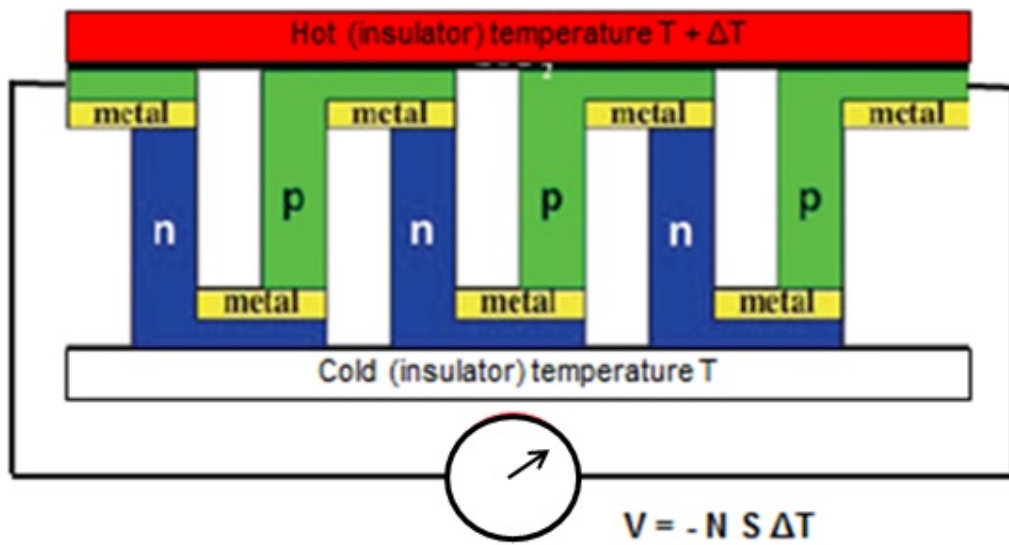


Figure 7.1: Schematic of a Tandem device